Electrochemical Impedance Spectroscopy (EIS) Sensors for the Detection of Heavy Metal Ions in Water-based Solutions

Thesis

In partial fulfilment of the requirements for the degree of:
Master of Science
In Materials Science and Engineering
At Delft University of Technology
To be defended publicly on: 25th November of 2020 at 15:00

by

Ai-Yu Liou

Supervisors:
Dr. Peyman Taheri (Delft University of Technology)
Dr. Majid Ahmadi (University of Groningen)
Lazlo Kleczewski (TWTG R&D B.V.)
Pieter de Bruijn (TWTG R&D B.V.)

Student number	4815432
Project duration	Jan. 2020 - Nov. 2020

Thesis committee

Prof.dr.ir. Arjan Mol (Chair)	Delft University of Technology
Dr. Peyman Taheri	Delft University of Technology
Dr. Majid Ahmadi	University of Groningen
Dr. Yaiza Gonzalez Garcia	Delft University of Technology
Dr. Marilia Moura de Salles Pupo	Delft University of Technology

Abstract

The detection of heavy metal ions (HMI) is an essential step in water treatment. Due to their adverse effect on human health and the environment, various agencies have set guidelines for the concentration of HMI in drinking water. However, conventional HMI detection techniques, such as atomic absorption spectroscopy (AAS) and inductively coupled plasma mass spectroscopy (ICP-MS), are often too expensive and not practical for on-site real-time monitoring. Electrochemical methods, including anodic stripping voltammetry (ASV) and electrochemical impedance spectroscopy (EIS), appear as alternatives for detecting HMI. Among these techniques, EIS possesses great potential in providing more information about water composition with modeling and data analysis. However, past research on the physical interpretation of the impedance response and the differentiation of different types of HMI in a mixed aqueous solution is inadequate.

In the first part of the research, the electrochemical cell for HMI detection was constructed with pure platinum electrodes and the impedance response was collected for two types of HMI solutions, $ZnSO_{4\ (aq)}$ and $Pb(NO_3)_{2(aq)}$, and their mixed solution. The data was collected repetitively in a wide range of settings to understand the influence of varying parameters, including concentration, types of HMI, temperature, mixing ratio, and designs of the electrochemical cells. The reproducibility of results was quantified by the calculation of standard deviation. It was found that each HMI solution has its own characteristic impedance value. In addition, the change of impedance response follows a linear trend line in the Bode and Nyquist impedance plot when varying parameters such as concentration, temperature, and mixing ratio. In addition to controlled experiments, the electrochemical cell was tested in tap water and industrial water samples provided by the project's collaborators.

In the second part of the research, various techniques of surface analysis were conducted on the surface of the platinum working electrode, including scanning electron microscope (SEM), energy-dispersive X-ray spectroscopy (EDS), and X-ray photoelectron spectroscopy (XPS). Since the HMI-related adsorbates were presented in the results, a hypothesis was proposed, which suggests that the adsorption/desorption process of HMIs has taken place during the EIS measurement, and this phenomenon contributes to the inductive behavior in the impedance response. Finally, equivalent circuit models were proposed based on the result of EIS measurements, surface analysis, and literature studies. Data fitting for the impedance data was carried out with Zview software version 3.5h. Charge transfer resistance and other equivalent circuit elements' impedance values were compared to specify the differences between the two HMI.

Acknowledgements

I would like to express my deep appreciation to my main supervisors, Dr. Peyman Taheri and Dr. Majid Ahmadi, for their patient guidance and positive encouragement throughout the whole project. I would also like to express my great appreciation to the supervisors from TWTG, Lazlo Kleczewski, and Pieter de Bruijn, for sharing their knowledge on the development of the EIS sensor with me and providing enthusiastic supports to the project.

As for the memorable time working in the laboratories of TU Delft, I would like to thank all the technicians and staffs who had ever helped me solve the technical challenges, taught me the operation of instruments, or given me wise advises or direct support for my experiments, including Agnieszka Kooijman, Urša Tiringer (for helping me with the XPS measurements), Luis de Almeida Nieto, Sander Van Asperen, Ruud Hendrikx (for helping me with the XRD measurements), Remko Seijffers, and Kees Kwakernaak.

My special thank is given to Dr. Yaiza Gonzalez Garcia, who brought me to the world of electrochemistry with her wonderful lesson on Corrosion Science and taught me the fundamental knowledge needed in this project.

Finally, I would like to thank my family in Taiwan deeply for supporting my study here in TU Delft, both financially and emotionally, and my beloved friends for their care and emotional supports during this memorable period in 2020.

Ai-Yu Liou
Delft, Nov 2020

Contents

List of Tables

List of Figures

1

Introduction

Water treatment is any process that improves the quality of water to make it more acceptable for a specific end-use. The end use may be drinking, industrial water supply, irrigation, river flow maintenance, water recreation, or many other uses, including being safely returned to the environment. To conduct proper water treatment, detecting the toxic compounds and particles in the water is an important step. Among these contaminants, heavy metal ions (HMI) are considered highly toxic at trace levels and can lead to various diseases after being intaken by human beings.

Electrochemical Impedance Spectroscopy (EIS) is an electrochemical technique for measuring the impedance of a system, depending on the AC potentials frequency. EIS has played an essential role in characterizing many types of systems and providing information on various fundamental processes, i.e., adsorption/film formation, rate of charge transfer, ion exchange, diffusion, etc., which occurs at the electrode | electrolyte interface. Hence, EIS provides a basis for the detection of heavy metal ions in water through electrochemical characterizations.

This chapter contains the literature study for the cooperated project between TU Delft and TWTG on developing a portable EIS sensor for on-site monitoring of water quality. In this chapter, section 1.1 provides some background knowledge for understanding heavy metals, including their definition, toxicity, pollution source, and the international guideline value for drinking water. The conventional ways of detecting HMI are discussed at the beginning of section 1.2, while the rest of the section gives an overview of various electrochemical methods for HMI detection as alternatives to conventional techniques. Among these methods, the working principles and the roles of anodic stripping voltammetry (ASV), cyclic voltammetry (CV), and EIS in this research field are further discussed in detail. Finally, section 1.3 focuses on the existing research of EIS sensors for HMI detection, and a table of the summary is made. This section is completed by a discussion on the potentials of the

EIS sensor. This project's research questions developed together with supervisors from TU Delft and TWTG are listed at the end of the chapter in section 1.4.

1.1. Background knowledge about heavy metal

"Heavy metal" is a general description rather than a well-defined term. It is considered any group of metals or metalloids with atomic weights between 63.5 and 200.6 g/mol [17] and possesses a density greater than 4 g/cm3, or five times greater than water [18]. By this definition, more than 50 elements in the periodic table can be classified as heavy metals. However, the term "heavy metal" is more commonly referred to as the metallic/semi-metallic elements that pose a threat to human health and flora and fauna in the environment due to their chemical properties and accessibility [19]. This definition, concerning the toxicity, thus narrows down the categories of heavy metal to 17 elements [20]. These elements, generally including mercury (Hg), cadmium (Cd), arsenic (As), chromium (Cr), lead (Pb), zinc (Zn), copper (Cu), iron(Fe), silver (Ag), and nickel (Ni), have adverse effects on living organisms when being intaken at a certain level.

The toxicity of these elements comes from the inhibition of enzymes and the induction of oxidative stress [21]. By blocking the functional group of metabolically important molecules and interfering with the transportation of electrons, the presence of excessive heavy metals in living organisms results in the generation of reactive oxygen species (ROS) [22] [23]. This disruptive mechanism then leads to the damage of DNA [24], peroxidation of lipids [25], and the disfunction of proteins [26], which can further lead to a wide range of diseases for humans related to the respiratory system, the central/peripheral nervous system, immune system, and organs (e.g., kidneys, lungs) [21]. In addition, since these elements are non-biodegradable and tend to accumulate in the biological system, a trace level of contamination is already unacceptable.

1.1.1. The emission of heavy metal pollution

The emission of heavy metal into the environment can result from both natural and anthropogenic activities. However, the major emission occurs during the mining operation and industrial processes [27]. Heavy metals exist naturally in the earth's crust in the form of sulfide or oxide ores. During mining, some heavy metals are left as tailings in mining pits and are exposed to wind and flood [28], posing a severe threat to the environment. Other major sources of emission include the smelting and refining process in foundries and smelters, wastewater released from electroplating, and by-products of combustion [18]. In addition to the industrial process, heavy metal can also be emitted into the environment through the exhaust of automobiles and household waste disposal. Since heavy metals are widely used in pigments, fertilizer, cosmetic products, batteries, and electronics [21], it can also contaminate the soil and rivers due to the leakage of heavy metals in landfills [29]. Compared to integrating into suspended sediments, heavy metals' deleterious effect is more severe when dissolving in the water due to mobility and reactivity.

1.1.2. The regulation for heavy metal in drinking water

To ensure society's safety, various agencies at the national, regional, and international levels have set the concentration limits of heavy metal in the drinking water. These agencies include the World Health Organization (WHO), United Nations Environment Programme (UNEP), European Union (EU), and the United States Environmental Protection Agency (USEPA). At the international level, the WHO first published the International Standards for Drinking-Water in 1958. After several revisions and renewed publications, the guideline standard for drinking water is now written in the latest version of Guidelines for Drinking-Water Quality (GDWQ) 4th edition published in 2011 [1]. Table 1.1 shows the guideline value and the detection limit of conventional detection techniques for heavy metals in drinking water. It should be noted that some elements, such as Fe, Zn, Cu, served as essential nutrients for humans as they play a role in the metabolism and synthesis of enzymes. Their guideline values are either high or not defined due to relatively low toxicity compared to Cd, Hg, As, and Pb, which have no bio-importance to humans.

1.2. Electrochemical sensors for detecting HMI

There are various spectroscopic techniques to identify the concentration of heavy metal ions (HMI) in aqueous solutions. The conventional ways include the use of atomic absorption spectroscopy (AAS) [30], cold vapor atomic absorption spectrometry (CV-AAS) [31], inductively coupled plasma mass spectroscopy (ICP-MS) [32] and inductively coupled plasma-optical emission spectrometry (ICP-OES) [33]. Varieties of AAS, ICP-MS, and ICP-OES and their detection limits for HMI are indicated by WHO in GDWQ as shown in table 1.1. Other less common techniques are also explored by various researchers, including X-ray Fluorescence Spectrometry (XRF) [34], neutron activation analysis (NAA) [35], and atomic fluorescence spectroscopy (AFS) [36]. The instruments used to perform these detection methods have versatile applications, and they are suitable for simultaneously detecting a wide range of elements. In addition, they possess high sensitivity and low limit of detection (LOD) in the femtomolar range [37]. However, these instruments are costly and bulky, and the process of detecting HMI is time-consuming. It requires well-trained technicians to prepare multi-samples and operate the complex equipment, followed by complex analysis and data interpretation. Additionally, except XRF, most of the techniques mentioned above are only suitable for the quantitative measurement of HMI if they are not coupling with other techniques, such as chromatography [38]. Multiple steps of measurement with transporting and handling of samples greatly increase the risk of sample contamination [37].

As the need to develop on-site real-time monitoring of HMI increases, electrochemical sensors gain more attention from researchers in recent years. Compared to spectroscopic measurement, electrochemical sensors are much cheaper, easier to operate, and faster in data analysis. They can also be designed to be portable and with replaceable electrodes, which is suitable for on-site monitoring and does not require heavy training for operators. Although the LOD of electrochemical sensors is not as low as conventional spectroscopic techniques and the sensitivity is

Table 1.1: Table: Basic physical properties of heavy metals and their guideline value and detection limit provided in the chemical fact sheet of WHO GDWQ, 2011 [1].

	Atomic weight (g/mol)	Density at r.t (g/cm3)	Guideline value (µg/l)	Detection limit by conventional techniques
Cadmium (Cd)	112.41	8.65	3	0.01 µg/l by ICP-MS 2 µg/l by flame AAS
Mercury (Hg)	200.59	13.534	6	0.05 µg/l by cold vapor AAS 0.6 µg/l by ICP 5 µg/l by flame AAS
Lead (Pb)	207.2	11.34	10	1 µg/l by AAS practical quantification limit in the region of 1-10 µg/l
Arsenic (As)	74.92	5.727	10	0.1 µg/l by ICP-MS 2 µg/l by hydride generation AAS or flame AAS
Chromium (Cr)	51.9961	7.19	50	0.05-0.2 µg/l for total chromium by AAS
Nickel (Ni)	58.6934	8.908	70	0.1 µg/l by ICP-MS 0.5 µg/l by flame AAS 10 µg/l by ICP-OES
Copper (Cu)	63.546	8.96	2000	0.02–0.1 µg/l by ICP-MS 0.3 µg/l by ICP-OES 0.5 µg/l by flame AAS
Zinc (Zn)	65.38	7.14	3000*	-
Iron (Fe)	55.845	7.874	-**	-

*The guideline value is not defined; however, it may not be acceptable for the customer if the zinc content is over 3mg/l in the drinking water.

**Not of health concern at levels found in drinking water.

lower than conventional spectroscopic techniques, it is possible to combine different electrochemical measurements on a sensor to identify both the types of HMI and their concentration. In addition, by modifying the electrode materials and combining different electrochemical measurements, both the sensitivity and selectivity can be raised [3].

In general, the setup of an electrochemical sensor for HMI detection consists of three electrodes: working electrode (WE), reference electrode (RE), and the counter electrode (CE), as shown in figure 1.1. The WE is the platform for the adsorption of MHI or the redox reaction between HMI and the electrode. The external electrode signal is passed between the WE and CE, while the potential between WE and RE is measured and recorded with a high input impedance device. This potential is regarded as the cell potential. According to the controlled and measured electric signal, electrochemical methods for HMI detection can be classified into five different categories: static technique (potentiometry), potentiostatic technique, galvaniostatic technique, impedance measurement, and electrochemiluminescence. In addition, potentiostatic technique can be further subdivided into amperometry, chronocoulometry, and voltammetry, as shown in figure 1.2. Among these categories, voltammetry is the most popular HMI detection method due to its high accuracy and sensitivity.

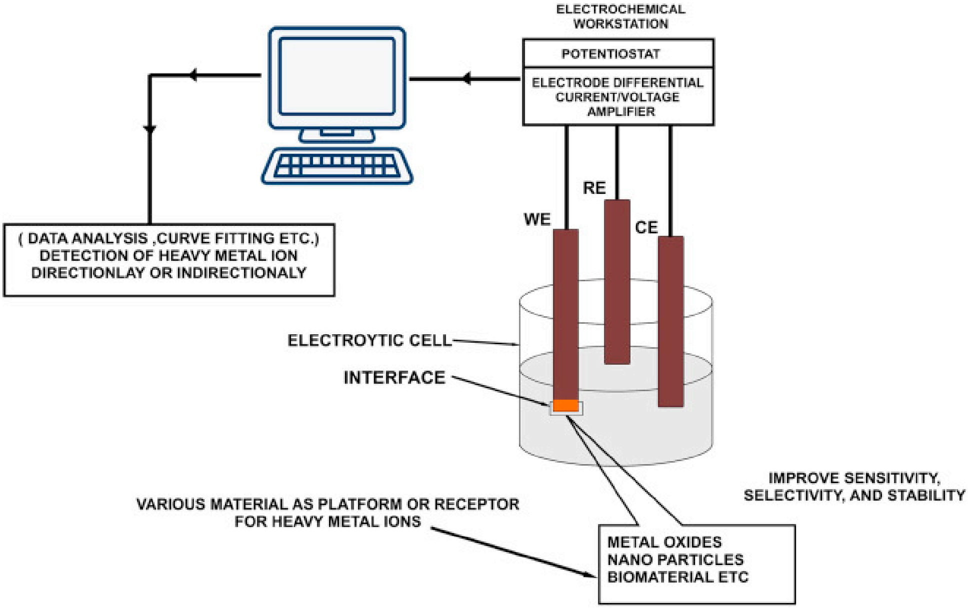

Figure 1.1: General setup of an electrochemical workstation for detecting HMI [3].

In section 1.2.1 and 1.2.2, the principle of anodic stripping voltammetry and cyclic voltammetry and their roles in the field of HMI detection are briefly discussed,

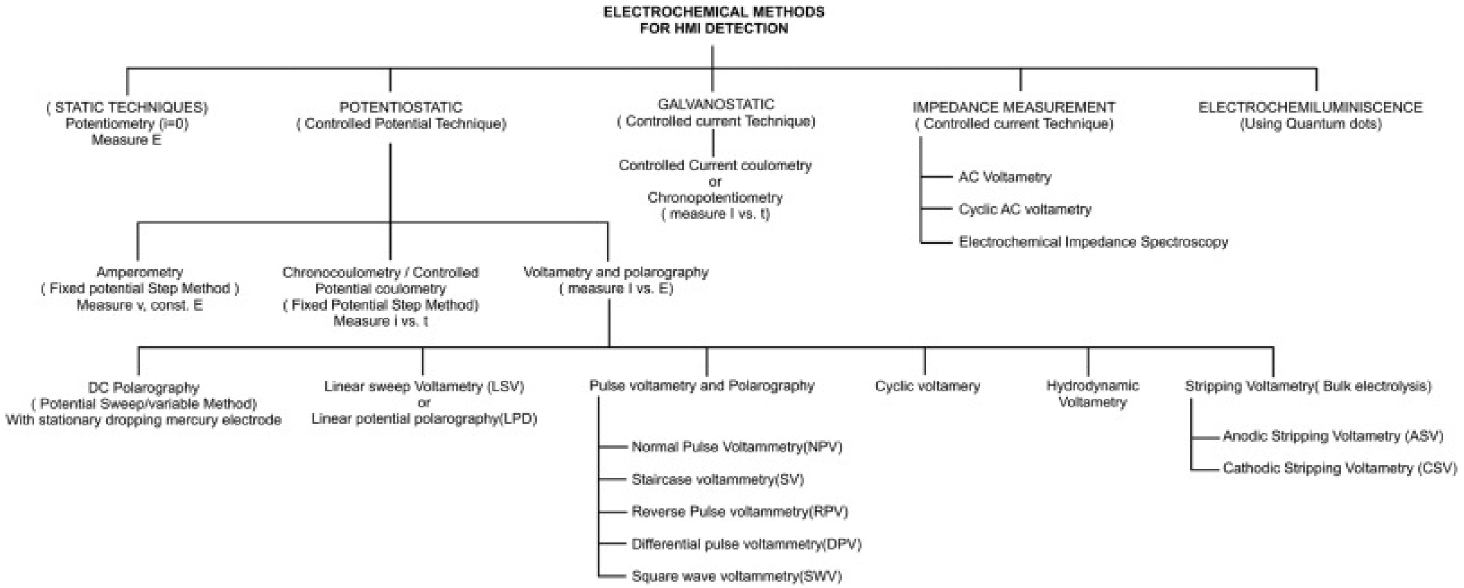

Figure 1.2: Categories of electrochemical methods for HMI detection [3].

while the principle and past research of electrochemical impedance spectroscopy (EIS) in the field of HMI detection are discussed in detail in section 1.2.3 and 1.3. Although voltammetry methods do not relate to this project directly, they provide some important insights into reactions between HMI and electrodes and the methods of evaluating electrode performance. Furthermore, it is also possible to combine these techniques with the EIS sensor developed in this project to expand the applications in the future.

1.2.1. Anodic stripping voltammetry

According to the review done by Bansod *et al.* and Pujol *et al.*, anodic stripping voltammetry (ASV) is by far the most popular electrochemical method to detect HMI quantitatively and qualitatively. As shown in figure 1.2 It can detect 15 types of HMI, including Cd^{2+}, Cu^{2+}, Pb^{2+}, Hg^{2+}, Ag^{+}, and Zn^{2+}, while Co^{2+}, Cr^{2+}, Fe^{2+} can be detected by adsorptive stripping voltammetry, which has a similar working principle as ASV except for the adsorption during preconcentration step [2]. There is plenty of research focus on the development of ASV due to its low LOD up to the picomolar range and high signal to noise ratio (S/N) [39]. During the early stage of development, hanging dropping mercury electrodes (HDME) [40] or thin mercury film electrodes (TMFE) [41] are used as platforms of ASV since they obtain high sensitivity, high hydrogen overpotential, and high purity of the surface. However, due to the concern of environmental pollution and toxicity, they are gradually replaced by bismuth film [9], which serves as good alternatives to TMFE, and electrodes modified with nanostructural coatings, such as carbon nanotubes (CNTs) [42].

There are four steps in the ASV process for a classical mercury platform, including cleaning, electroplating, equilibration, and stripping step [43]. The controlled potentials for different steps are indicated in figure 1.3. During the cleaning step, the potential of WE is held at a high oxidizing level for a period of time. This step is to make sure that the HMI is fully oxidized and is removed from the WE surface with the help of stirring. During the electroplating step, the potential of WE is held at a lower level while the HMI is reduced, deposited, and electroplated on the WE surface. Since the mercury platform and the HMI can form an amalgam at this stage and result in a sharp signal peak at the later oxidation stage, the resolution between different HMI can be significantly increased. In the third step, the equilibration step, the stirring is stopped, and the potential is held at the same level for a period of time. This step is to ensure that the reduced heavy metals are spread evenly on the WE. During the stripping step, an increased potential sweep can be carried out in various waveforms, and the electroplated analytes are oxidized at a certain potential level, depending on the type of analytes, and then the resulted current signal appears as a peak due to the release of electrons. The concentration of the HMI can thus be determined by analyzing the intensity of the current peak. Finally, the process goes back to the cleaning step to prepare for the next run of HMI collection. The general illustration of ASV's principle can be found in figure 1.4.

Depending on the waveform of the potential sweep in the stripping step, ASV can

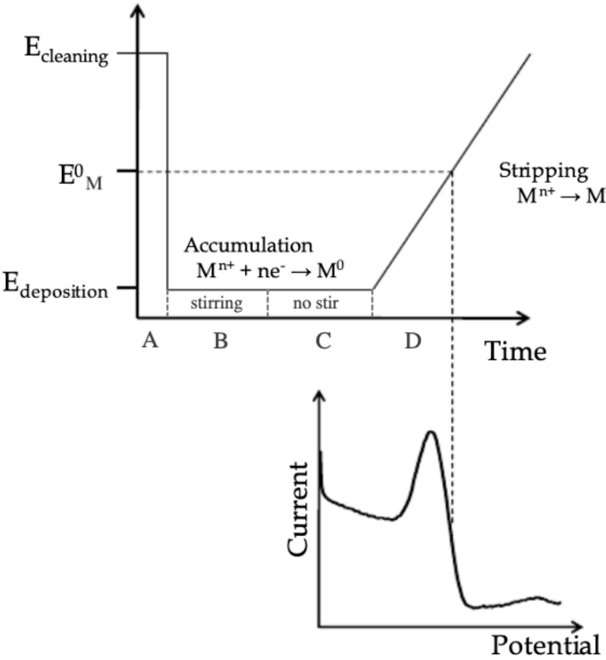

Figure 1.3: Different steps in a typical process of ASV and resulting voltammogram, adapted from ref. [4]. A: cleaning step, B: electroplating step, C: equilibration step, D: stripping step (linear sweep).

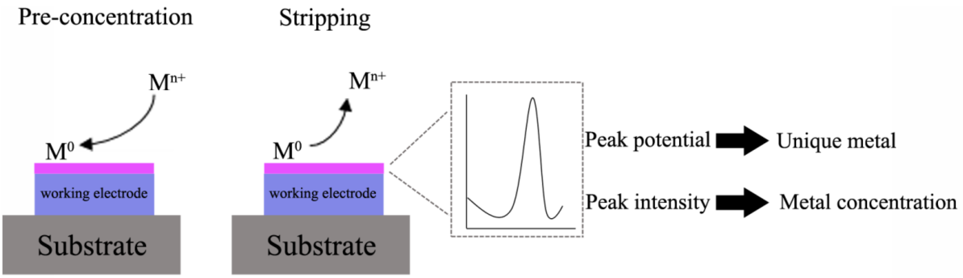

Figure 1.4: Illustration of ASV working principle [2].

Table 1.2: List of HMI and species that can be determined by anodic, cathodic and adsorptive voltammetry [2].

Metals that can be determined by Anodic Stripping Voltammetry		
Antimony	Gallium	Mercury
Arsenic	Germanium	Silver
Bismuth	Manganese	Thallium
Cadmium	Indium	Tin
Copper	Lead	Zinc
Species that can be determined by Cathodic Stripping Voltammetry		
Arsenic	Iodide	Mercaptans
Chloride	Selenium	Thiocyanate
Bromide	Sulfide	Thio compounds
Metals that can be determined by Adsorptive Stripping Voltammetry		
Aluminum	Nickel	Uranium
Cobalt	Chromium	Iron

be further classified into the linear sweep anodic stripping voltammetry (LSASV), differential pulse anodic stripping voltammetry (DPASV), and square wave anodic stripping voltammetry (SWASV). SWASV is by far the most used technique due to its high S/N while DPASV is the second-most-used [3] [37]. The waveforms of potential signals and the typical generated current signal are shown in figure 1.5.

Limitation of ASV

One major drawback of the ASV in HMI detection is the requirement for pH control. During the experiment, an extra acidic solution is often added into the detecting medium to keep the pH at a low value, usually around pH=4 [44]. Since most of the transition metal ions are hydrolyzed into the form of $[M(H_2O)_6]^{2+}$ at pH=7 and can be converted into $[M(H_2O)_5(OH)]^+$ when the pH is raised higher, resulting in the formation of insoluble hydroxides and oxides, the changes in pH can result in shifts in the current peak of ASV, casing troubles for the data interpretation [45]. However, if the pH value is held too low, the electroplated metals on the electrode surface can also be dissolved back in the solution and interfere with the redox reaction taken place at the electrode [44]. Thus, careful control of pH is required for ASV measurement, which poses some challenges for developing an on-site monitoring device for HMI detection.

Another requirement for conducting ASV is having a good charge transfer property of electrodes. Since the identification of HMI, both for types and concentration, relates to the redox reaction on the electrode surface, often an electrode with a

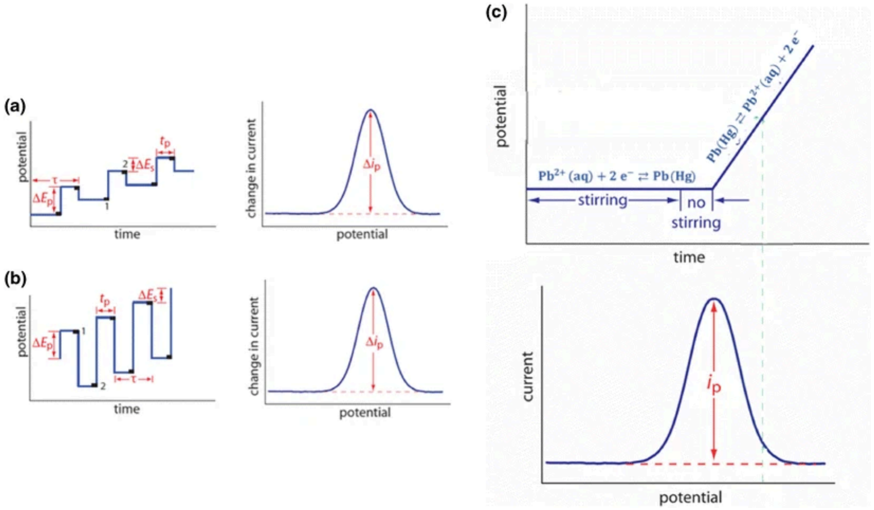

Figure 1.5: Potential signals of different waveforms during the stripping step and the obtained voltammograms. (a): differential pulse, (b): square-wave, (c): linear sweep [5].

large surface area or good electron transfer properties is preferred. The evaluation of electrodes is often carried out with the help of CV and sometimes EIS.

1.2.2. Cyclic voltammetry

Cyclic voltammetry (CV) is an electrochemical technique that provides information about cell potentials, reversibility of the redox reactions, and kinetics of the reaction on the electrode surface. During CV measurement, a linear potential scan is carried out with a constant scan rate (unit: mV/s) from V1 to V2 and then sweep back from V2 to V1, as shown in figure 1.6. These cycles can be executed as many times as needed. The typical result of CV is shown in figure 1.7, where two current peaks can be observed for the reduction reaction and the reversible oxidation reaction. Before reaching the cathodic current peak, the reaction rate is limited by the migration of cations toward the electrode surface, and the diffusion of reduced species is faster than the migration of cations. After the current peak (equilibrium) is reached, the reaction rate becomes limited by the diffusion of reduced species since they hindered the approach of cations toward the electrode surface. This phenomenon causes the voltammogram curve to go downward. By examining the curve's symmetry, the cathodic/anodic peak current, the corresponding potentials, and the interactions between analytes and electrodes can be studied [7].

Although this method is not suitable for the determination of trace HMI since its LOD for ion concentration is higher and the sensitivity is lower than that of stripping voltammetry [46] [47], CV is still widely used in the study of electrochemical sensors for HMI detection since it helps to investigate the charge transfer properties of the electrodes, as well as the range of detection window for other voltamme-

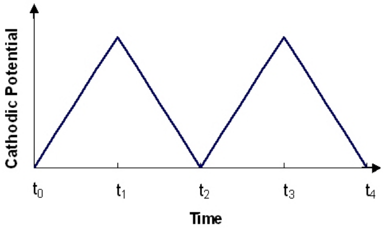

Figure 1.6: Cyclic voltammetry potential waveform, adapted from [6].

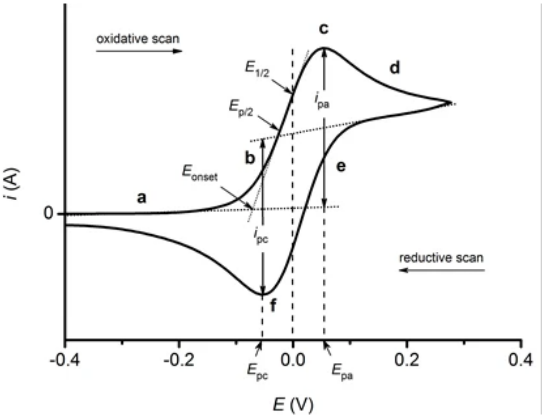

Figure 1.7: Typical voltammogram of CV [7].

try measurements based on the identification of unfavorable redox reactions. For instance, in the experiment conducted by Zhang *et al.*, CV is used for evaluating the properties of modified and unmodified glassy carbon electrodes (GCE) before conducting the SWASV measurement. As shown in figure 1.8 (a), the CV voltammogram of bare GCE, GCE modified by carbon nano-fiber (CNF), and GCE modified by binary metal PtAu alloy nanoparticle CNF hybrid (PtAu/CNF) were compared to show that PtAu/CNF membrane successfully enhance the charge transfer properties of the electrode, giving a more well-defined redox peak. This also results in a higher resolution in the SWASV response, as shown in figure 1.8 (b). Another example is the research done by Zou *et al.* on the properties of the microfabricated bismuth sensor. As shown in figure 1.9, the detection window of a bismuth sensor is confined by the potential levels where the electrode oxidation and hydrogen evolution take place.

1.2.3. Electrochemical Impedance Spectroscopy

Electrochemical impedance spectroscopy (EIS) is a technique that investigates the dielectric properties of a physical system [48]. This dielectric system can exist everywhere, ranging from the surface of a steel casing going through corrosion, any electrochemical cell, fuel cell, to biological membranes. Due to its simplicity and versatility, EIS is widely used in the food industry to examine the concentration of bacteria, the composition and the quality of food [49]. In addition to the food industry, EIS is also widely used in the biomedical field to reveal information about the interactions between biomolecules [50]. In the field of materials science, it is often used in the qualitative evaluation of coating [51], nanocomposite synthesis [52], and film formation. Finally, in the field of HMI detection, EIS has been used as a tool to understand the changes in the surface of a modified electrode during the assembling, as well as the charge transfer properties and diffusion mechanism on the electrode surface.

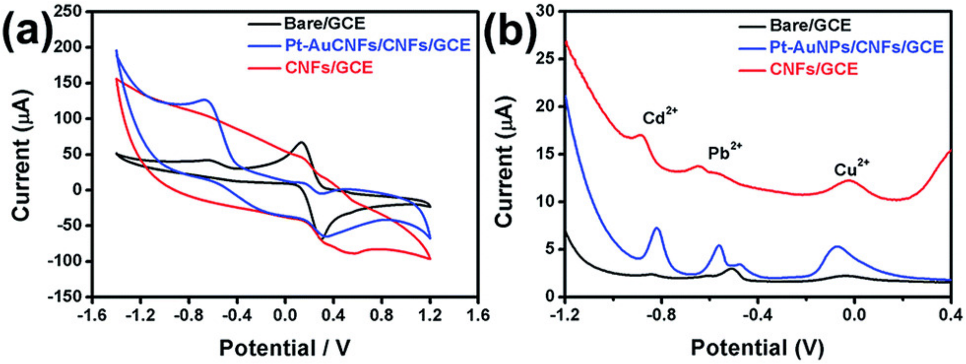

Figure 1.8: (a) Cyclic voltammogram for bare GCE, CNF/GCE, and PtAu/CNF/GCE. Scan rate:100 mV/s. (b) SWASV response of three different electrodes. Among them, PtAu/CNF/GCE gives the most distinguishable stripping peak [8].

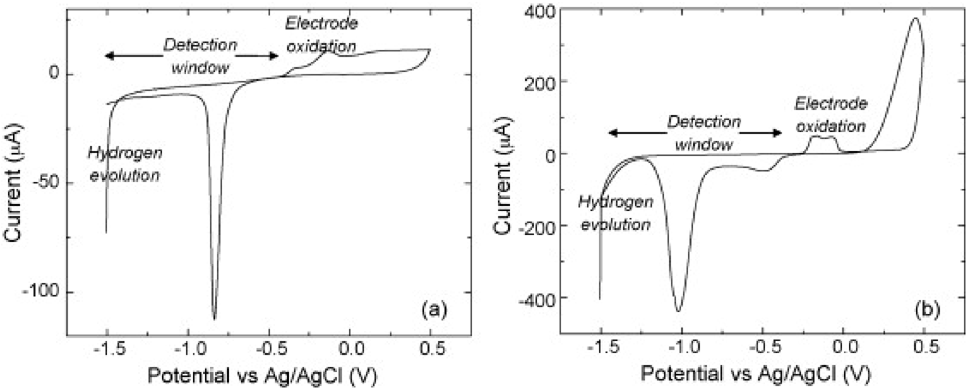

Figure 1.9: Cyclic voltammograms of bismuth electrode in different buffer solutions. (a): PBSbuffer (pH7.43), (b):acetate buffer with 0.1M KCl (pH4.65), Scan rate: 100 mV/s, potential range: −1.5 to 0.5 V. [9].

Working principle and data interpretation of EIS

A complex dielectric system comprises two elements: energy dissipater (resistance) and energy storage (capacitance), which can be related to the concept of impedance in an electric circuit. Due to the nature of dipole movements, dielectric mechanisms, including relaxation and resonance at electronic, atomic, and ionic scales, are dominant at characteristic frequency ranges exerted by an external field [53]. During EIS measurement, an AC-signal of potential is applied to the electrodes in different frequency ranges. At the same time, the impedance response is recorded by dividing the measured current with the potential, shown in eq. 1.1. The result is usually presented with a Nyquist plot and Bode plots. While the Nyquist plot displays the relationship between the real and imaginary parts of the impedance, with each point representing a specific frequency, the Bode plot illustrates the change in the magnitude or phase of the impedance versus the changes in frequency. In the second and third part of eq. 1.1, the expression of impedance in cartesian coordinates and polar coordinates can be found. These expressions correspond to the parameters shown in the Nyquist plot and Bode plot, respectively. At the stage of data analysis, impedance response obtained with EIS is usually fit to an equivalent circuit model, which is a combination of various circuit elements: resistor (R), capacitor (C), inductor (L), constant phase element (CPE), and Warburg impedance element (W). The expressions for the impedance of a resistor, capacitor, and inductor for a sinusoidal system can be found in eq. 1.2 - eq. 1.4.

$$Z(\omega) = \frac{V(t)}{I(t)} = Z_{re} + iZ_{im} = |Z|e^{i\theta} \tag{1.1}$$

$$Z_R(\omega) = R \tag{1.2}$$

$$Z_C(\omega) = \frac{1}{i\omega C} \tag{1.3}$$

$$Z_L(\omega) = i\omega L \tag{1.4}$$

The equivalent circuit model can be semi- or fully empirical. By combining different circuit elements and arranging them in a specific way, the impedance response of the equivalent circuit can be matched with the actual result gained from EIS measurement. However, even though EIS's impedance response can be fully fitted by combining complex circuit elements, the circuit's arrangement should be as simple as possible, which contains at least elements that indicate electrolyte resistance, double-layer capacitance, and impedance of the Faradaic or non-Faradaic process. In addition, the model that can give insights into the physical meaning of the system is preferred [10].

There are two standard equivalent circuits commonly used in electrochemical systems, including the Randles Cell and the Mixed Kinetic and Diffusion Control model. The equivalent circuit arrangement and the corresponding Nyquist plot and Bode plots of these two models are illustrated in figure 1.10. The radius of the semicircle found in Nyquist plots represents the charge transfer resistance, R_{ct}, of the electrode, while the capacitance of the double layer is represented in the term C_{dl} and the resistance of the electrolyte or solution is represented in the term R_{el}. The main difference between the Randle circuit and the Mixed Kinetic and Diffusion Control model is the presence of the Warburg element. The presence of this element is due to the fact that the polarization in the electrochemical cell is controlled both by the kinetic and the diffusion processes. It can be seen in the Nyquist plot of the Mixed Kinetic and Diffusion Control model that there is a linear line of 45°at the low-frequency range, which is related to diffusion. This kind of Nyquist plot is essential in understanding the experimental result illustrated in chapter 3.1.

The research done by Mei *et al.* further explained the physical interpretation of the Nyquist plot in an electric double-layer capacitor (EDLC) system. The researchers used the modified Poisson−Nernst−Planck model and experimental measurements to reproduce the Nyquist plot for a single EDLC system shown in figure 1.11. The result shows that it is possible to extract physical parameters, such as electrode resistance, bulk electrolyte resistance, diffuse layer resistance, and equilibrium differential capacitance, directly from the Nyquist plot without using the equivalent circuit model. The physical parameters that can be retrieved directly from the Nyquist plot are illustrated in figure 1.12. However, it should be noted that the physical interpretation of Nyquist impedance claimed by Mei *et al.* are different from the general explanations developed in the field of EIS. For instance, the resistance present in the very high-frequency region is generally attributed to ohmic resistance, which is the sum of electrolyte resistance, electrode resistance, and the contact and intrinsic resistance in the electric circuit [54] [55]. However, Mei *et al.* claimed that the high-frequency resistance (HFR) in the electrochemical system is solely related to the electrode's resistance. In addition, the size of the first semicircle present in the high-frequency region is generally associated with the charge transfer resistance at the electric double layer [56] [57], but Mei *et al.* claimed that this region is associated with the bulk electrolyte resistance. Since the research done by Mei *et al.* is relatively new and has not been fully verified by other researchers, the interpretation of the Nyquist impedance plot in this research follows the general theories that are more accepted in the field of EIS study. The interpretation of the Nyquist impedance plot conducted in this research is further illustrated in chapter 3.1.1.

1.3. Development of EIS sensors for HMI detection

EIS is a less popular electrochemical method compared to ASV in the field of HMI detection. Most of the time, the technique was used to examine the properties of electrodes after fabrication and surface modification rather than detecting HMI. Although the research on EIS sensors for HMI detection is relatively new and underdeveloped, a few past researches have revealed its potential and possible applications. Table 1.3 shows the overview of the past research on HMI detection with EIS as the main technique. It is considered that EIS sensors possess a low LOD for HMI concentration in the aqueous solution that is generally below the environmen-

(a) Equivalent circuit of RC model

(b) Equivalent circuit of MK&DC model

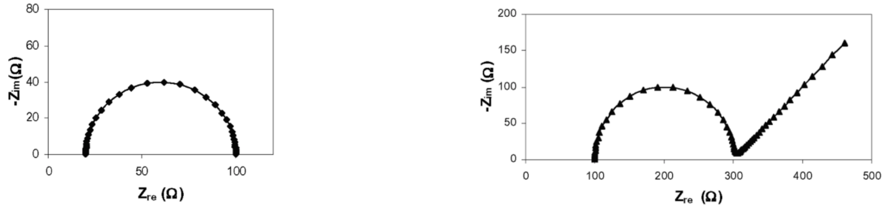

(c) Typical Nyquist plot of RC model

(d) Typical Nyquist plot of MK&DC model

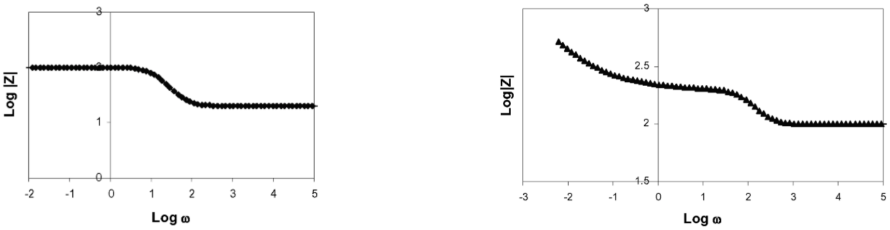

(e) Typical Bode impedance plot of RC model

(f) Typical Bode impedance plot of MK&DC model

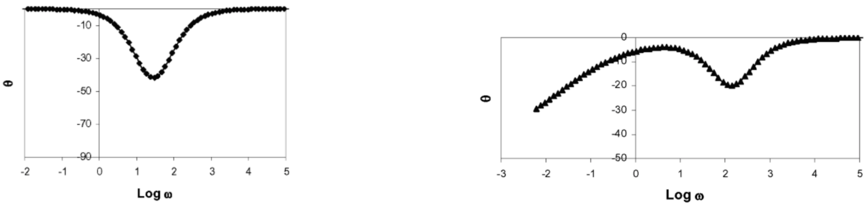

(g) Typical Bode phase shift plot of RC model

(h) Typical Bode phase shift plot of MK&DC model

Figure 1.10: The comparison of the equivalent circuit and the frequency response between Randles Cell and Mixed Kinetic and Diffusion Control model [10].

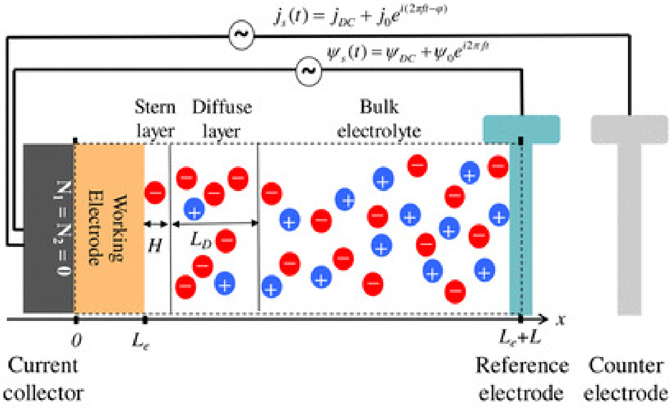

Figure 1.11: The construction of a one-dimensional EDLC system in a three-electrode setup. The dashed line region is the simulated domain [11].

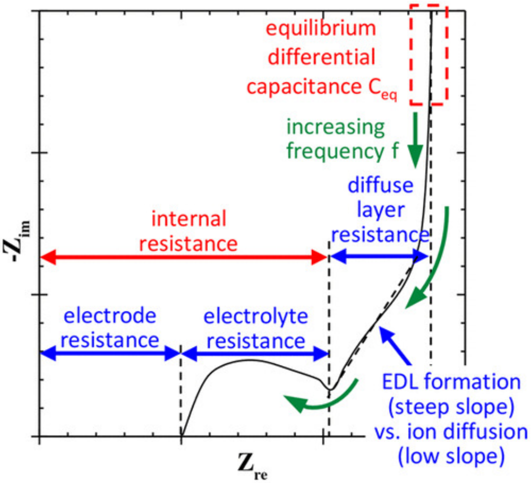

Figure 1.12: The parameters that were retrieved from different parts of the Nyquist plot in ref. [11].

tal regulations. Furthermore, EIS sensors are easy to operate and can be designed to suit on-site monitoring in rivers. For instance, Avuthu *et al.* designed the EIS sensor with screen-printed electrodes on PET film, as shown in figure 1.13, which is cost-efficient in fabrication and flexible in use. For this design, a distinguishable signal was obtained at a lower frequency region, ranging from 1 Hz to 2 kHz, and the average percentage change of impedance compared to DI water was 18% and 52% for Pb^{2+} concentration at 1 nM and 1μM respectively, as shown in figure 1.14a. It shows that the addition of Pb^{2+} into the DI water exhibits an evident change in impedance value. In addition to the research on Pb^{2+}, the LOD for Cd_{2+} was also investigated with the same design, as shown in figure 1.14b. When the concentration of the dissolved $Cd(NO_3)_2$ increases, the radius of the first semicircle on the Nyquist impedance plot decreases, implying the decrease of the charge transfer resistance on the electrode surface as the conductive ionic concentration increases at the surface. The LOD for Cd^{2+} is then determined as 1nM.

Figure 1.13: Photo of the screen-printed EIS sensor on PET film [12].

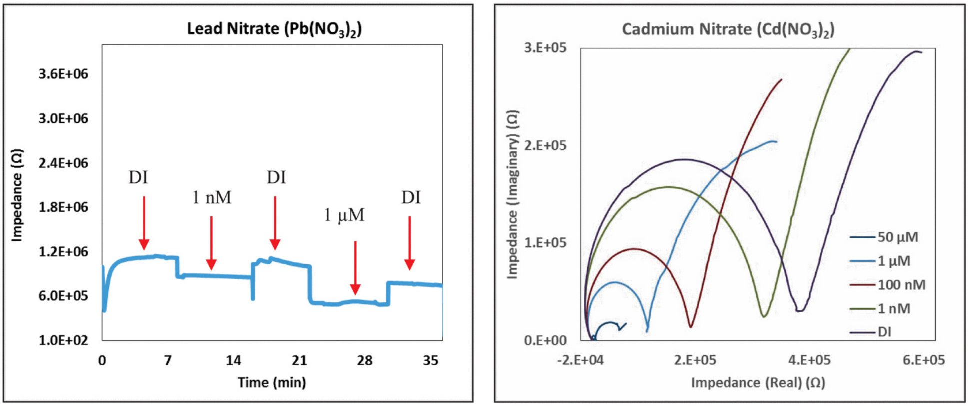

(a) The dynamic plot of impedance v.s time when dosing $Pb(NO_3)_2$ into DI water alternatively

(b) Nyquist plot for different concentrations of $Cd(NO_3)_2$ dissolved in the DI water

Figure 1.14: The results of HMI detection with the EIS sensor presented in ref. [12].

EIS is generally considered as a non-selective method for HMI detection since

Table 1.3: The overview of past research on EIS detection of HMI.

Year	Electrochemical platform	Medium	EIS setting	Detected HMI	LOD
2012 [58]	2-electrode system with photolithographically fabricated Au interdigitated electrodes	(7-(diethylamino)-3-((2-hydroxy-4-methyl phenyl imino) methyl)-2H-chromen-2- one) (DHMMC)	20 Hz - 2 kHz; 1mV	Zn^{2+}	100pM
2014 [12]	Screen-printed electrodes on PET: WE: Carbon ink RE: Ag/AgCl ink CE: Ag ink	Deionized (DI) water	1 Hz - 100 kHz; 1V	Pb^{2+} ($Pb(NO_3)_2$) Cd^{2+} ($Cd(NO_3)_2$)	1nM, 1nM
2015 [14]	WE: Au electrode modified with Cu2O, nano-chitosan particles (NCs) or Cu2O@NCs nanocomposites, with or without adsorption of DNA strands on the surface RE: Pt-slide CE: Ag/AgCl	1:1 mixture of 5 mM of $K_3[Fe(CN)_6]/K_4[Fe(CN)_6]$ and PBS (pH 7.4, containing 0.1 M of KCl)	1 mHz - 1 MHz	Hg^{2+} ($Hg(NO_3)_2$)	0.15 nM (S/N = 3)
2017 [13]	WE: (1) Au (2)Pt (3) glassy carbon (GC) (4) silver nanoparticle (SNP)	Water	1 Hz-100 kHz	Cd^{2+} ($CdSO_4$•$8H_2O$) Cu^{2+} ($CuCl_2$ •$2H_2O$) Co^{2+} Pb^{2+} Zn^{2+} ($ZnCl_2$) As^{3+} (As_2O_3) Cr^{2+} ($K_2Cr_2O_7$) Ni^{2+} ($NiCl_2$)	-*

*The research focuses on the classification of different types of HMI by analyzing impedance signal, rather than the determination of the HMI concentration.

the conductivity values gained from EIS are non-specific and do not provide information on the type of ionic compounds or materials in the solution. However, by separating the magnitude and phase of measured impedance, more qualitative information can be obtained from the measurement. According to the research done by Nambo *et al.*, a transfer function can be gained from the phase characteristics and different magnitude of EIS impedance response related to particular conductive solutions. This finding provides the basis for HMI classification by analyzing the EIS frequency response. Another example of using modeling techniques for extracting HMI information from EIS is the research done by Karkra *et al.*, in which principal component analysis (PCA) and cluster analysis were used to classify eight different HMIs, as shown in figure 1.15. The sets of impedance data were first collected in the separate matrix, called single-frequency multi-electrode (SFME), multi-frequency single electrode (MFSE), and multi-frequency multi-electrode (MFME), before running PCA and clustering. By conducting the cluster analysis and PCA on the SFME matrix, it was observed that at 1 kHz, the classification is more reasonable than other frequencies, 1 Hz, 100 Hz, 10 kHz, and 100 kHz. In addition, the MFSE matrix analysis showed that the silver nanoparticle (SNP) working electrode provided the best classification compared to the other electrodes. Overall, the study shows the possibility of simultaneously identifying multiple HMIs by analyzing EIS data with the algorithm. However, the optimal classification for the eight HMIs came from the cross-analysis of impedance values obtained from different working electrodes, namely the MFME matrix shown in figure 1.16, with the help of the particle swarm optimization (PSO) algorithm.

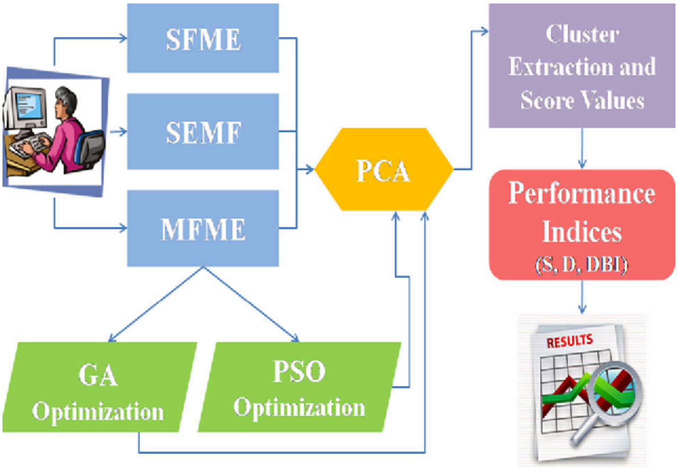

Figure 1.15: The analytical methodology of classifying HMI in ref. [13].

In addition, EIS measurement can also become selective by choosing an electrode that selectively combines with a specific HMI. For instance, Liu *et al.* synthesized cuprous oxide and nano-chitosan composites (Cu_2O@NCs) and modified its

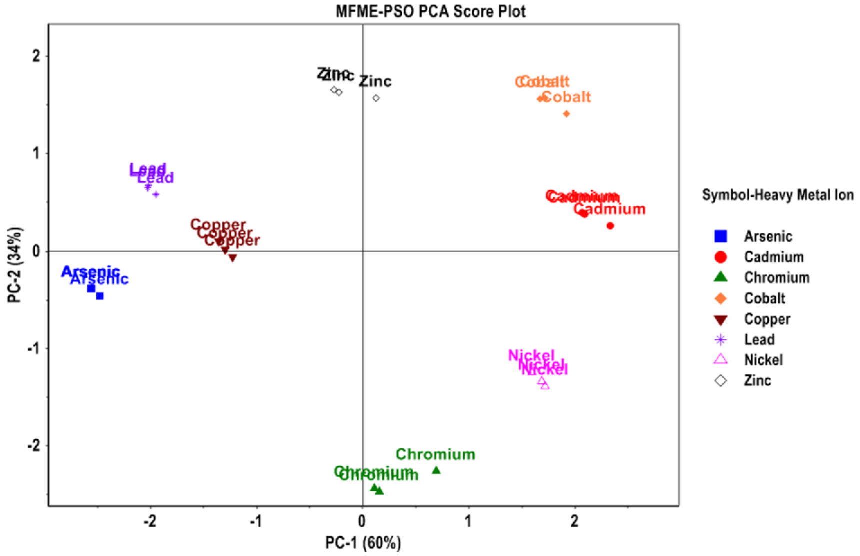

Figure 1.16: PCA score plot for MFME matrix, with optimization from particle swarm optimization (PSO) algorithm [13].

surface with single-stranded, thymine (T)-rich DNAs before spin-coating it on the Au electrode. Since T-rich DNA acted as a biosensor and generated T–Hg^{2+}–T coordination, the Au/Cu_2O@NCs/DNA electrode only detects Hg^{2+} and is not interfered by the presence of other HMIs, including Pb^{2+}, Co^{2+}, Zn^{2+}, Ag^+, Fe^{3+}, and Ni^{2+}. The EIS sensor thus exhibited a satisfactory selectivity for $Hg2^+$ even when the concentration of the interfering ions is 5-time higher than that of Hg^{2+}. In addition, Liu *et al.* also compared the variation of interfacial charge transfer resistance (R_{ct}) after the immobilization of DNA strands and after the collection of Hg^{2+} for different types of electrodes. Before the experiment, the electrodes were first investigated with CV, and the equivalent circuit model was constructed by data fitting. The embedded drawing in the figure 1.17 graph (b) indicates the equivalent circuit of the electrochemical system, where R_{ct} represents the charge transfer resistance, R1 the electrolyte solution resistance, CPE1 the constant phase element, and W1 the Warburg impedance. The result shows that the Cu_2O@NCs electrode exhibited the highest variation of interfacial R_{ct} between different steps compared to Cu_2O and NCs electrodes, as shown in figure 1.18, which indicates a higher sensitivity during the detection of Hg^{2+}. However, since the Hg^{2+} ions coordinated with the T-rich DNA on the electrode surface, the sensor's usability and the repeatability of the EIS result rely on the cleaning of the electrodes. By rinsing the electrode with 50 mM cysteine after usage, the T-Hg^{2+}-T structure can be disrupted and the sensor can be regenerated. Furthermore, Liu *et al.* also tested the CuO@NCs sensor with river water samples with the addition of Hg^{2+}, and it showed a high recovery rate (>100%).

Another way to make the EIS sensor become selective is to combine it with differ-

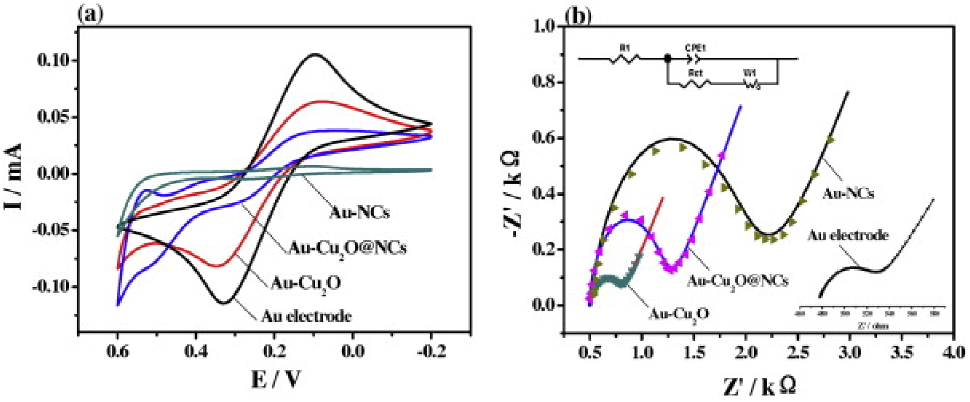

Figure 1.17: (a) CV and (b) EIS analysis of Au, Au/Cu_2O, Au/Cu_2O@NCs, and Au/NCs electrodes [14].

ent electrochemical techniques. For instance, Narakathu *et al.* used coumarin-based fluorescent chemosensor, specifically (7-(diethylamino)-3-((2-hydroxy- 4-methyl phenyl imino) methyl)-2H-chromen-2- one (DHMMC)), to selectively detect Zn^{2+} through a chelation-enhanced fluorescence mechanism. In addition to the fluorescence Spectroscopy, EIS was performed as a part of dual detection. In the research, a better S/N was observed at a lower frequency, ranging from 100 Hz to 400 Hz. At 200 Hz, the percentage changes of impedance response were 38%, 33%, 28% as the concentration of Zn^{2+} varied from 100 pM to 100 nM to1 μM to 1 mM, respectively.

In the research related to EIS sensors for HMI detection, the requirement of pH control is not clearly mentioned. It is not clear if the change in pH will significantly influence the impedance response in the EIS system designed for HMI detection. In addition, the charge transfer efficiency of the electrode is not the main focus for EIS sensor, but rather the ability to produce evident variation in R_{ct} values before and after the presence of HMI. For instance, in figure 1.17, the charge transfer property of a modified Cu_2O@NCs electrode is not as good as the original Au/Cu_2O electrode, which produces a more obvious redox peak during CV measurement. However, since the modified Cu_2O@NCs electrode is able to produce the highest variation of charge transfer resistance after detecting Hg_{2+} compared to the other electrodes as shown in figure 1.18, it suits better for the EIS measurement.

Another parameter to consider in the experiments is temperature. The temperature greatly influences the result of both ASV and EIS because it affects the kinetics of mass transfer and the charge transfer properties [60] [61]. Therefore, it is essential to make sure the experimental environment is temperature-controlled to avoid misinterpretation of the data. It is also worth investigating the quantified influence of changing temperature on the EIS result to calibrate the error it causes in the application stage.

For EIS sensors in the field of HMI detection, there is currently no scientific

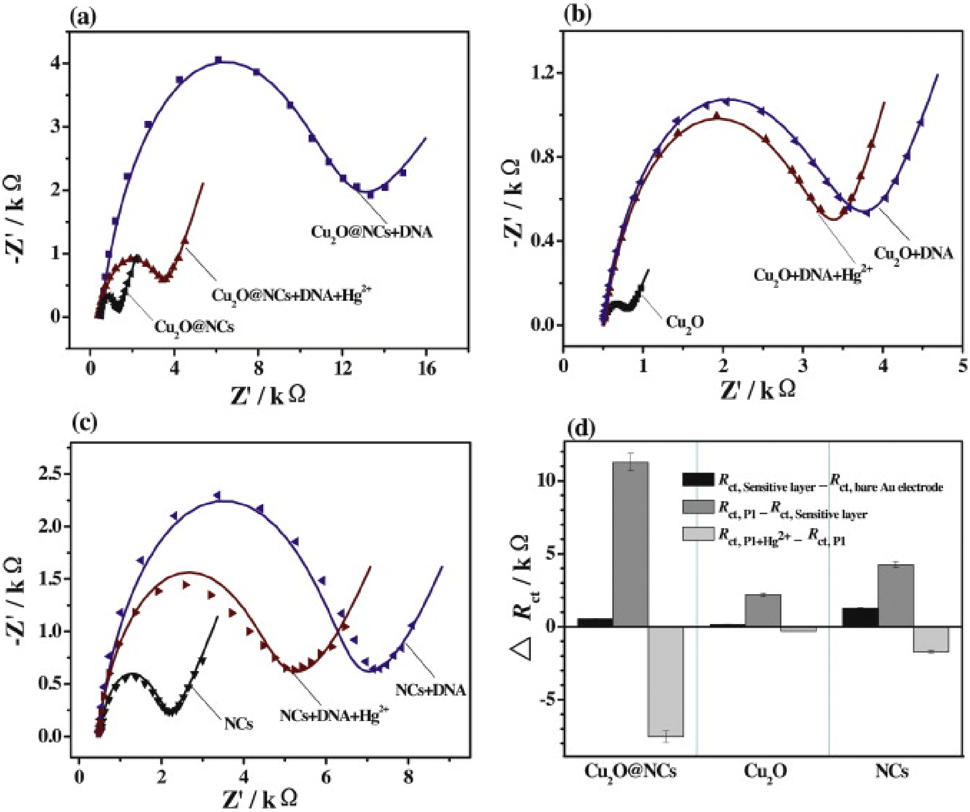

Figure 1.18: Nyquist plot showing the changes of impedance for (a)Cu_2O@NCs (b)Cu_2O (c)NCs electrodes during the three-step process: without immobilization of DNA, immobilization of DNA, and the collection of Hg^{2+}. Graph (d) shows the quantified values for R_{ct} variation between different steps [14].

papers being published to explain the interaction between two or more HMIs and its effect on the impedance response, nor about the physical interpretation of the distinguishable signals in Bode plots for various HMI detection. Even though it is possible to extract characteristic information of HMI from the EIS results through data analysis or modelling techniques, further research is required to provide the scientific basis for validation and further improve the existing models.

In conclusion, despite the research on the EIS sensor for HMI detection is still in the developing stage, the EIS sensor has shown great potential to provide more quantitative and qualitative information with modelling techniques. In the existing research, EIS sensors showed low LOD for identifying HMI concentration ranging from 100pM to 1nM, which is competitive with ASV. Furthermore, there are some possibilities to overcome the drawbacks of ASV with EIS sensors for HMI detection in aqueous solution, including pH control and electrode selection.

1.4. Research questions of this project

This project aims to expand the previous research done by TWTG regarding materials recognition in water-based solution with electrochemical impedance spectroscopy. In addition to finding predictable patterns in the impedance response that can be used to analyze the solution's ionic composition, the physical interpretation of the electrochemical system under the influence of changing parameters should be proposed for further development of the EIS sensor. Finally, the electrode's surface variation after EIS measurements should be studied to establish the equivalent circuit models. The research targets of this project can be summarized in the following questions:

1. By analyzing the EIS data, can an unknown HMI be identified, including its type and concentration, in a water-based salt solution?
2. Can the type and concentration of each HMIs be identified in a mixed HMI solution based on the fingerprint of each HMI?
3. What is the quantified influence of temperature on the EIS result?
4. What physical meaning can be extracted from the EIS data and the surface analysis on the working electrode?
5. What would be the equivalent circuit model that can describe and predict the electrochemical system of HMI detection?

In chapter 2, the research methodology is explained in further detail, including the construction of electrochemical cells, the procedure of conducting EIS measurements, and the preparation before surface analysis. In chapter 3, the results of the experiments and modelling/data fitting are presented, analyzed, and discussed in great details, while the research questions listed in this section are answered in chapter 4 by concluding the extent of the research. Finally, in chapter 5.1, the improvement of the experimental methods and the validity of the results are discussed, and future recommendation for the development of EIS sensor is suggested in chapter 5.2 as well as the proposal of EIS sensor prototype.

2

Materials and Methodology

In this chapter, the methodology of this research and the materials/instruments that were used are explained in detail. The overview of the research is illustrated in figure 2.1. First of all, different designs of electrochemical cells were constructed, and then the impedance data from different sets of EIS measurements were collected. The EIS measurements include five main subjects, which are (1) variation of concentration and types of HMIs, (2) variation of the mixing ratio in a mixed HMI solution, (3) variation of temperature, and (4) variation of electrochemical cell designs, and (5) detection of HMI solution in real water samples. After the EIS results were analyzed, the surface analysis on the working electrode was conducted to extract valuable information for the physical interpretation of the EIS result. Finally, the equivalent circuit model (ECM) based on surface analysis and literature study was proposed for data fitting.

2.1. Configuration of the electrochemical cell

To perform the EIS measurement repeatedly without changing the physical parameters during the process, an electrochemical cell that has a fixed setting is needed. The parameters that need to be taken into account here include the distance between each electrode, the exposed surface area of the electrode, and the dipping depth of the electrode into the electrolyte. In this research, a three-electrode system was used, which consist of a working electrode (WE), a counter electrode (CE), and a reference electrode (RE). During the EIS measurement, the AC voltage was applied on both WE and CE, while the output signal was measured between RE and WE. In this research, there were five different designs of the electrochemical cells being made, which includes the standard design, two modified designs for the investigation of the inductive loop (see section 3.1.1), and two modified designs for surface analysis.

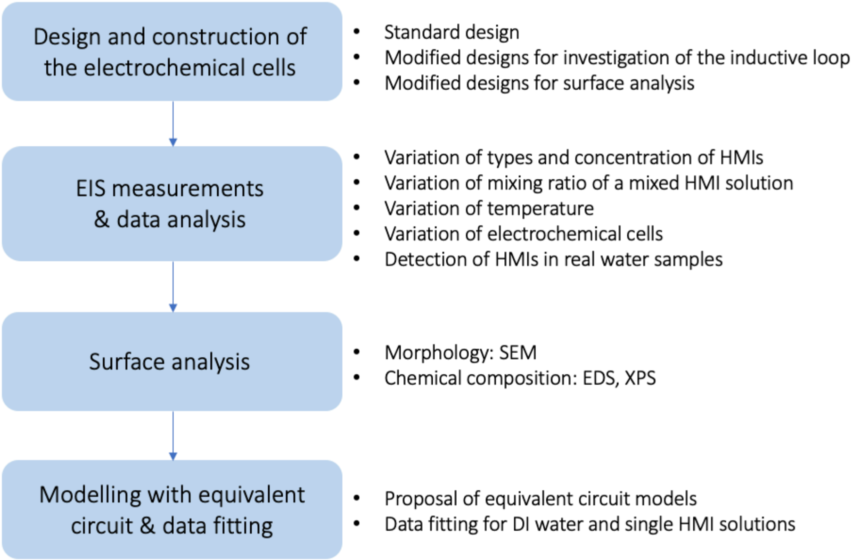

Figure 2.1: Overview of the research.

2.1.1. The standard design

Pure platinum (Pt) wire was chosen to be the material for both working and counter electrodes in the standard design due to its chemical and electrical properties. It is an inert metal that has excellent resistance to corrosion and electrical conductivity. It is widely used in laboratory equipment and often used as the electrodes in the electrochemical system. For the reference electrode, the saturated calomel electrode (SCE) was chosen due to its availability and stability.

Figure 2.2 illustrates the geometry and dimension of the standard design. Two platinum wires with 1cm length and 1mm diameter were connected with copper cable without soldering before being embedded in an acrylic resin holder by cold mounting. During the cold mounting process, ClaroCit powder (dibenzoyl peroxide) and ClaroCit liquid (methyl methacrylat and tetramethylene dimethacrylate) supplied by *Struers ApS* is taken in a 2:1 ratio and mixed. In addition, an extra plastic rod with 7.5 mm diameter was covered with silicone oil and installed in the setting, which helped create a hole for the insertion of RE after removal.

After the acrylic resin was fully dried in a high-pressure environment to prevent the formation of air bubbles, the bottom of the holder was sanded with SiC sandpapers, with the numbers of P80, P180, P320, P800, P1200, P2000. After grinding, the bottom of the holder was polished with fine diamond particles with the size of $3\mu m$ and $1\mu m$ until a mirror-like surface was reached. After polishing and before the EIS measurements, the acrylic resin holder was finally cleaned with demi water and isopropanol and dried with an air gun.

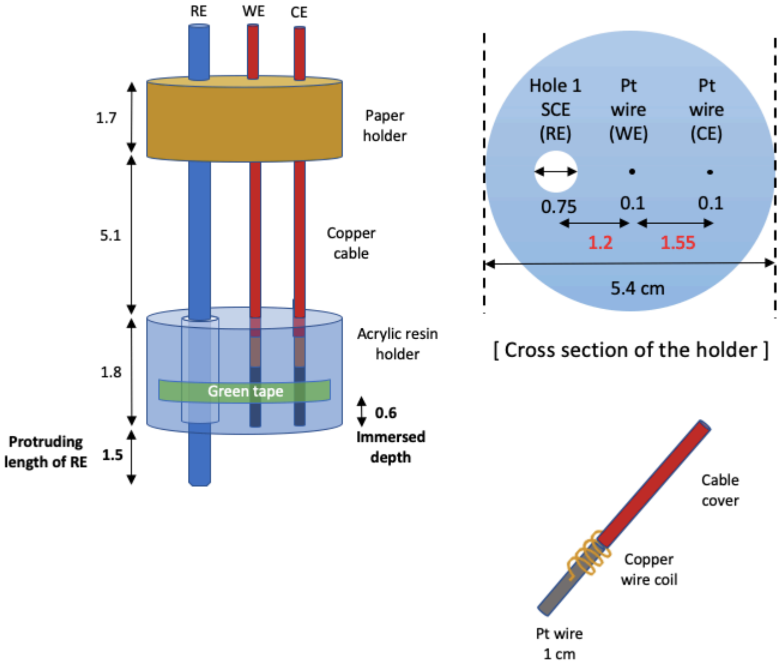

Figure 2.2: Schematic of the standard design.

This kind of design makes sure that the distance between each electrode is fixed at all times. It is worth noting that the distance between each electrode was set bigger than 1cm to reduce the effect of stray capacitance, which may result from the storage of the electric charge between platinum/copper wires. In addition, the distance between the WE and the RE was held closer than that between the WE and the CE. This design aims to decrease the ohmic losses due to the residual solution between the WE and RE [62]. Another parameter to be fixed is the dipping depth of the electrodes into the solution, and it was made possible by marking the position with green tape.

2.1.2. Modified designs for the investigation of the inductive loop

In order to investigate the appearance of the inductive loop in the Nyquist impedance plot (see section 3.1.1), two modified designs of the electrochemical cells were made. The first modified design is almost the same as the standard design, except that the connection between the copper wire and the platinum wire was made by soldering with tin, as shown in figure 2.3. The change is to eliminate the possibility that the inductive behavior in the EIS result comes from the copper coil at

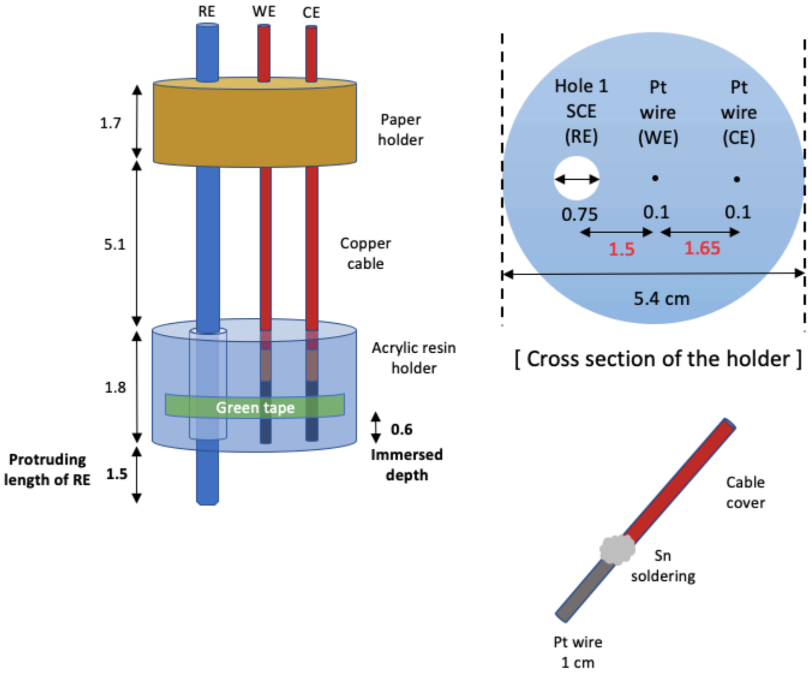

Figure 2.3: Schematic of the modified design with soldered connection.

the connection point. Another difference between the standard design and the first modified design is the distance between electrodes. This inevitable movement of the electrode's position was caused by volume change during the acrylic resin's solidification.

The second modified design involves replacing the SCE with another platinum wire, as shown in figure 2.4. This design was made to investigate the impact of reference electrode on the inductive behavior as well as the feasibility of the EIS sensor prototype (see chapter 5.2). Using the same materials for all three electrodes makes it easier to fabricate the EIS sensor in the form of chips. The mass production of the sensor chip can be realized by depositing the desired materials on a wafer and cut it into pieces. As mentioned previously, the deviation of the distance between electrodes was caused by the drying process of the acrylic resin.

2.1.3. Modified designs for the surface analysis

In order to meet the sample size requirement for the surface analysis, removable platinum thin foil with 1.2cm x 1.2cm surface area was used as the WE instead of the platinum wire embedded in the resin. After the EIS measurement, the Pt thin

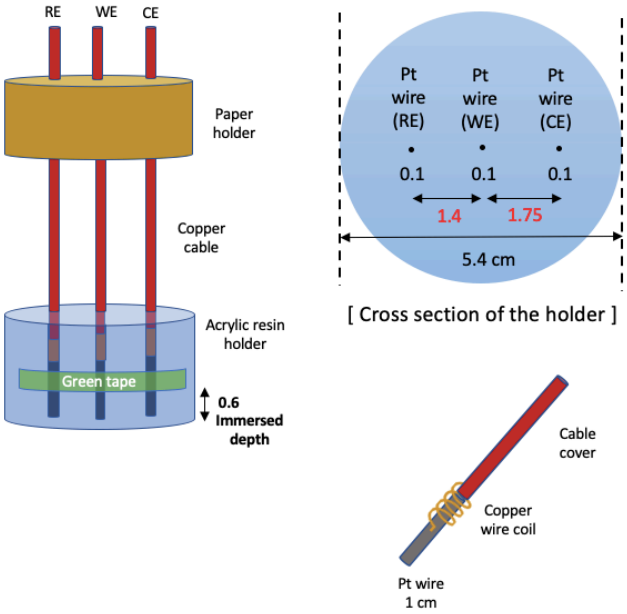

Figure 2.4: Schematic of the modified design with Pt wire as the RE.

foil was removed from the acrylic resin holder and fitted into the chamber of the scanning electron microscope (SEM) and X-ray photoelectron spectroscopy (XPS).

Before ordering the alternative Pt foils, the Pt wire cross-section was examined first with XRD, and the result is shown in the appendix A. From the XRD analysis, it can be concluded that the Pt wire used in the standard design is 100% pure platinum. Therefore, platinum foil with the highest purity (99.99+%) was ordered from *Goodfellow Cambridge Limited*. The thickness of the ordered Pt thin foil was 0.125mm, and the size is 25mm x 25mm. The analysis for the impurity in the product (ppm) includes Al 1, B 1, Ca 2, Au 1, Fe 4, Mg 1, Mo 1, Ni 1, Pd 7, Ru 3, Ag 2, Te 3, Zr 6.

The surface of the Pt foil was already polished and cleaned by the supplier. After purchase, it was cut into pieces with a surface area of approximately 1.2cm x 1.2 cm (±0.1cm). However, during the research, the Pt thin foils were reused during the repetitive experiments. Thus, after the first usage, they were polished again with diamond particles and cleaned with an ultrasonic bath when being immersed in isopropanol.

Two different designs were being made for the surface analysis, as shown in figure 2.5. In both cases, the back of the Pt thin foil was connected with a copper tape, which was fully sealed with non-conductive green tape to prevent leakage.

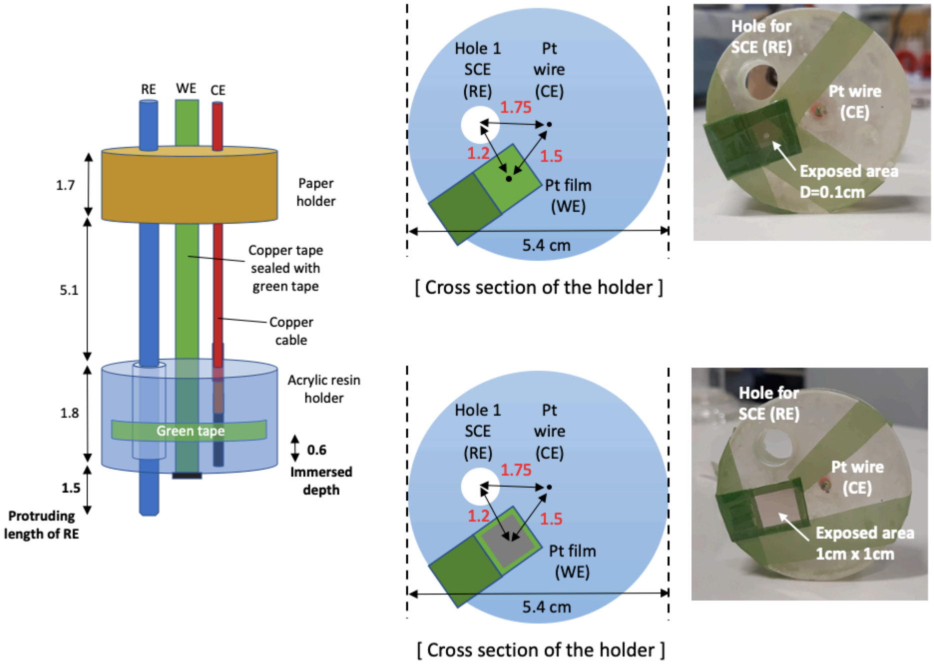

Figure 2.5: Schematic of the modified design with Pt thin foil as the WE.

The WE' surface of the first design was fully covered with green tape, except a round surface with 1mm diameter was exposed to the solution. This design is to mimic the exposed surface area in the case of the standard design. The second design increased the exposed surface area to 1cm x 1cm (±0.1cm). It is worth noticing that the edge of the Pt foil in the second design was also covered with green tape to avoid the leakage of the solution from the edge.

2.2. HMI solutions

In this project, zinc (Zn) and lead (Pb) ions are chosen to be the main research target for detecting HMIs. Zinc is a naturally abundant material in the earth's crust and serves as an essential element for human beings due to its multiple roles in DNA and RNA metabolism. Deficiency of zinc can cause problems to prenatal and postnatal development [63]. However, due to industrial development and human activities, especially the mining process, the disposal of commercial products containing zinc, and steel processing, the appearance of zinc in the groundwater and soil is rising unnaturally. It can cause health problems when zinc concentration is too high in the drinking water [64]. As for lead, it is considered one of the most toxic heavy metals and can affect almost every organ inside human bodies, especially the nervous system [65]. It was found that lead has no physiological role in the human body and can lead to DNA damage and cell membrane [66]. Pollu-

Table 2.1: Information of the HMI solution provided from the supplier.

Salt	**Contained ions**	**Bottle 1**	**Bottle 2**	**Bottle 3**
$Pb(NO_3)_2$	-	0.800 g/L	1.600 g/L	3.200 g/L
	Pb^{2+}	500 ppm	1000 ppm	2000 ppm
	NO^{3-}	300 ppm	600 ppm	1200 ppm
$ZnSO_4$	-	1.234 g/L	2.468 g/L	4.936 g/L
	Zn^{2+}	500 ppm	1000 ppm	2000 ppm
	$SO4^{2-}$	734 ppm	1468 ppm	2936 ppm

tion of lead may come from the production of lead-acid batteries, leaded gasoline pipelines, and metal recycling and foundries [67]. The threshold for zinc and lead concentration in the drinking water, set by WHO, can be found in table 1.1.

The solutions containing zinc ions and lead ions were prepared by dissolving zinc sulfate monohydrate ($ZnSO_4 \cdot H_2O$) and lead nitrate ($Pb(NO_3)_2$) in pure water. The HMI stock solutions with three different kinds of concentration were ordered from *Specs Compound Handling B.V*, as shown in table 2.1. During the EIS measurements, the tested samples were prepared by diluting these stock solutions with deionized water (Milli-Q water) available in TU Delft's laboratory.

2.3. Procedure of the EIS measurements

The EIS measurements were conducted with the *BioLogic*'s VSP-300 potentiostat, and the results were recorded in EC-Lab® software. After the data was collected, it was transferred to Microsoft Excel and ZView® software for further analysis and modeling. During the measurements, the frequency was swept from 1MHz to 100mHz, while the amplitude of voltage excitation was set at 10mV. In addition, 15 points per decade in the frequency range were recorded. It is worth noting that the voltage is set at a small value to maintain the equilibrium state and pseudo-linear response of the system and avoid the scaling effect from the distortion of the generated current curve. However, it should be noted that the voltage excitation should not be too small. Otherwise, the signal to noise ratio (S/N) may increase as well.

The repetitive EIS measurements were operated in the following manners:

1. Polished the surface of electrodes with $1\mu m$ and $3\mu m$ diamond particles.
2. Cleaned the surface of electrodes with demi-water and isopropanol and dried them with an air gun.
3. Poured 100ml of the designated HMI solution into a 250ml beaker and immersed the beaker in water-filled in the thermostat bath. The thermostat

bath temperature was regulated with the thermofluids provided by *Huber Kältemaschinenbau AG*, which has good heat transfer properties.

4. Immersed one of the electrochemical cells (illustrated in section 2.1) in the HMI solution with a fixed immersing depth, as shown in figure 2.6. The SCE was rinsed with deionized water before usage to wash away 3M KCl solution residue on the surface.

5. Connected the electrochemical cell with the potentiostat and closed the Faraday cage to avoid interfering signals from other electronic devices.

6. Waited for extra 5 minutes for temperature control. It is worth notice that the thermostat bath has been turned on for at least 10 minutes before the experiment to create a thermally stable environment. However, there was a ±0.3°C errors shown in the thermostat bath's control panel when the temperature was set at a fixed value.

7. Conducted the open-circuit voltage (OCV) measurement for 3-5 min. This step was to make sure that the system is in the equilibrium state before conducting EIS measurement.

8. Conducted the EIS measurement.

9. Wiped the surface of electrodes with an ultra-fine cloth and refilled the beaker with a new batch of HMI solution.

10. Repeated the same measurement with all the fixed parameters for at least three times. The repetition is to collect enough data for calculating standard deviation and showing the reproducibility of results.

As mentioned previously, there are five subjects regarding the EIS measurements, including:

- **Variation of type and concentration of HMIs**: This was done by changing the concentration of a single HMI solution ($ZnSO_{4(aq)}$ or $Pb(NO_3)_{2(aq)}$) from 5ppm, 10ppm, 20ppm, 50ppm, to 100ppm, while the temperature is fixed at 20°C during EIS measurements.

- **Variation of mixing ratio in a mixed HMI solution**: This was done by mixing 5ppm $ZnSO_{4(aq)}$ and 5ppm $Pb(NO_3)_{2(aq)}$ together with different mixing ratio, including 100%, 75%, 50%, 25%, and 0% of $ZnSO_{4(aq)}$, while the total volume of the mixed HMI solution was fixed at 100ml. The temperature was fixed at 20°C during EIS measurements. In addition, the same measurement was done for 50ppm case.

- **Variation of temperature**: The effect of changing temperature on the EIS result were investigated in four cases, which includes 5ppm $ZnSO_{4(aq)}$, 50ppm $ZnSO_{4(aq)}$, 5ppm $Pb(NO_3)_{2(aq)}$, and 50ppm $Pb(NO_3)_{2(aq)}$. The temperature under investigation ranged from 10°C to 30°C, with 5°C deviation in between.

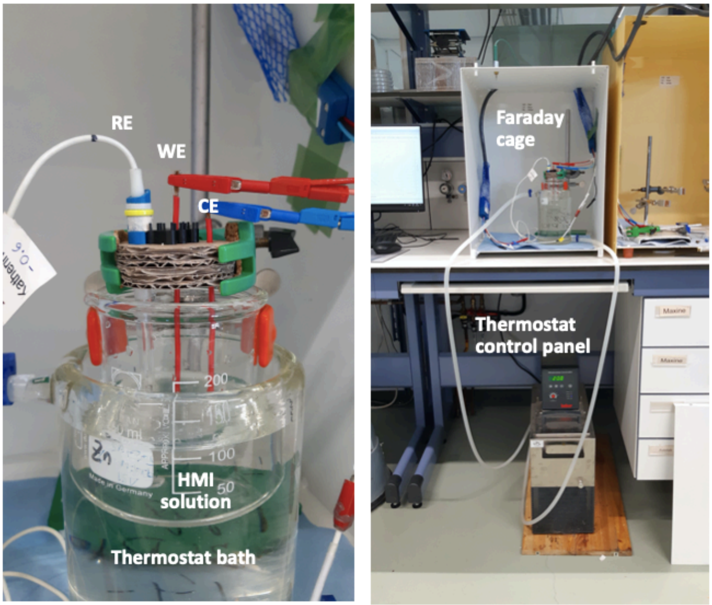

Figure 2.6: Setup for the EIS measurements.

- **Variation of the electrochemical cells**: The EIS results for five different electrochemical cells mentioned in section 2.1 were compared and analyzed in three cases: deionized water, 50ppm $ZnSO_{4(aq)}$ and 50ppm $Pb(NO_3)_{2(aq)}$, while the temperature was fixed at 20°C during measurements.

  There are multiple purposes to investigate the differences between various designs. One of the main goals is to understand if the inductive behavior comes from the geometry or the physical arrangement of the cell. However, it is also essential to know that if the SCE can be replaced by platinum wire. This information is essential for evaluating if the EIS sensor prototype can be produced by using the same materials for all electrodes. In addition, since an alternative Pt thin foil was used for surface analysis rather than the original Pt wire used in standard design, it is important to compare the EIS results of the two cases and discuss if they are comparable to each other.

- **Detection of HMIs in real water samples**: In addition to pure DI water and HMI solutions that were prepared with DI water, the EIS results of real water samples and their impedance response under the addition of $ZnSO_{4\,(aq)}$ were investigated. The purpose of this experiment is to test the practicality of the EIS sensor in the real water environment. The real water samples are listed in table 2.2. The industrial water was provided by one of the collaborators in this project and was collected during the stage of waste water treatment. The temperature was fixed at 20°C during EIS measurements, and

Table 2.2: List of real water samples and the overall concentration of Zn^{2+} inside the solution.

Real water samples	**Concentration of Zn^{2+}**
100% Tap water	-
90% Tap water + 10% 2000ppm $ZnSO_{4\ (aq)}$	200 ppm
100% Industrial water	-
90% Industrial water + 10% 2000ppm $ZnSO_{4\ (aq)}$	200 ppm
80% Industrial water + 20% 50ppm $ZnSO_{4\ (aq)}$	10 ppm

the total volume of solution was fixed at 100ml.

Except the investigation on differences between various electrochemical cells, all the other EIS measurments were conducted with the standard design, as shown in figure 2.2.

2.4. Surface analysis

In order to obtain more information about the electrochemical reactions on the surface of the working electrode, for instance, the deposition of certain compounds, the surface of the working electrode was examined with scanning electron microscopy (SEM), energy dispersive X-Ray spectroscopy (EDS), and X-ray photoelectron spectroscopy (XPS) before and after EIS measurements. The result of the surface analysis can provide information for further interpretation of the EIS data and the development of equivalent circuit models.

2.4.1. SEM/EDS analysis

A scanning electron microscope (SEM) is a microscope that acquires images and chemical composition of the materials by scanning focused electrons. The accelerated electrons with high kinetic energy interact with the materials and generate a variety of signals, including secondary electrons, back-scattered electrons, and characteristic X-ray [68]. Depending on the acceleration voltage of the electron beam, the injected electrons penetrate the materials within the depth of $1\mu m$-$3\mu m$, and various signals are emitted from different depths of the materials. For instance, the signal of secondary electrons is emitted from the depth of 10nm [69], which is very close to the surface of the material, while the characteristic X-ray is emitted from the depth of $1\mu m$. The morphology and topography of the materials are examined by the detection of secondary electrons, while the determination of elemental composition relates to the detection of characteristic X-ray and is called energy-dispersive X-ray spectroscopy (EDS). Depending on the accelerating voltage of the electrons and the spot size of the electron beam during the experiment, the resolution of the full-sized SEMs ranges from 1 to 20 nm, while the table-top system ranges from 20nm onwards [70].

During the research, the morphology of the WE's surface was first examined with JSM-IT100 InTouchScope™ scanning electron microscope, provided by *JEOL*

Ltd.. After the surface images were taken, specific points on the surface were chosen, and point EDS was conducted. The acceleration voltage of the electron beam was set at the range of 10kV-20kV during the investigation.

There were seven samples of Pt thin foil in total that have been examined with the SEM/EDS analysis. The description of samples are listed in table 2.3. As mentioned previously in chapter 2.1.3, since the Pt thin foils were reused repeatedly during the research, they were polished repeatedly with fine diamond particles after the first usage, which leads to two different surface conditions. In addition, there were two kinds of processes being implemented, including the case of short immersion and long immersion. In the case of short immersion, three repetitive EIS measurements were conducted with the standard procedure, as mentioned in chapter 2.3. After that, the surface of WE was dried with nitrogen gas to prevent pollution from the air. In the case of long immersion, the WE was continuously immersed in the HMI solution while cycles of OCV and EIS measurements were taken place. The total immersion time, in this case, was approximately 3 hours. Similarly, the sample was dried with nitrogen gas instead of an air gun in the end.

There were two kinds of electrode designs used in this experiment, in which the Pt thin foil has a small or large exposed surface area. The details of the electrode design are shown in figure 2.5.

2.4.2. XPS analysis

X-ray photoelectron spectroscopy (XPS) is a surface-sensitive technique based on the principle of the photoelectric effect. By irradiating the materials with a beam of X-ray and measuring the kinetic energy of the emitted electrons, the binding energy (E_{BE}) of each electron can be calculated, as shown in equation 2.1, where ϕ represents the work function of the surface of a specific material [71]. Since each element has its own characteristic electron configuration, the elemental composition on the materials can be obtained and quantified by plotting the number of emitted electrons at every specific binding energy. Additionally, since the binding energy of the emitted electron also depends on the orbital where the electron is ejected from, XPS also gives information about the chemical states of the elements and their bonding.

$$E_{BE} = E_{photon} - (E_{kineitc} + \phi) \tag{2.1}$$

The XPS analysis in this research was carried out using a PHI-TFA XPS spectrometer equipped with an x-ray Al-monochromatic source. The pressure of the vacuum state during XPS analysis was 10^{-9} mbar. The analyzed area was 0.4 mm in diameter, and the analyzed depth was 3 to 5 nm. Narrow multiplex scans of the peaks were recorded using a pass energy of 23.5 eV with a step size 0.1 eV, at a take-off angles of 45 °with respect to the sample surface. Low energy electron gun was used for surface charge neutralization XPS. After acquiring the data, the spectra were processed using Multipak v8.0 software. Both the spectrometer and

Table 2.3: List of samples examined by SEM/EDS analysis.

No.	Surface condition of the Pt foil (WE)	Exposed area to the HMI solution	HMI solution	Process	Total immersion time
1	Original state	-	-	-	-
2	Repolished	-	-	-	-
3	Original state	Circle, D=1mm	50ppm $ZnSO_4$ (aq)	3 repetitive EIS measurements, discontinuous immersion	~45 min
4	Original state	Circle, D=1mm	50ppm $Pb(NO_3)_2$ (aq)	3 repetitive EIS measurements, discontinuous immersion	~45 min
5	Repolished	Square, 1x1 cm	50ppm $ZnSO_4$ (aq)	3 repetitive EIS measurements, discontinuous immersion	~45 min
6	Repolished	Square, 1x1 cm	50ppm $Pb(NO_3)_2$ (aq)	3 repetitive EIS measurements, discontinuous immersion	~45 min
7	Repolished	Square, 1x1 cm	50ppm $ZnSO_4$ (aq)	6 repetitive EIS measurements, continuous immersion	~3 hr

Table 2.4: List of samples examined by XPS analysis.

No.	Surface condition of the Pt foil (WE)	Exposed area to the HMI solution	HMI solution	Process	Total immersion time
1	Repolished	-	-	-	-
2	Original state	Square, 1x1 cm	50ppm $ZnSO_4$ (aq)	3 repetitive EIS measurements, discontinuous immersion	~45 min
3	Original state	Square, 1x1 cm	50ppm $Pb(NO_3)_2$ (aq)	3 repetitive EIS measurements, discontinuous immersion	~45 min
4	Repolished	Square, 1x1 cm	50ppm $ZnSO_4$ (aq)	6 repetitive EIS measurements, continuous immersion	~3 hr
5	Repolished	Square, 1x1 cm	50ppm $Pb(NO_3)_2$ (aq)	6 repetitive EIS measurements, continuous immersion	~3 hr

the software were provided by *Physical Electronic Inc.*.

There were five samples in total that have been examined with the XPS analysis. The details of the samples are listed in table 2.4.

2.5. Modelling and data fitting

During the last stage of the research, several equivalent circuit models (ECMs) were proposed based on literature studies and surface analysis results. After the proposal of ECMs, the impedance data obtained from EIS measurements were fitted with the models by using ZView® software version 3.5h, provided by *Scribner Associates*. During the modelling process, different parts of the Nyquist impedance plot were fitted separately to find the approximate value for each circuit element, and the ultimate values were determined by simulation.

3

Results and Discussion

In this chapter, the results for experiments, data analysis, and modelling are presented and discussed. Associated literature is studied to support the reasoning behind the hypothesis and the interpretation of the results. Further discussion on the improvement of the experiments and the validity of the results will be discussed in chapter 5.1.

3.1. EIS measurements

In this section, the results of EIS measurements are presented for the five topics, as illustrated previously in figure 2.1. In the discussion of the first topic, which is the effect of varying types and concentrations of HMI, the interpretation of the Nyquist plot and physical meanings behind the impedance response are discussed in great detail. In contrast, in the other sections, the discussion focuses more on the influences of changing parameters on the impedance response, the reason behind these influences, and how they affect the EIS sensor's application.

3.1.1. The effect of varying types and concentration

In this section, the influence of varying types and concentrations of HMI on the impedance response was investigated. Figure 3.1 shows the Bode impedance plot for zinc sulfate solution, while figure 3.2 shows the Bode impedance plot for lead nitrate solution. In both cases, when the concentration of the HMI increases, the overall impedance value decreases. However, different behaviors were observed in different frequency regions. For instance, in the case of $ZnSO_4$ $_{(aq)}$ and $Pb(NO_3)_2$ $_{(aq)}$, there were two peaks of impedance fluctuation presented in the high frequency region (10^4 Hz - 10^6 Hz), one being the local maximum point and the other one being the local minimum point. In contrast, the fluctuation peaks didn't appear in the case of DI water. In addition, for the case of HMI solutions, the impedance value significantly increased in the low-frequency region (10 Hz - 0.1 Hz) as the frequency decreased, creating steep lines with different slopes, while in the case of DI water, the impedance value remained the gradual increase with only a slight change in gradient near 0.1 Hz.

One of the similarities between the case of DI water and two HMI solutions were the starting point at high-frequency region (10^6 Hz - 10^5 Hz). In all cases, the increase of impedance in this frequency region followed the same linear line before reaching a plateau in the mid-frequency region. In the mid-frequency region (10^3 Hz - 100 Hz), the impedance value increased slightly but gradually, creating a stable plateau region that marks the difference of impedance between DI water and HMI solutions at various concentration.

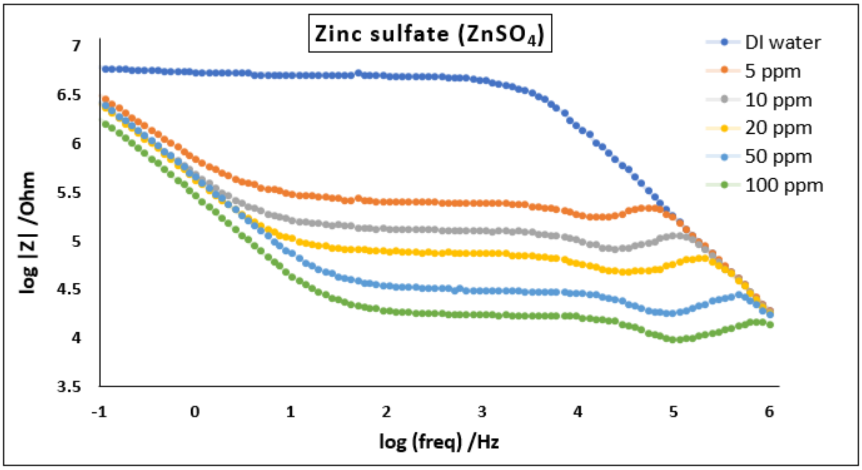

Figure 3.1: Bode impedance plot of $ZnSO_{4\ (aq)}$ for different concentrations at 20 °C.

(1) Data analysis on Bode impedance plot

In order to compare the impedance response of the two HMI solutions, two characteristic points in the high-frequency region (10^6 Hz - 10^4 Hz) were selected, including the local maximum and local minimum point. These two characteristic points were re-plotted on the Bode impedance plot again with error bars added on them, as shown in figure 3.3. The error bar represents the data's standard deviation, which indicates how widely the data points are dispersed from the average value in three repetitive experiments. The standard deviation was calculated with the "STDEV.S" function in Microsoft Excel, as shown in equation 3.1. $\overline{x}$ represents the average value of impedance, and n represents the number of data points. It is worth noting that the impedance values mentioned so far were plotted on a logarithmic scale rather than a linear scale.

$$f(x) = \sqrt{\frac{\sum(x-\overline{x})^2}{(n-1)}} \tag{3.1}$$

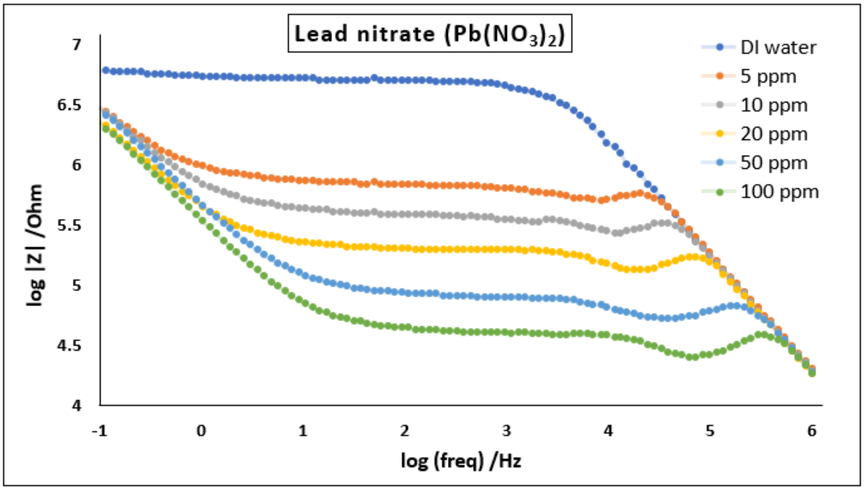

Figure 3.2: Bode impedance plot of $Pb(NO_3)_2$ $_{(aq)}$ for different concentrations at 20 °C.

The result in figure 3.3 shows that the two characteristic points varied their position on the Bode impedance plot according to a linear trend line. For the local maximum points, the points for $ZnSO_4$ $_{(aq)}$ and the points for $Pb(NO_3)_2$ $_{(aq)}$ almost align on the same linear trend line. However, for the local minimum points, the slope of the two trend lines are slightly different.

The result indicates that at the same concentration, each HMI solution has its own characteristic impedance value. When the concentration is doubled, the impedance value in the log scale varies along the linear trend line for an approximately fixed distance. It is worth noting that the local maximum and local minimum points for a HMI solution appear at a different frequency when the concentration varies. Despite of their characteristic impedance values, the point for 50ppm $Pb(NO_3)_2$ $_{(aq)}$ and the point for 20ppm $ZnSO_4$ $_{(aq)}$ almost overlap with each other. Therefore, further modeling is required to distinguish the two ions by the identification of different equivalent circuit elements.

As for the reproducibility of the result, the standard deviation for three repetitive measurements is presented in both X-axis and Y-axis. The scale of the error bar implies that the reproducibility of the results is high. This stability of the system provides the foundation for the future development of the EIS sensor.

In order to quantify the impedance change of each HMI solution corresponding to DI water, the impedance value in log scale at 317 Hz (log(freq.)=2.5) was selected and compared, as shown in figure 3.4. The point in the mid-frequency region was chosen to represent the average of the whole impedance spectrum. In addition, during the experiments, the plateau region was found to be the most sta-

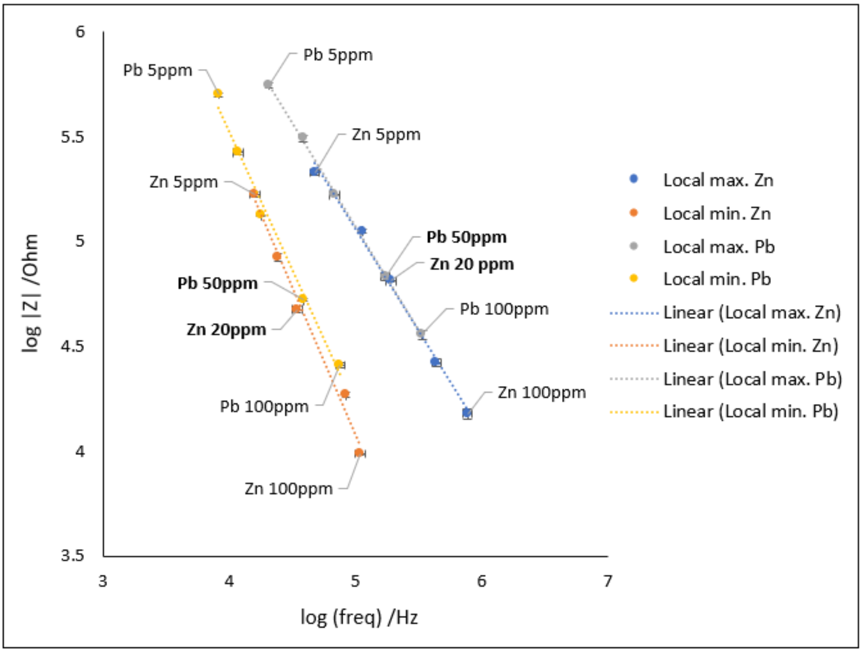

Figure 3.3: Characteristic points on the Bode impedance plot, representing the fluctuation of impedance in the high-frequency region.

ble region across the entire impedance spectrum. The result indicates that when the concentration is doubled, the change in impedance values in the log scale increases 3.7-4.3% (=4%±0.3%) for both HMI solutions. Additionally, at the same concentration, the difference in impedance change between the two HMI solution is 5.6-7.0% (=5.8%±0.2%).

During data analysis, the Bode phase shift plots and the slope of steep lines in the low-frequency region of the Bode impedance plot were also investigated. However, no significant patterns were found in the analysis. The Bode phase shift plot for the two HMI solution are shown in appendix C.

(2) Interpretation of Nyquist impedance plots

By analyzing the shape of the impedance spectrum in the Nyquist impedance plot, it is possible to obtain clues about the physical interpretation of the system. Although without further investigation of the electrochemical process on the electrode surface, solid conclusions cannot be made by simply observing the impedance response, possible equivalent circuit elements can still be proposed for further development of modelling.

Figure 3.5 show the Nuquist impedance plot for $ZnSO_{4\ (aq)}$, and figure 3.6 is the magnified version of it near the origin. In the first figure, the impedance response

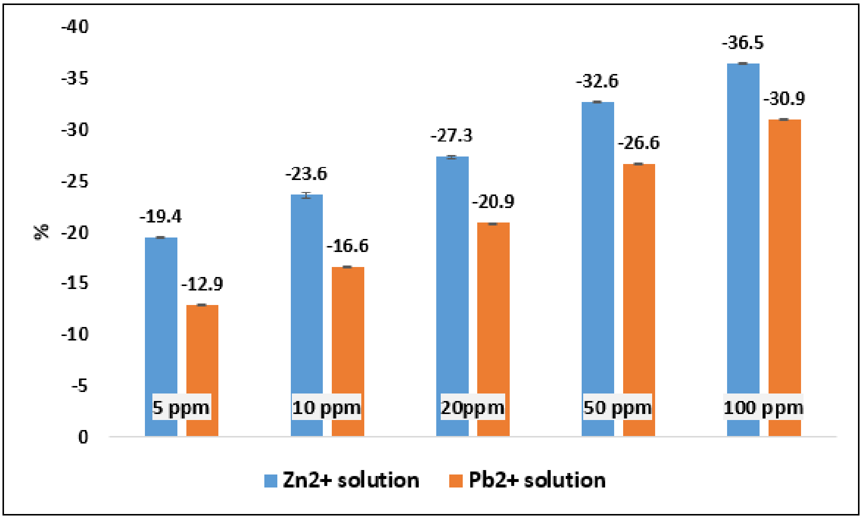

Figure 3.4: Impedance change in logarithmic scale at 317Hz compared to DI water.

of DI water is clearly shown. It has a depressed semicircle in the high frequency region and a steep line in low frequency region, indicating an element of Warburg impedance for the diffusion process. The data points are presented in the fourth quadrant, implying a typical parallel resistor–capacitor (R/C) circuit, with the ideal capacitor replaced by a constant phase element (CPE). As mentioned in chapter 1.2.3, this kind of system is controlled by both kinetic and diffusion process. The depressed semicircle, which appears in the high-frequency region, is attributed to the combination of charge transfer resistance and the double layer capacitance. The non-ideal behavior of the double-layer capacitance may be caused by various reasons, including surface roughness, non-uniform distribution of the current, and non-homogeneous reaction rate on the electrode surface [72].

It is worth noting that the high-frequency resistance (HFR) in this system is almost negligible. The phenomenon is clearly shown in figure 3.6, in which the data points of the first semicircle in the high-frequency region approach x-axis at the origin. The HFR consists of all the ohmic losses in the electrochemical system, including electrolyte resistance, the resistance of the electrode materials, and the resistance of cables or other circuit elements [54]. Since the platinum electrode and the copper cable are both highly conductive materials, the main contribution of HFR, in this case, is the ion flow resistance of the electrolyte. The extremely low value of HFR implies that the distance between the WE and RE is close enough so that the uncompensated resistance can be neglected.

In addition, in figure 3.6, it can be seen that the impedance response of zinc sulfate solution consists of two depressed semicircles, a spiral connection between the two depressed semicircles, and a steep line in the low-frequency region. The first depressed semicircle, as mentioned in the case of DI water, represents the combination of charge transfer resistance and double-layer capacitance. Since the system is non-ideal, the element of capacitors is replaced with constant phase elements. As the concentration increased, the size of the first depressed semicircle decreased. This implies the charge transfer resistance decreases when the concentration of HMI increases.

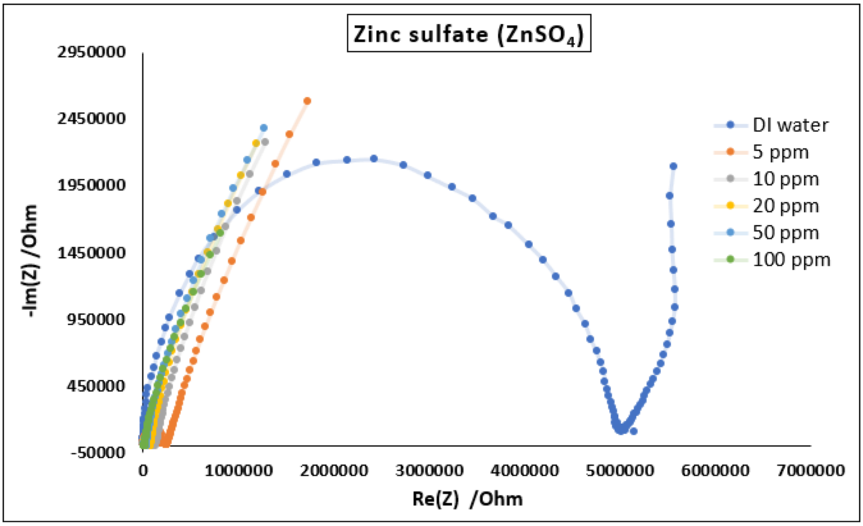

Figure 3.5: Nyquist impedance plot of $ZnSO_{4\ (aq)}$ for different concentrations at 20 °C.

Charge transfer resistance is related to the barrier of electron flow passing from the electrode surface to the adsorbed species and from the adsorbed species to the electrode surface [10]. The calculation of charge transfer resistance can be deducted from the Butler–Volmer equation as shown in equation 3.2, which expresses the relationship between net current density (i) and the overpotential (η) of the electrochemical system.

$$i = i_0(exp(-\frac{\alpha nF\eta}{RT}) - exp(-\frac{(1-\alpha)nF\eta}{RT})) \tag{3.2}$$

In the equation, i_0 represents the exchange current density at equilibrium, α represents the symmetry factor, and n represents the number of electrons involved in the reaction. The constant F and R represents Faraday's constant and the gas constant, respectively. Since the EIS measurement is conducted with a small perturbation of the AC voltage, the electrochemical system can be seen to be at equilibrium with small overpotential, and equation 3.2 can be simplified into equation 3.3.

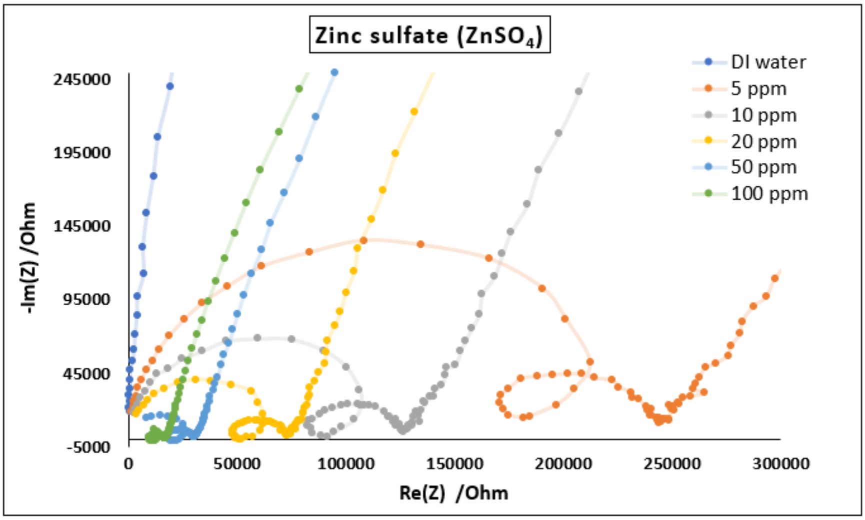

Figure 3.6: Magnified Nyquist impedance plot of $ZnSO_4$ $_{(aq)}$ for different concentrations at 20 °C.

$$i = i_0(\frac{nF\eta}{RT}) \tag{3.3}$$

Finally, the charge transfer resistance can be calculated by diving the overpotential with net current density, as shown in equation 3.4.

$$R_{ct} = \frac{\eta}{i} = \frac{RT}{nFi_0} \tag{3.4}$$

From the equation, it can be seen that the value of charge transfer resistance is closely related to the value of exchange current density (i_0). When the exchange current density increases, the charge transfer decreases. The exchange current density is defined as the intrinsic rate of electron transfer between the electrode and the electrolyte at equilibrium [73], and is controlled by several parameters, including the nature of the electrode materials, roughness/surface area of the electrode, the concentration of the reactant and product, and temperature [10]. The value of exchange current density can be estimated with equation 3.5. In the equation, K represents the electrochemical reaction rate, β represents the transfer coefficient of the reaction, while C_O and C_R represents the concentration of oxidant and reductant, respectively. The term A is the electroactive surface area rather than the total area of the electrode and is dependent on temperature.

$$i_0 = nFKAC_O(\frac{C_O}{C_R})^{-\beta} \tag{3.5}$$

At constant temperature, when the total concentration of the HMI solution increases, the conductive ions near the electrode surface also increases. This increase in conductive ions contributes to increased exchange current density and further decreases the charge transfer resistance. This similar pattern is also shown in the case of lead nitrate solution. Figure 3.7 shows the Nyquist impedance plot for $Pb(NO_3)_2$ (aq) at various concentration, the figure 3.8 is the magnified version of it near the origin. When the concentration of $Pb(NO_3)_2$ (aq) increases, the size of the first semi-circle in the Nyquist impedance plot decreases.

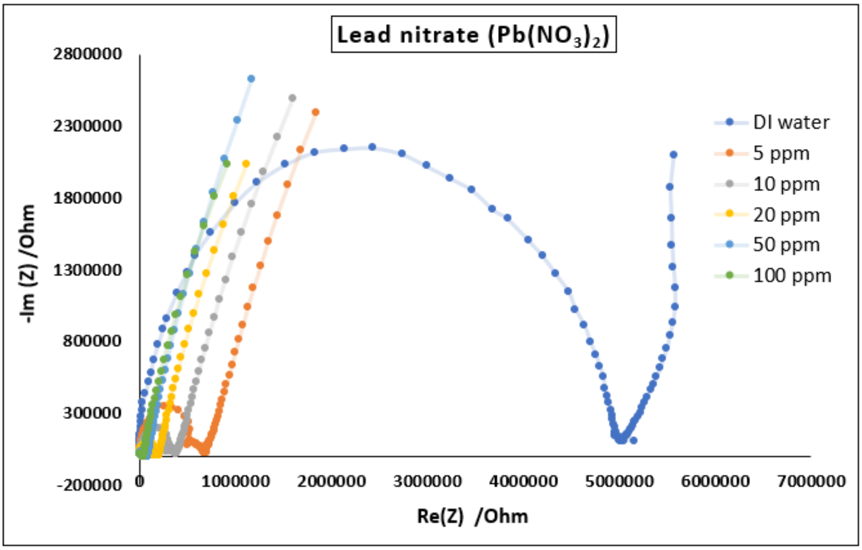

Figure 3.7: Nyquist impedance plot of $Pb(NO_3)_2$ (aq) for different concentrations at 20 °C.

Things that are worth investigating further for the two HMI solution cases include the inductive behavior and the presence of the second depressed semicircle. There are several hypotheses being proposed by researchers to explain the inductive behavior in the relatively low-frequency region, including the influence of electrical shielding (Faraday cage) [74], different components in cell designs (including springs, wiring, the presence of reference electrode) [75], and stray capacitance [76]. Aside from the arguments that attribute the inductive behavior to physical artifacts, some researchers believe that the inductive behavior in the relatively low-frequency region is associated with the adsorption and desorption process of the intermediate species. For instance, in the research done by Itagaki *et al.*, the inductive loop was explained by Faradaic process involving two steps of electron transfer and reaction intermediate of a dissolving iron electrode in an acidic solution. Equation 3.6 show the two-step reaction in which the metal element (M) is oxidized into metal ion ($M(II)$) via an adsorbed intermediate ($M(I)_{ad}$). In the equations, K_1 and K_2 represent the potential-dependent rate constants.

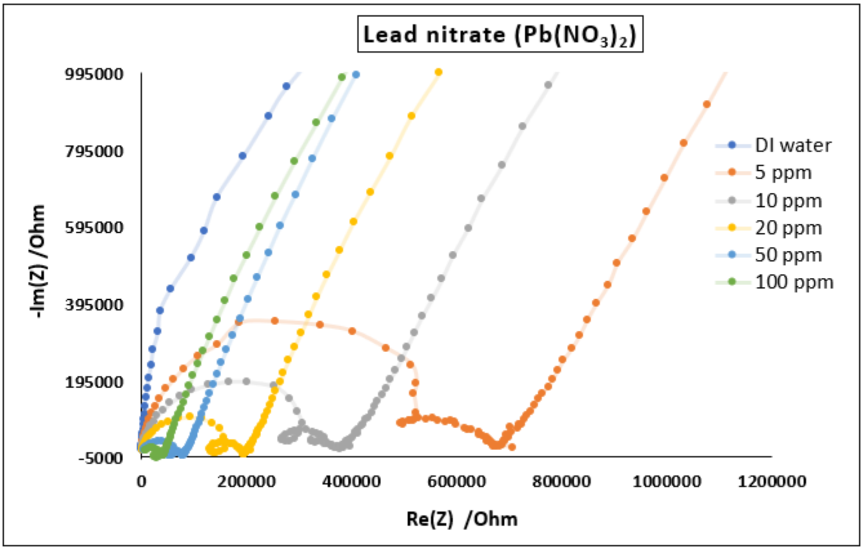

Figure 3.8: Magnified Nyquist impedance plot of $Pb(NO_3)_2$ $_{(aq)}$ for different concentrations at 20 °C.

$$\begin{gathered} M \xrightarrow{K_1} M(I)_{ad} + e^- \\ M(I)_{ad} \xrightarrow{K_2} M(II) + e^- \end{gathered} \tag{3.6}$$

In addition, in the research done by Harrington and Van den Driessche, the hydrogen evolution reaction (HER) was used as an example to derive the condition for inductive loop's appearance. It stated that the inductive behavior could only occur if two mechanisms of electron transfer are present simultaneously, including oxidation in the direction of adsorption and reduction in the direction of adsorption. This requirement can be realized if both the adsorption and desorption processes take place. Equation 3.7 shows the 3-step HER mechanisms, with $M(site)$ being the free adsorption sites on the surface of the electrode and $MH(ads)$ being the site with adsorbed H atom.

$$\begin{gathered} M(site) + H^+ + e^- \underset{K_{-1}}{\overset{K_1}{\leftrightarrows}} MH(ads) \\ MH(ads) + H^+ + e^- \underset{K_{-2}}{\overset{K_2}{\leftrightarrows}} M(site) + H_2 \\ 2MH(ads) \underset{K_{-3}}{\overset{K_3}{\leftrightarrows}} 2M(site) + H_2 \end{gathered} \tag{3.7}$$

Aside from HER, another possibility of having an adsorption/desorption process in the aqueous solution is the oxygen reduction reaction (ORR). In the research

Table 3.1: Measured pH value for DI water and HMI solutions and calculated thermodynamic potential

	pH before EIS	**pH after EIS**	**Thermodynamic potential (unit: V)**
Deionized water	7.9	7.8	anodic: 0.72 cathodic: 0.70
50ppm ZnSO4 (aq)	5.5	5.6	anodic: 0.58 cathodic: 0.56
50ppm Pb(NO3)2 (aq)	4.8	4.7	anodic: 0.54 cathodic: 0.52

done by Cruz-Manzo *et al.*, it was suggested that the produced intermediates during ORR account for the appearance of the inductive loop in the electrochemical system. Since platinum is a good catalyst for both HER and ORR, there is also a chance that these reactions took place during the EIS measurements when the solution's conductivity was high enough, and thus contribute to the appearance of inductive behavior.

In order to check the possibility of these reactions, the thermodynamic potentials versus reversible hydrogen electrode (RHE) for three solution cases are calculated with equation 3.8. The applied voltage in this case is 0.01V v.s SCE. The measured pH value and the calculated potential are listed in table 3.1. It is worth noting that the pH values for three solution cases show no significant changes before and after EIS measurements.

$$\begin{aligned} E_{RHE} &= E_{SHE} + 0.0591 \times pH \\ &= E_{SCE} + 0.244 + 0.0591 \times pH \end{aligned} \tag{3.8}$$

From the result, it can be seen that the calculated thermodynamic potentials for the three solution cases are lower than the thermodynamic potential of ORR (1.23V) in the standard condition [80]. In addition, the calculated thermodynamic potentials for the three solution cases are higher than the thermodynamic potential of HER (0V). Therefore, it is implausible that these reactions took place in the system significantly. Instead, the adsorbates are more likely related to HMI or other ionic species presented in the aqueous solution.

Another element to be noticed is the second depressed semicircle in the Nyquist impedance plot. Since there are two semicircles present, the system likely possesses two time constants, with the second one being the contribution from the adsorbate. In order to investigate whether an adsorption/desorption process took place during the EIS measurements and what kind of species might involve, more investigation on the surface of the WE was conducted with surface analysis techniques, and the results were discussed in section 3.2. In addition, the possible contribution of physical artifacts to the inductive behavior is further investigated in section 3.1.4, by the comparison of different cell designs.

The last component to be discussed in the Nyquist impedance plot is the Warburg element in the very-low-frequency region. The Warburg element is related to the diffusion process and can be recognized by the straight line with 45°slope. The value of Warburg impedance in the case of semi-infinite diffusion can be calculated with equation 3.9, where σ represents the Warburg coefficient (unit: Ωs^{-1}) and ω represent the angular frequency [10].

$$Z_w = \sigma\omega^{-1/2} - i\sigma\omega^{-1/2} \tag{3.9}$$

The Warburg coefficient is related to the diffusivity (D) and the bulk concentrations (C^∞) of the oxidized and reduced species, as shown in equation 3.10 . The notation of O and R in the equation represents the oxidized and reduced species, respectively [10].

$$\sigma = \frac{RT}{n^2F^2A\sqrt{2}}(\frac{1}{\sqrt{D_O C_O^\infty}} + \frac{1}{\sqrt{D_R C_R^\infty}}) \tag{3.10}$$

However, in real electrochemical systems, the diffusion condition is often a finite one due to natural boundaries or the electrode's thickness. The difference between the impedance response of finite systems and semi-infinite conditions is shown in figure 3.9. The value of Warburg impedance for finite systems are calculated with equation 3.11, where Z_{FLW} represent the finite length Warburg impedance, Z_{FSW} the finite space Warburg impedance, R_W the limiting diffusion resistance, and τ_D the diffusion time constant [15].

$$\begin{aligned} Z_{FLW} &= \frac{R_W}{\sqrt{i\omega\tau_D}} tanh(\sqrt{i\omega\tau_D}) \\ Z_{FSW} &= \frac{R_W}{\sqrt{i\omega\tau_D}} coth(\sqrt{i\omega\tau_D}) \end{aligned} \tag{3.11}$$

In the case of DI water, as shown in figure 3.5 and 3.7, the Warburg element first shows a transition region in relative high frequency region and then approaches finite space impedance near the lowest frequency (0.1 Hz). However, for HMI solutions, the impedance response near the lowest frequency is more similar to one in finite-length conditions. During the EIS experiments, the lines for the Warburg impedance near the lowest frequency in all cases were observed to be less stable than the impedance response in other higher frequency regions. Not only the deviation of the slope is larger, but also no significant pattern was found in the values of these slopes. In section 3.3, the values for Warburg impedance will be calculated with the help of modelling, and further discussion will be addressed.

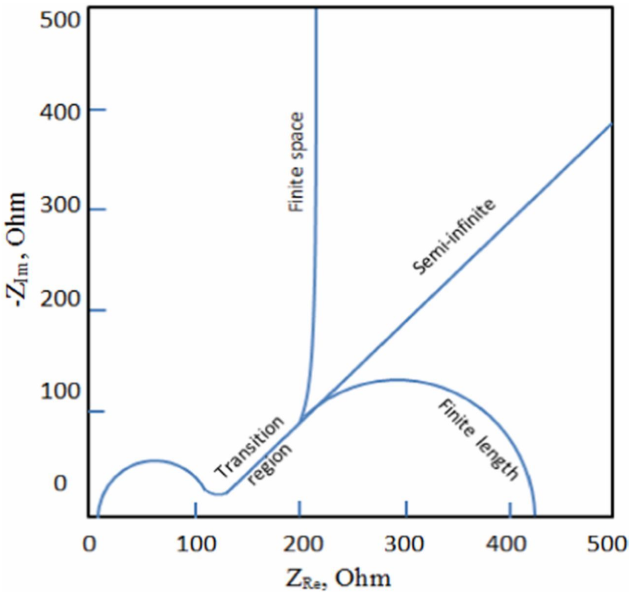

Figure 3.9: Different types of Warburg impedance on a Nyquist plot [15].

(3) Data analysis on Nyquist impedance plot

In order to compare the Nyquist impedance plot for the two HMI solutions, two characteristic points were selected on the Nyquist impedance plot. The first one is the highest point on the first semicircle (local maximum), representing the extent of charge transfer resistance. The second one is the starting point of the Warburg element in the low-frequency region, representing the sum of all non-diffusional resistance of the system (local minimum). These data points for the two HMI solutions are shown in figure 3.10. The results indicate that the decrease of charge transfer resistance follows a clear pattern as the concentration increases. When the concentration of an HMI solution doubled, the extent of charge transfer resistance becomes halved. In addition, at the same concentration, each HMI solution has its own characteristic value of charge transfer resistance. This result suggests that the concentration of an HMI solution is predictable if one of the data points of that solution is collected for a specific concentration, considering the linear relationship between the concentration and the extent of charge transfer resistance. However, the result also suggested that it is more difficult to distinguish different points for high concentration than for low concentration. The EIS sensor is thus more sensitive in the case of low concentration.

In addition, the points for 20ppm $ZnSO_{4\ (aq)}$ and 50ppm $Pb(NO_3)_{2\ (aq)}$ almost overlap with each other, as well as the points for 50ppm $ZnSO_{4\ (aq)}$ and 100ppm $Pb(NO_3)_{2\ (aq)}$. Further distinction of the two HMI solution thus relies on other types of data analysis or modelling rather than the selection of characteristic points. In

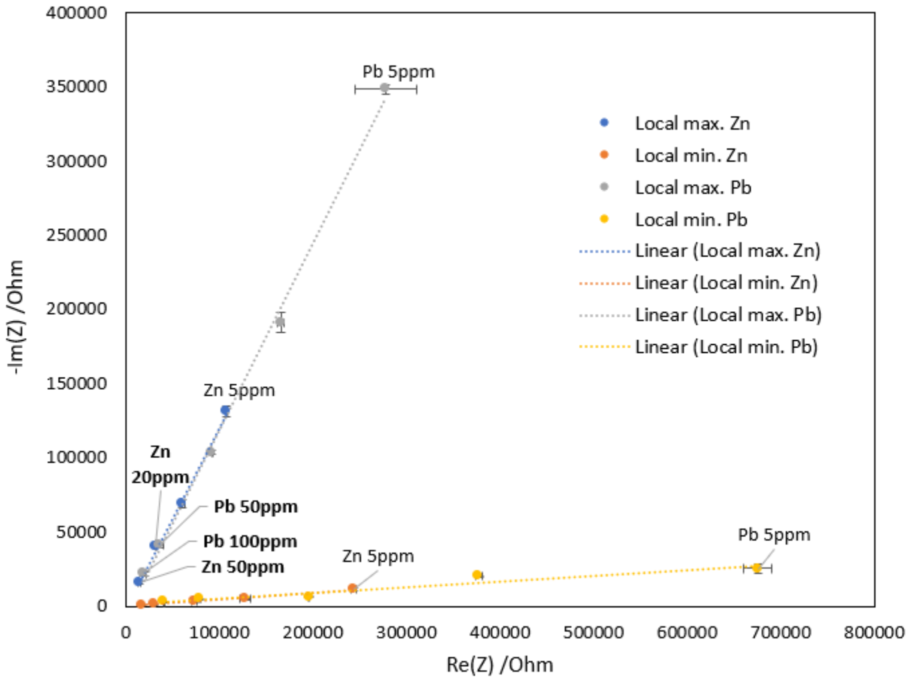

Figure 3.10: Characteristic points on the Nyquist impedance plot, representing the extent of charge transfer resistance (local max.) and the extent of non-diffusional resistance (local min.) of the electrochemical system.

section 3.3, the values of equivalent circuit elements for the case of 20ppm $ZnSO_4$ (aq) and 50ppm $Pb(NO_3)_2$ (aq) are compared and discussed.

3.1.2. The effect of varying mixing ratio of a mixed HMI solution

In this section, the EIS result for a mixed HMI solution with various mixing ratio is analyzed and discussed. It should be noted that the notation of concentration being used here refers to the concentration of each HMI solution before mixing. For example, the term ”5ppm mixed solution” indicates that the solution was mixed with 5ppm $ZnSO_{4\ (aq)}$ and 5ppm $Pb(NO_3)_{2\ (aq)}$ with different mixing ratio, ranging from 0% to 100% with 25% deviation.

Figure 3.11 shows the Bode impedance plot of 5ppm mixed HMI solution. The overall shape of the curve for the mixed solution is similar to the one in the single HMI solution. In both cases, the Bode impedance plot consists of two characteristic points (local maximum and local minimum) in the high-frequency region, a plateau in the mid-frequency region, and a steep line in the low-frequency region, which is associated with the diffusion process. However, the peak values of characteristic points of the mixed solution in high-frequency regions behave more modest compared to the ones in a single HMI solution.

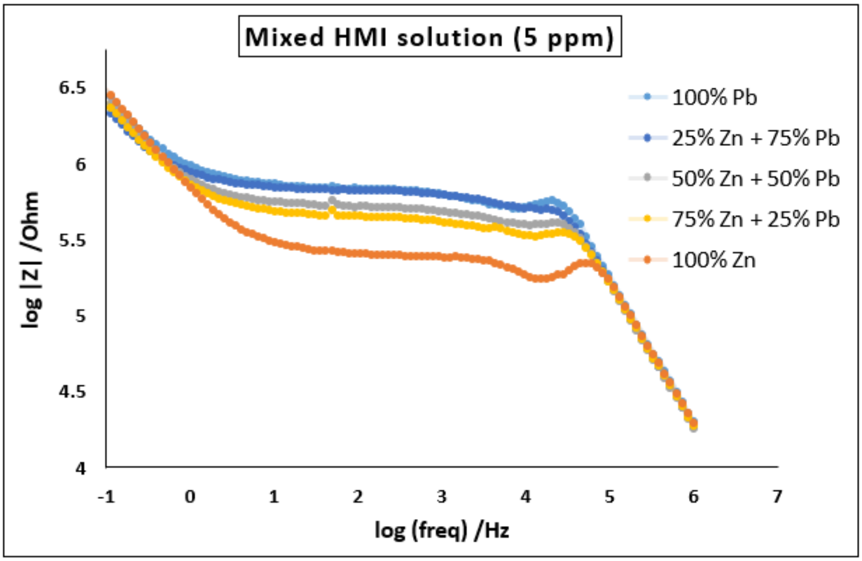

Figure 3.11: Bode impedance plot of 5ppm mixed HMI solution at 20°C.

For the case of 50ppm mixed HMI solution, as shown in figure 3.12, the shape of the curve in the Bode impedance plot is also similar to the ones for single HMI solutions. The line for the case of ”25% Zn + 75% Pb” appears to be discontinuous at log(frequency)=4.3 is due to the interruption of noise to the potentiostat. It is worth notice that the slope of the steep line in the low-frequency region for a mixed solution is smaller than the ones in a single HMI solution in both 5ppm and 50ppm cases.

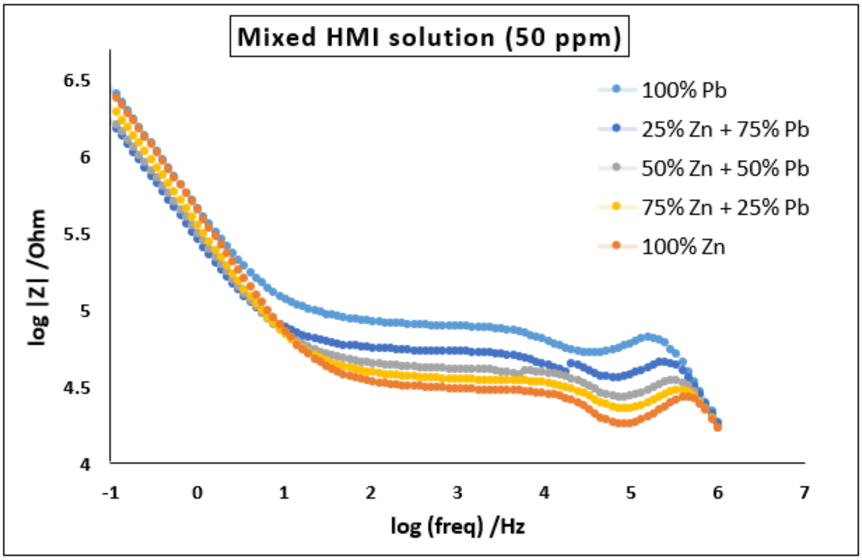

Figure 3.12: Bode impedance plot of 50ppm mixed HMI solution at 20°C.

(1) Data analysis on Bode impedance plot

In order to quantify and compare the change of impedance in the case of 5ppm and 50ppm mixed solution, similar methods illustrated in section 3.1.1 are used to conduct data analysis, including the selection of characteristic points and the calculation of impedance change compared to DI water at log(freq.)=2.5.

Figure 3.13 and 3.14 shows the characteristic points on Bode impedance plot for the case of 5ppm and 50 ppm mixed solution, respectively. The standard deviation was calculated with 3 collected data in the repetitive experiments. From the result, it can be seen that the points for mixed solution lie between the points for single HMI solution. As the portion of $ZnSO_4$ $_{(aq)}$ in the mixed solution increases, the impedance value moves toward the value for pure $ZnSO_4$ $_{(aq)}$. However, something interesting is that the situations in 5ppm and 50ppm cases are different. In the case of 5ppm mixed solution, the points for 25%, 50% and 75% $ZnSO_4$ $_{(aq)}$ lie closer to the point for pure $Pb(NO_3)_2$ $_{(aq)}$ rather than the point for pure $ZnSO_4$ $_{(aq)}$. On contrast, in the case of 50ppm mixed solution, the points for mixed solution lie closer to pure $ZnSO_4$ $_{(aq)}$. It seems that $Pb(NO_3)_2$ $_{(aq)}$ has a ”dominant role” at low concentration, affecting the impedance value of the mixed solution more than $ZnSO_4$ $_{(aq)}$, while at high concentration, $ZnSO_4$ $_{(aq)}$ has its dominant influence.

In addition, the alignment of points on the linear trend line for a mixed solution is not as consistent as the one observed in section 3.1.1, where most of the points align consistently on the linear trend line when varying concentration in a single HMI solution. In the case of the 5ppm HMI solution, the local maximum points

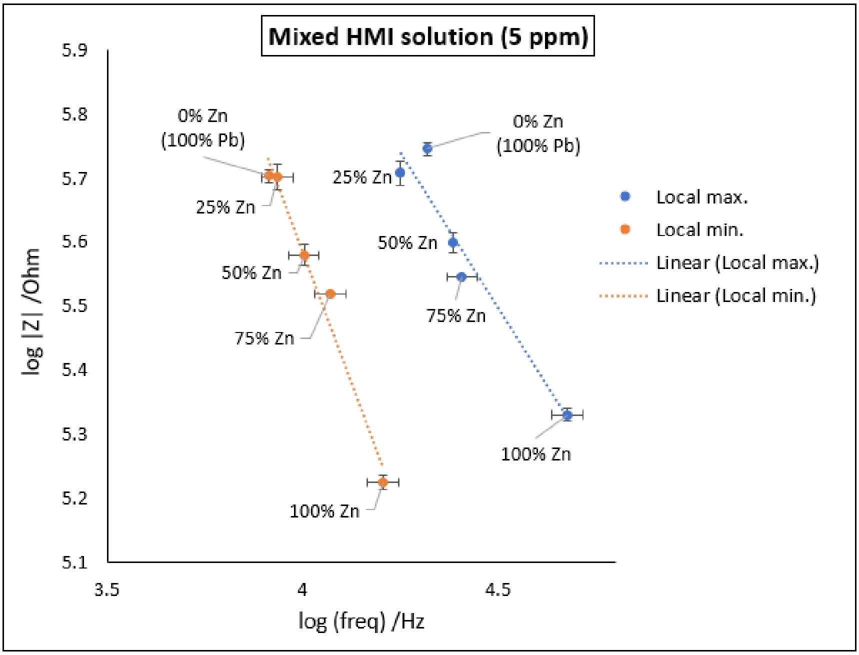

Figure 3.13: Characteristic points on the Bode impedance plot for 5ppm mixed HMI solution, representing the fluctuation of impedance in the high-frequency region.

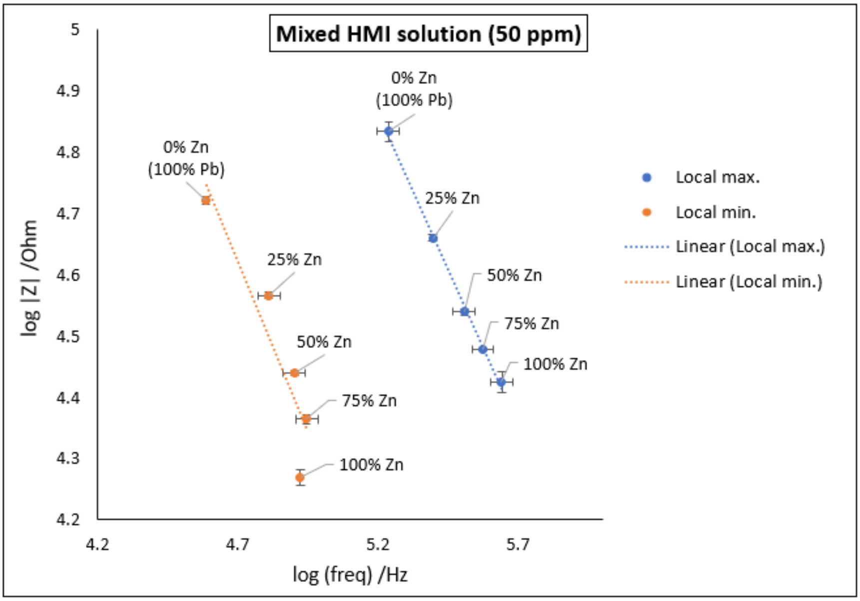

Figure 3.14: Characteristic points on the Bode impedance plot for 50ppm mixed HMI solution, representing the fluctuation of impedance in the high-frequency region.

for mixed solution deviated from the linear trend line and moved toward the right side, indicating that the local maximum points for mixed solution appear at a lower frequency compared to single HMI solution. In the case of 50ppm, this shift of characteristic points was observed in the local minimum, where the points move toward higher frequency.

In order to quantify the change of overall impedance for the mixed HMI solution, figure 3.15 was made. From the result, it can be seen that the impedance change compared to DI water in log scale at 317Hz does not behave as an arithmetic progression as the mixing ratio increases. Although the impedance value in the log scale does increase or decrease according to the change in mixing ratio, no simple pattern such as the arithmetic sequence can be found in the percentage change of impedance.

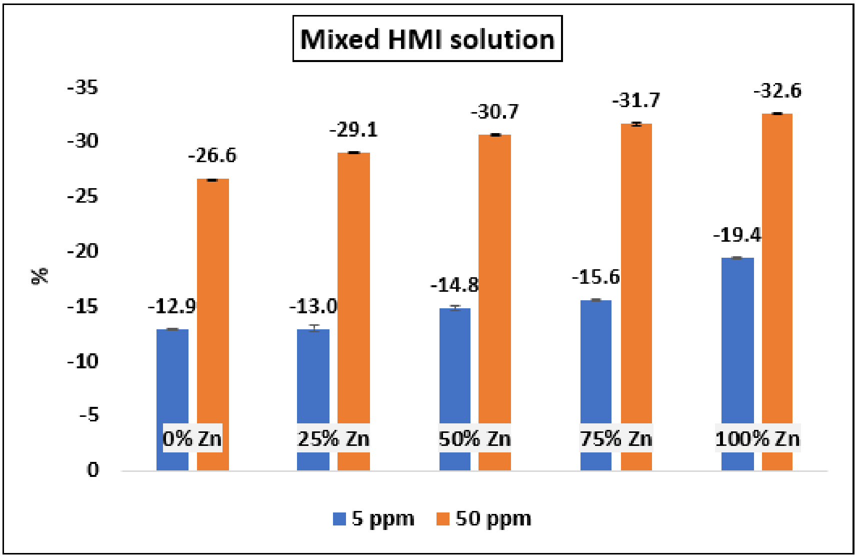

Figure 3.15: Impedance change at 317Hz compared to DI water for 5ppm and 50ppm mixed HMI solutions.

(2) Interpretation of Nyquist impedance plot

Figure 3.16 and 3.17 show the Nyquist impedance plot for 5ppm and 50ppm mixed solution, respectively. In the case of a 5ppm mixed solution, the inductive behavior that follows the first semicircle seems to be reduced, creating a shape with two overlapping semicircles without a loop in between. However, in the case of 50ppm mixed solution, the shape of the curve for the mixed solution does not have significant differences from the one for single HMI solution, except the changes in size according to the mixing ratio.

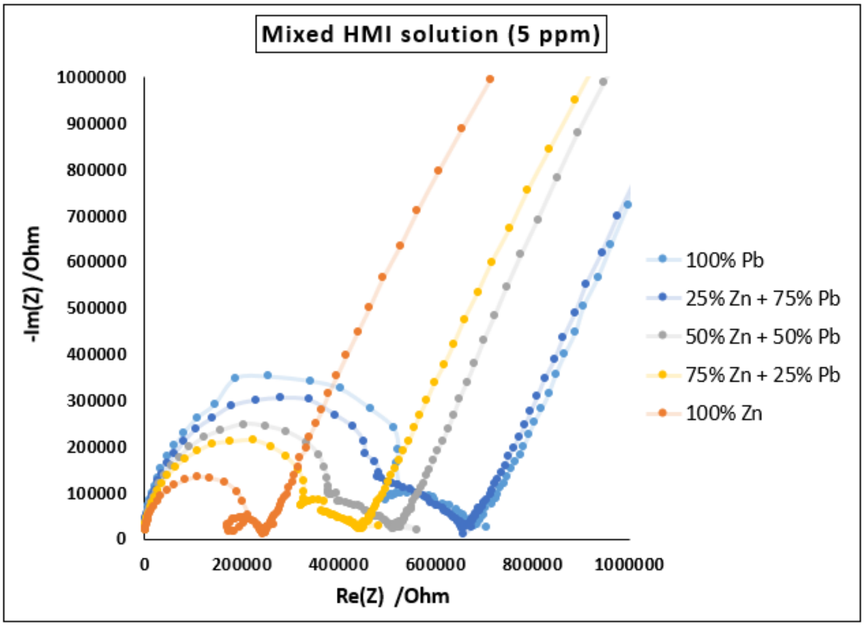

Figure 3.16: Nyquist impedance plot of 5ppm mixed HMI solution at 20°C.

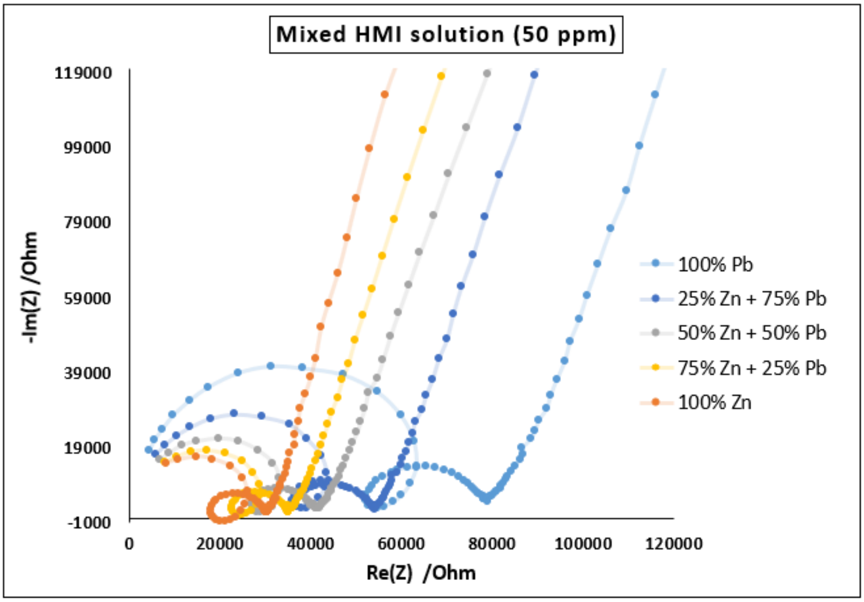

Figure 3.17: Nyquist impedance plot of 50ppm mixed HMI solution at 20°C.

(3) Data analysis on Nyquist impedance plot

The characteristic points on the Nyquist impedance plot for 5ppm and 50ppm mixed solution are shown in figure 3.18 and 3.19, respectively. In the case of 5ppm mixed solution, the extent of charge transfer resistance decreases as the portion of $ZnSO_4$ $_{(aq)}$ increases. However, the characteristic points are not evenly distributed along the linear trend line. For instance, the points for "0% Zn" and "25% Zn" are very close to each other and overlap at the local minimum. In addition, the point for "75% Zn" does not lie in the middle of "50% Zn" and "100% Zn". Instead, its position is closer to "50% Zn".

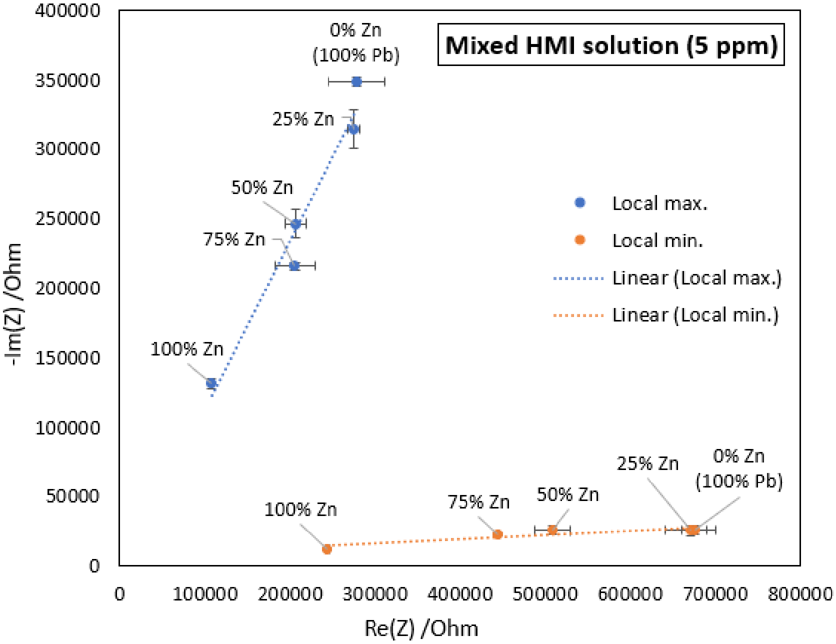

Figure 3.18: Characteristic points on the Nyquist impedance plot for 5ppm mixed HMI solution, representing the extent of charge transfer resistance (local max.) and the extent of non-diffusional resistance (local min.) of the electrochemical system.

For the case of a 50ppm mixed solution, the characteristic points align more orderly. The local maximum points, which represent the extent of charge transfer resistance, not only follow the linear trend lines but also descend with a predictable pattern. When the portion of $ZnSO_4$ $_{(aq)}$ increases 25%, the distance between the local maximum point of the mixed solution and the point of pure $ZnSO_4$ $_{(aq)}$ becomes approximately halved.

The complexity of the system is due to the fact that there are multiple ions present in the water at the same time. Aside from the cations, namely Pb^{2+} and

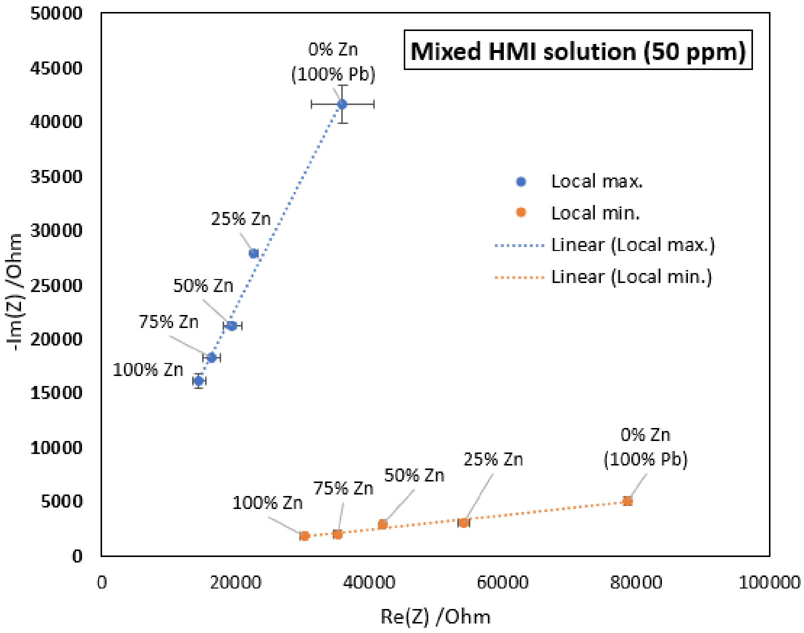

Figure 3.19: Characteristic points on the Nyquist impedance plot for 50ppm mixed HMI solution, representing the extent of charge transfer resistance (local max.) and the extent of non-diffusional resistance (local min.) of the electrochemical system.

Zn^{2+}, there are also two different anions present in the system, including NO_3^- and SO_4^{2-}. It is not clear how these ionic species interact with each other and influence the overall impedance response. However, the reason why the $Pb(NO_3)_2$ $_{(aq)}$ has a dominant role in determining the impedance value in the case of 5ppm mixed solution might be explained by the adsorption process of Pb^{2+} on the electrode surface. In the research done by Ekop and Eddy, the adsorption potential of Pb^{2+}, Ni^+, and Zn^{2+} on the *Helix aspera* shell were investigated, and Pb^{2+} turned out to be the most absorbed species and Zn^{2+} were the least absorbed one. In addition, the adsorption of Zn^{2+} on natural zeolite is reported to be slower than the adsorption of Pb^{2+} [82], as well as in the case of untreated coffee residues [83]. In the case of titanium phosphate, the adsorption of Pb^{2+} is reported to be slower than the adsorption of Zn^{2+}. Still, the overall capacity of Pb^{2+} adsorption is higher than Zn^{2+} after the equilibrium of the system is reached [84]. The reason why Pb^{2+} has a higher affinity to adsorption on various materials than Zn^{2+} is resulted from its lower magnitude of hydration enthalpy, as suggested by Martin-Dupont *et al.*.

In section 3.2, the adsorption of Pb^{2+} and Zn^{2+} are both found in surface analysis of this research. However, since the surface analysis experiments in this research were not specifically arranged for studying adsorption kinetic, the adsorption affinity of the two HMIs cannot be determined. If there is a higher tendency for the adsorption of Pb^{2+} on the platinum electrode, it will support the argument that lead ions have a greater reaction with the electrode surface and thus has a dominant role in determining the charge transfer resistance in the mixed solution at certain concentration. For instance, when the concentration of Pb^{2+} and Zn^{2+} are both low (5ppm), the influence of Pb^{2+} becomes more obvious. In contrast, when the concentrations of both heavy metal ions are high, the influence of Pb^{2+} becomes less obvious due to a significant amount of Zn^{2+} and other ions in the mixed solution, which hinder the reaction between Pb^{2+} and the electrode. It should be noted that this argument is merely a hypothesis, and further research is required to understand if the differences in the adsorption affinity of the two HMIs contribute to the inconsistent impedance response in the low and high concentration cases. In addition, the adsorption kinetic also depends on temperature, the concentration of the solution, and immersion time of the electrode [84]. It is not clear whether the adsorption of Pb^{2+} and Zn^{2+} reach the equilibrium state during the EIS measurements.

Another parameter to be considered here is the pH value. In the studies of adsorption kinetic, the pH value also plays a role in determining the adsorption process of metal ions [83]. However, since the pH value was not fixed during the experiments in this research, it may affect some of the electrochemical reactions, especially when there are multiple ions present inside the solution.

3.1.3. The effect of varying temperature

In this section, the influence of temperature on the EIS result is presented and discussed. Data analysis on the Bode impedance plot and the Nyquist impedance plot are conducted in the same way as in the previous sections. Figure 3.20 shows the Bode impedance plot for all the solution cases that were investigated under the influence of changing temperature, including 5ppm $Pb(NO_3)_2$ $_{(aq)}$, 5ppm $ZnSO_4$ $_{(aq)}$, 50ppm $Pb(NO_3)_2$ $_{(aq)}$, and 50ppm $ZnSO_4$ $_{(aq)}$. From the result, it can be seen that the impedance response in the high and mid-frequency region are affected by temperature in all cases. As the temperature increases, the impedance value in these regions decrease.

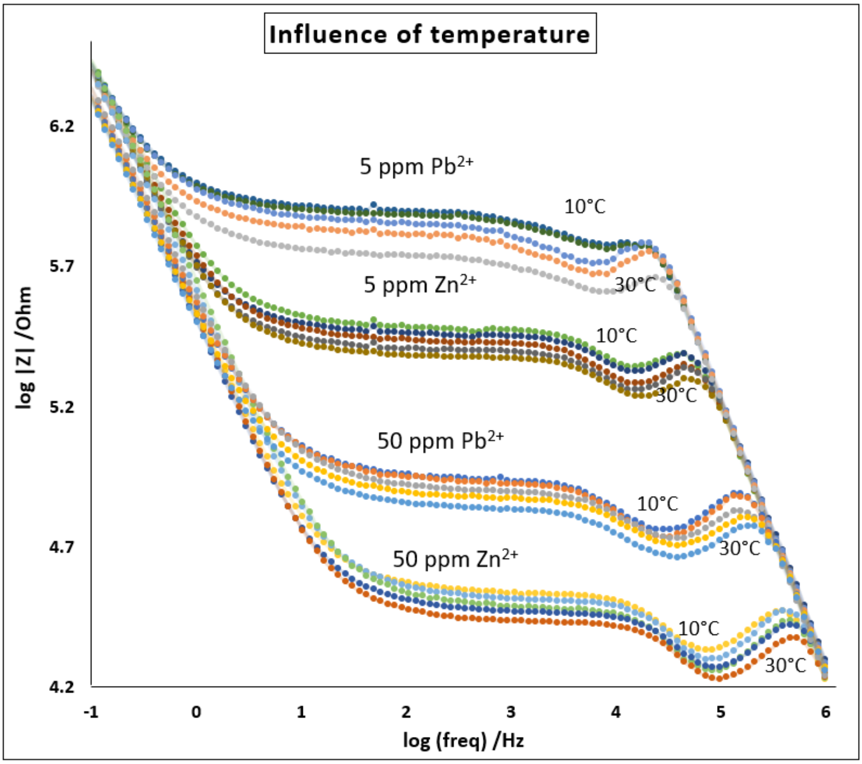

Figure 3.20: The influence of varying temperature on the Bode impedance plot.

(1) Data analysis on Bode impedance plot

The characteristic points on the Bode impedance plot were selected and compared for data analysis. Figure 3.21 shows the average of local maximum point and the local minimum points for the case of 5ppm $ZnSO_4$ $_{(aq)}$ and 5ppm $Pb(NO_3)_2$ $_{(aq)}$. The error bar represented the standard deviation from the average value and was calculated with three collected data. From the figure, it can be seen that the impedance value descends as the temperature increases. However, the error bars for 5ppm

$Pb(NO_3)_2$ (aq) are shown to be bigger than that of 5ppm $ZnSO_4$ (aq). In addition, some of the points for 5ppm $Pb(NO_3)_2$ (aq) deviates a lot from the linear trend line. This may indicate that the system is unstable and certain electrochemical reactions occur in respond to temperature changes in the case of 5ppm $Pb(NO_3)_2$ (aq). However, it can also imply that the EIS sensor is more sensitive when the concentration of the HMI solution is low, and the overall impedance value of the system is high. In other words, getting reproducible data may be originally more difficult in this case and does not necessarily refer to the system's instability.

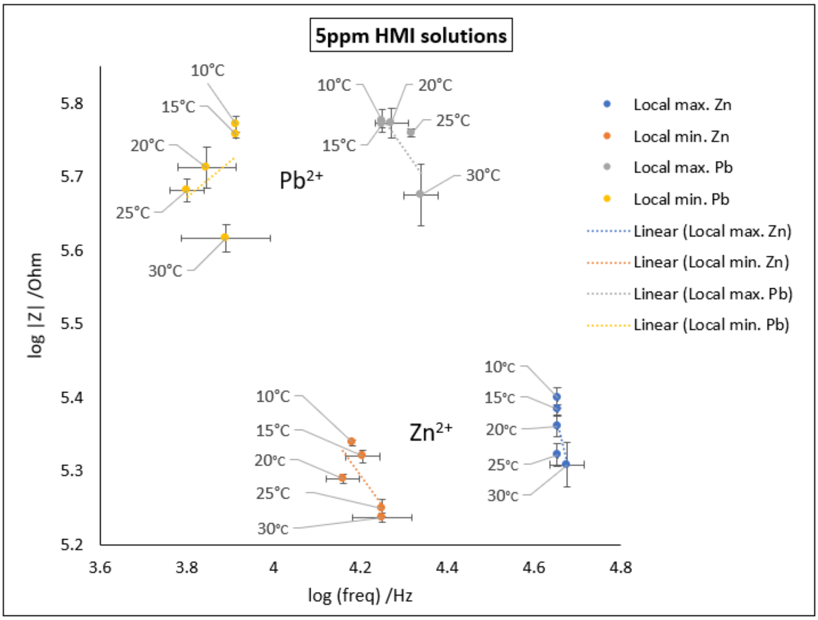

Figure 3.21: Characteristic points on Bode impedance plot for 5ppm $ZnSO_4$ (aq) and $Pb(NO_3)_2$ (aq) at various temperature, representing the fluctuation of impedance in the high-frequency region.

The characteristic points on Bode impedance plot for 50ppm $ZnSO_4$ (aq) and 50ppm $Pb(NO_3)_2$ (aq) at various temperature are shown in figure 3.22. The overall standard deviation of the characteristic points at 50ppm are smaller than that at 5ppm. In addition, the points align orderly on the linear trend line and the impedance values decrease with increasing temperature. It is worth notice that local maximum points of 50ppm $ZnSO_4$ (aq) occurs at almost the same frequency. The "straight" linear trend line in the case of 5ppm $ZnSO_4$ (aq) is an interesting phenomenon because in the all the cases discussed previously, the local maximum point occurs at different frequency when the parameters (e.g. concentration, mixing ratio, temperature) changes.

The impedance change compared to DI water in log scale for the four solution cases is shown in figure 3.23. The result shows that when the temperature

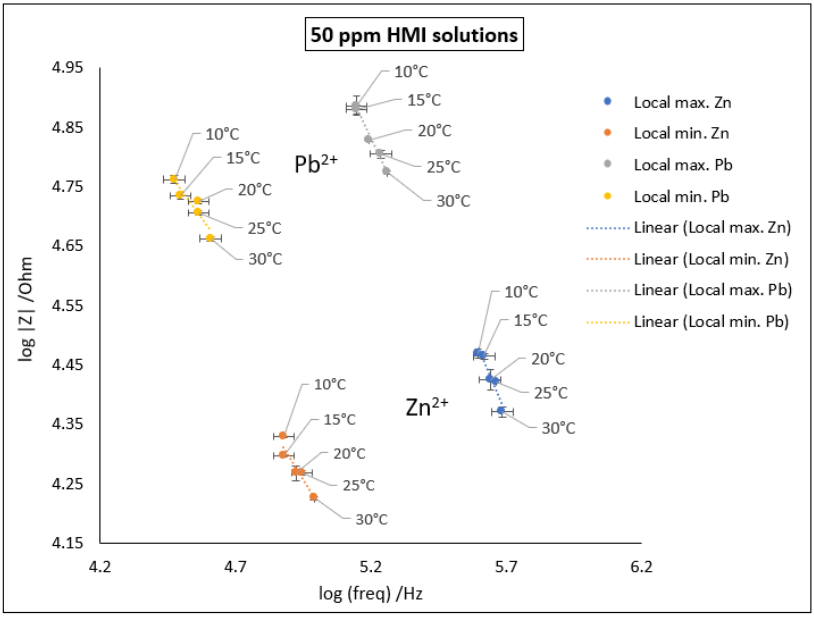

Figure 3.22: Characteristic points on Bode impedance plot for 50ppm $ZnSO_4$ $_{(aq)}$ and $Pb(NO_3)_2$ $_{(aq)}$ at various temperature, representing the fluctuation of impedance in the high-frequency region.

decreases or increases 5°C, the impedance change compared to DI water will generally deviate 0.2-0.6%. However, for the case of 5ppm $Pb(NO_3)_2$ $_{(aq)}$, the deviation between 25°C and 30°C is 1%. This exception may be resulted from the data points collected at 30°C for 5ppm $Pb(NO_3)_2$ $_{(aq)}$, which have the largest standard deviation among all the cases. It is worth notice that the impedance changes shown in figure 3.4 for the doubling of concentration in a HMI solution are 4%±0.3%. If the standard condition of the EIS sensor is set at 20°C, then the impedance change caused by ±10°C deviation is generally less than 1%. Since the change in impedance due to temperature variation has a clear pattern, it is possible to calibrate the temperature influence during the later stage of sensor application.

(2) Interpretation of Nyquist impedance plot

Figure 3.24 shows the Nyquist impedance plots for the four solution cases. The variation of temperature does not significantly affect the shape of curves in the Nyquist impedance plots. However, the size of the first semicircle in all cases changes with temperature, which implies that the temperature has an impact on the value of charge transfer resistance. This result is compatible with some other research related to temperature influence on the EIS measurements in different system. In the research done by Zhang *et al.*, the temperature was found to have significant impacts on the value of charge transfer resistance (R_{ct}) of the lithium-ion battery. As the temperature increases, the value of R_{ct} decreases, and this phenomenon observed in various systems is believed to be related to the mass transfer kinetics of

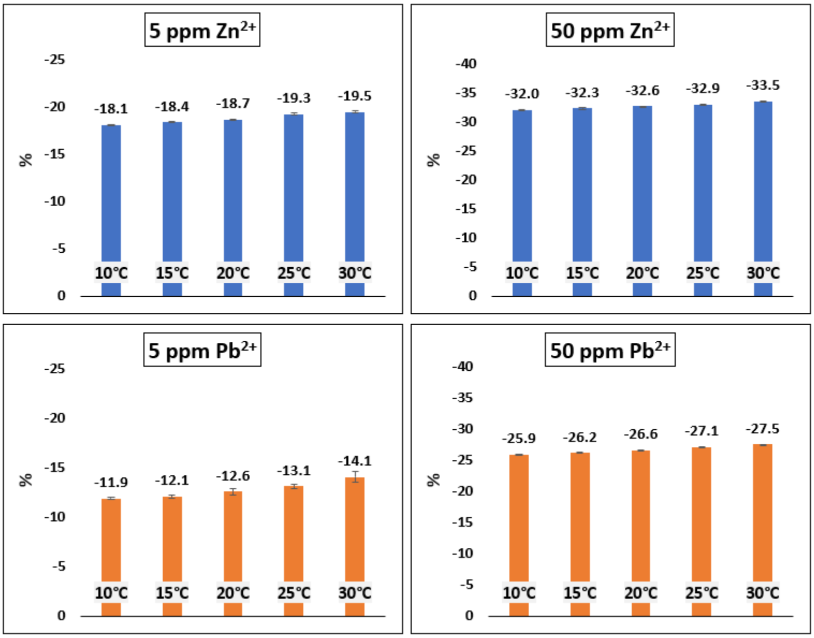

Figure 3.23: Impedance change at 317Hz compared to DI water for 4 cases of HMI solutions at various temperature.

the system, as suggested by various researchers in the field of Li^+ and Na^+ battery [61] [86] [87]. However, it should be noted that the concept of electron transfer and the concept of mass transfer are different. Although the mass transfer kinetics of the ionic species has an impact on the electron transfer process between the electrode surface and the electrolyte, the mass transfer kinetic is better described with Warburg impedance rather than charge transfer resistance. The value of Warburg impedance, as mentioned in equation 3.9 and 3.10, is related to temperature, temperature-dependent diffusivity, and temperature-dependent electroactive surface area.

The calculation of charge-transfer resistance was previously mentioned in section 3.1.1 with equation 3.4 and 3.5. However, these equations are not ideal to describe the temperature-dependence of charge transfer resistance, since the electroactive surface area varies with temperature. The relationship between the charge transfer resistance and temperature can be better described with Arrhenius relation [87] [88], as shown in equation 3.12, where A is the proportionality constant, k_B is Boltzmann constant, T is the temperature, and E_a is the activation energy of the charge transfer process.

$$\frac{1}{R_{ct}} = Ae^{-\frac{E_a}{K_B T}} \tag{3.12}$$

If the value of charge transfer resistance is determined for each temperature by data fitting into the equivalent circuit model, then the activation energy of the charge transfer process can be calculated. Additionally, the activation energy for the diffusion process can also be calculated by the same equation if the diffusion resistance is known. Nevertheless, these calculations are beyond the scope of this project. Further discussion on the value of charge transfer resistance is discussed in section 3.3.

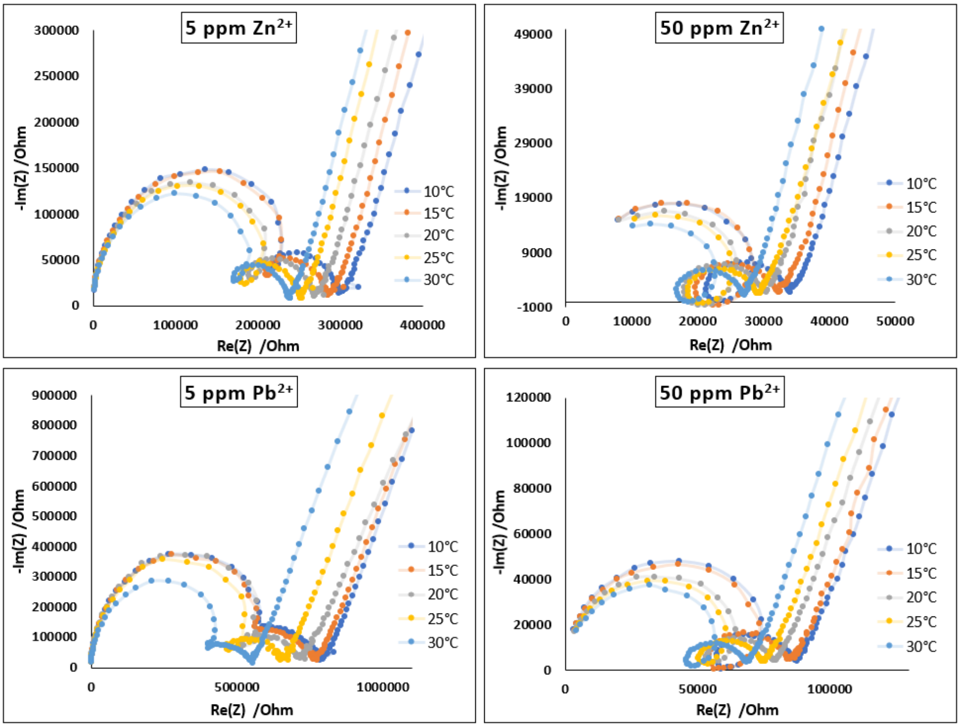

Figure 3.24: Nyquist impedance plot for 4 cases of HMI solutions at various temperature.

(3) Data analysis on Nyquist impedance plot

Figure 3.25 shows the characteristic points on Nyquist impedance plot for 5ppm $ZnSO_{4\ (aq)}$ and 5ppm $Pb(NO_3)_{2\ (aq)}$ at various temperature. The result shows that the extent of charge transfer resistance (local maximum points) for 5ppm $ZnSO_{4\ (aq)}$ decrease when the temperature increases. In contrast, in the case of 5ppm $Pb(NO_3)_{2\ (aq)}$, the local maximum points for 10°C - 25°C almost overlap with each other and only the point of 30°C has a significant decrease. In addition, the standard deviation for the case of 5ppm $Pb(NO_3)_{2\ (aq)}$ is much larger than that for 5ppm $ZnSO_{4\ (aq)}$.

It should be noted that the local minimum point represents the extent of overall non-diffusional resistance, including the ohmic resistance, charge transfer resistance, and the resistance in the region of inductive behavior. In all the cases discussed previously, the position of local minimum points is arranged in similar pattern as the local maximum points along the linear trend line, which means that the change of non-diffusional resistance is mainly determined by the change of charge transfer resistance. However, in the case of 5ppm $Pb(NO_3)_2$ $_{(aq)}$, there are deviations contributed from the other parts, such as the resistance in the inductive behavior region. Therefore, the local maximum points and local minimum points are not arranged similarly.

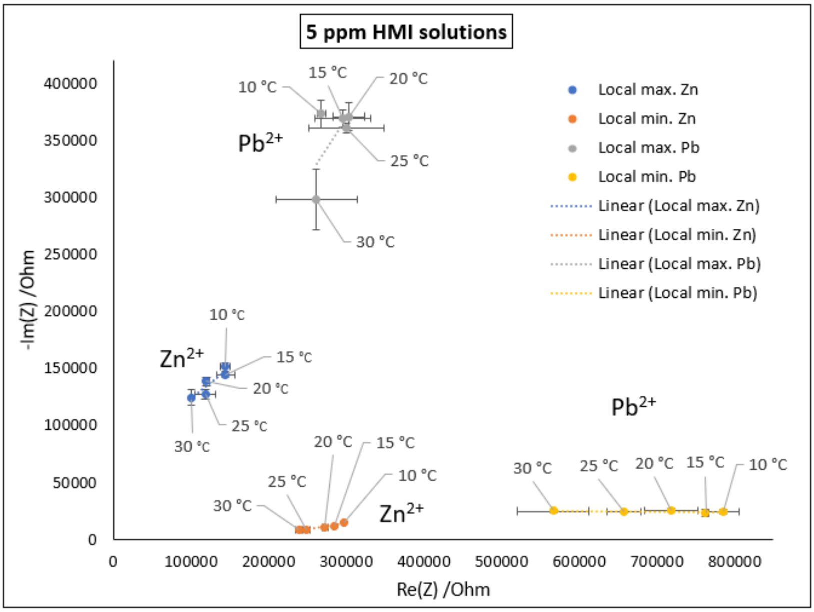

Figure 3.25: Characteristic points on the Nyquist impedance plot for 5ppm $ZnSO_4$ $_{(aq)}$ and $Pb(NO_3)_2$ $_{(aq)}$ at various temperature, representing the extent of charge transfer resistance (local max.) and the extent of non-diffusional resistance (local min.) of the electrochemical system.

Figure 3.26 shows the characteristic points on Nyquist impedance plot in the case of 50ppm $ZnSO_4$ $_{(aq)}$ and 50ppm $Pb(NO_3)_2$ $_{(aq)}$ at various temperature. The standard deviation of the points for 50 ppm $Pb(NO_3)_2$ $_{(aq)}$ is higher than that for 50 ppm $ZnSO_4$ $_{(aq)}$. In addition, in the case of 50 ppm $Pb(NO_3)_2$ $_{(aq)}$, the positions of local maximum points are arranged in different pattern than that of local minimum points.

In both 5ppm and 50ppm conditions, the electrochemical mechanism in response to temperature changes is shown to be slightly different for the two HMI solutions. In the case of $ZnSO_4$ $_{(aq)}$, the extent of non-diffusional resistance is mainly controlled by the extent of charge transfer resistance. As the temperature increases, both the charge transfer resistance and the non-diffusional resistance decreases. However, in the case of $Pb(NO_3)_2$ $_{(aq)}$, the change of non-diffusional resistance does not fully comply with the change of charge transfer resistance, as the alignment of local maximum and minimum points on the Nyquist impedance plot do not behave in the same manner. This means that the temperature may also influence the resistance in the inductive region for the case of $Pb(NO_3)_2$ $_{(aq)}$.

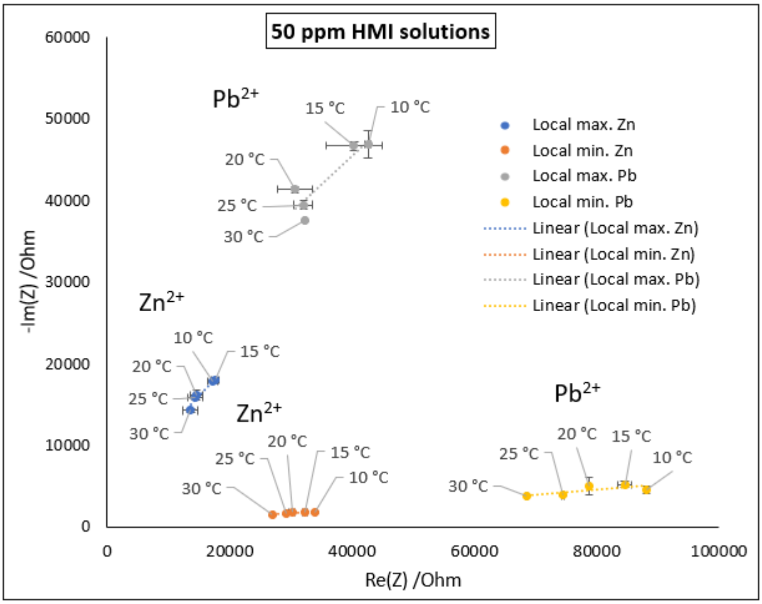

Figure 3.26: Characteristic points on the Nyquist impedance plot for 50ppm $ZnSO_4$ $_{(aq)}$ and $Pb(NO_3)_2$ $_{(aq)}$ at various temperature, representing the extent of charge transfer resistance (local max.) and the extent of non-diffusional resistance (local min.) of the electrochemical system.

3.1.4. The effect of the electrochemical cell designs

In this section, the impedance response of various electrochemical cell designs is compared and discussed. One of the goals is to investigate the possible contribution to the inductive behavior from artifacts in the cell design, such as wiring and the presence of the reference electrode. Figure 3.27 shows the Bode impedance plot for the standard electrochemical cell design and its soldering modification. There is no significant difference between the impedance response of the two designs, except at the very-low-frequency region, where the soldering modification has a slight increase of impedance near 0.1 Hz for the case of DI water. The impedance response in this region is related to the diffusion process and was observed to be influenced by the selection of individual SCE during the experiments.

Figure 3.28 shows the Bode impedance plot for the standard design, the design with Pt wire as RE, and the designs made for surface analysis. The figure indicates

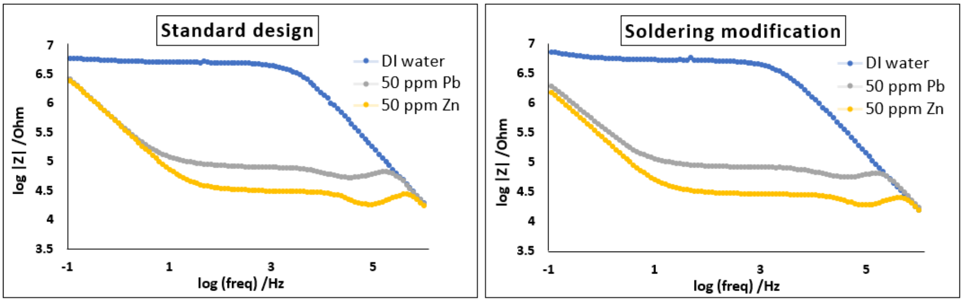

Figure 3.27: Comparison of Bode impedance plot between the standard electrochemical cell design and the soldering modification.

that the impedance response becomes very different when changing the WE from Pt wire to Pt foil. In addition, when the exposed surface area changes from a circle with 1 mm diameter to 1 cm ×1 cm square, the overall impedance value decreases significantly. Another thing to notice is that for the design of ”Pt foil as WE with a small area,” two plateau regions appear in the Bode impedance plot. The additional plateau region might due to the coverage of green tape on the Pt foil during EIS measurements, as green tape can act as a coating on the platinum surface.

As for the design of ”Pt wire as RE,” the impedance response is similar to the standard design. However, at high frequency, the fluctuation of impedance becomes more severe when replacing the SCE with Pt wire. In addition, after changing the SCE to Pt wire, the fluctuation of impedance occurs in both cases of HMI solution and DI water.

(1) Data analysis on Bode impedance plot

In order to compare the sensitivity of different cell designs, the impedance changes in log scale compared to DI water at 317HZ for various cell designs are shown in figure 3.29. The result shows that the impedance changes of the standard design, soldering modification, and the design with Pt wire as RE are similar. For these three designs, the impedance changes for the case of 50ppm $ZnSO_4\ _{(aq)}$ and 50ppm $Pb(NO_3)_2\ _{(aq)}$ are 32.35%±0.85% and 26.15%±0.65%, respectively.

For the design of ”Pt foil as WE with a small area,” the impedance changes are less than the standard design, indicating lower sensitivity in response to the presence of HMIs. However, the decrease of impedance changes of this design is partly because the plateau region of DI water and HMI solutions do not align well at 371Hz, as shown in figure 3.28. As for the design of ”Pt foil as WE with a large area,” the impedance changes are the highest among all the cell designs, indicating the highest sensitivity in response to the presence of HMIs. It should be noted that the sensitivity mentioned in this section refers to the degree of impedance change compared to DI water when there are HMIs present in the solution. Higher sensitivity indicates a larger extent of impedance change. However, for the design of ”Pt

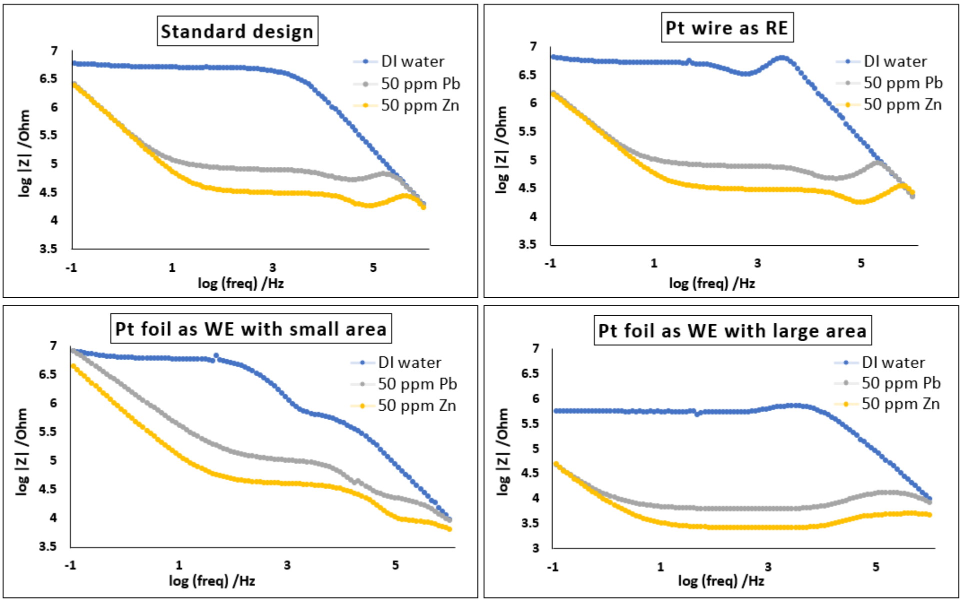

Figure 3.28: Comparison of Bode impedance plot between the standard electrochemical cell design and the designs for surface analysis & evaluation of sensor prototype.

foil as WE with a large area," the detection of HMI concentration can become more limited than the other designs when the overall impedance value of the solution is low (the concentration of ions are high inside the solution), since it is more difficult to distinguish the characteristic points for a specific HMI solution when the overall impedance of the system is high.

The difference of impedance changes between the case of 50ppm $ZnSO_4$ $_{(aq)}$ and 50ppm $Pb(NO_3)_2$ $_{(aq)}$ for various designs turned out to be 6.3%±0.3%, with the highest value (6.6%) appears in the design of "Pt foil as WE with large area". The result indicates that the design with a large exposed surface area distinguishes the two HMIs slightly better than other designs at the same concentration. However, the classification of the two HMIs can not merely depend on the data analysis on the overall impedance value. The development of equivalent circuit models and data fitting techniques is required to classify different types of HMIs further.

(2) Interpretation of Nyquist impedance plot

This section focuses on the examination of the inductive behavior presented in various electrochemical cell designs. Figure 3.30 shows the Nyquist impedance plots for the standard design and its soldering modification. The size of the inductive loop slightly decreases in the case of soldering modification, implying that the presence of copper wire in the standard design may partly contribute to the inductive behavior in the EIS result. However, the inductive behavior still presents in the

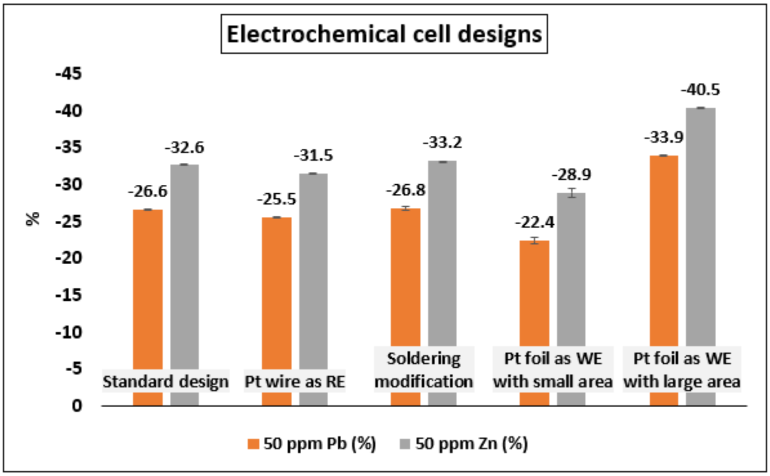

Figure 3.29: Impedance change in log scale compared to DI water at 317Hz for various electrochemical cell designs.

design of soldering modification, indicating possible contribution from the adsorption/desorption process of the ionic species inside the solution.

As mentioned previously, the difference of the Warburg element between the standard design and the soldering modification is observed to be influenced by selecting individual SCE during the experiment. Since further analysis in the very-low-frequency region is beyond the scope of this project, more detailed interpretation cannot be made to explain the parameters that influence the Warburg element.

Figure 3.31 shows the Nyquist impedance plot for the design of ”Pt wire as RE.” After replacing the SCE with Pt wire, the inductive loop is present in cases of HMI solutions and the case of DI water. In addition, the size of the inductive loop becomes larger compared to that in the standard design, and some of the data points appear in the first quadrant of the Nyquist impedance plot. The result indicates that replacing the SCE with Pt wire increases the inductive behavior in the impedance response. Since the inductive behavior also occurs in the case of DI water, the primary cause of the inductive behavior likely comes from the construction of the electrochemical cell, such as the stray capacitance between the WE and the RE.

For the designs made for surface analysis, the inductive behavior was found in the case of ”Pt foil as WE with a large area.” Instead of a ”spiral” shape of the inductive loop as seen in the case of standard design and the design of ”Pt wire as RE,” which has the second semicircle formed in the fourth quadrant of the Nyquist impedance plot, the inductive loop shown in figure 3.32 does not form the second semicircle in the fourth quadrant. As for the design of ”Pt foil as WE with a small area,” no inductive loop is shown in the Nyquist impedance plot. For these two

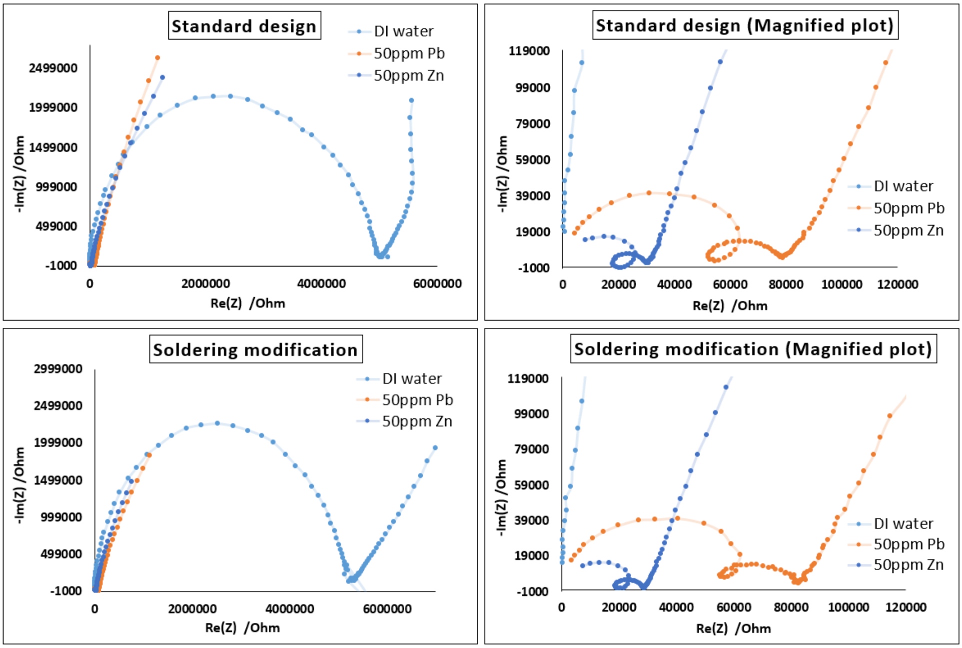

Figure 3.30: Nyquist impedance plot for the standard electrochemical cell design and the soldering modification.

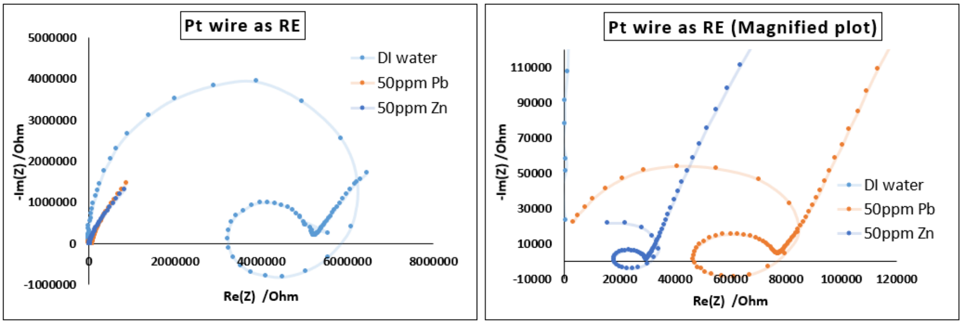

Figure 3.31: Nyquist impedance plot for the design of Pt wire as RE.

designs, the curves in the Nyquist impedance plot have a similar shape in the case of DI water and HMI solutions, indicating that the cell's configuration is the main contribution to the non-standard behaviors.

It is worth notice that there are two consecutive depressed semicircles present in the case of ”Pt foil as WE with a small area.” The first semicircle in the very-high-frequency region may have resulted from green tape coverage on the electrode surface. Since the green tape can act as a coating, the first semicircle can represent the impedance of the coating layer, while the second semicircle represents the charge transfer resistance and double-layer capacitance in a non-ideal situation. In addition, the size of the second depressed semicircle in the case of ”Pt foil as WE with a small area” was found to be similar to the first semicircle found in the case of standard design, which supports the hypothesis mentioned above. However, the phenomenon of two consecutive semicircles may also be related to the influence of stray capacitance [76].

As mentioned previously, the overall impedance value for the case of ”Pt foil as WE with large area” is lower than that of the other designs. As seen in figure 3.32, the size of the first semicircle in the very-high-frequency region, representing the charge transfer resistance, is smaller than that of the other designs. The decrease of charge transfer resistance is directly related to the increase of the WE's exposed surface area. When the temperature and concentration of ions are fixed, increasing WE's surface area also increases the electroactive surface area and therefore decreases the charge transfer resistance according to equation 3.4 and 3.5.

In conclusion, the inductive behavior in the standard design cannot be fully attributed to the connection of the copper wire since the inductive loop was also found in the case of soldering modification. Considering the fact that no inductive loop was found in the case of DI water, it is likely that the adsorption/desorption process of ionic species plays a role in the inductive region of the standard design. In contrast, the inductive or non-standard behaviors found in the other designs are primarily attributed to the construction of the cell designs since these behaviors are observed in both cases of DI water and HMI solutions. In other words, it is unlikely that the adsorption/desorption process of the ionic species is the main contributor to the inductive behavior found in these designs. In addition, the design with Pt wire as the RE has an intensified degree of inductive behavior, which is likely related to the stray capacitance between the WE and the RE. This behavior poses a challenge to the development of the EIS sensor as a form of a chip, which uses the same materials to fabricate the three electrodes. Although the design with Pt wire as the RE also produces reproducible data with a small standard deviation, as shown in figure 3.29, the inductive behavior due to design artifacts may affect the extraction of valuable data in the later stage of the application.

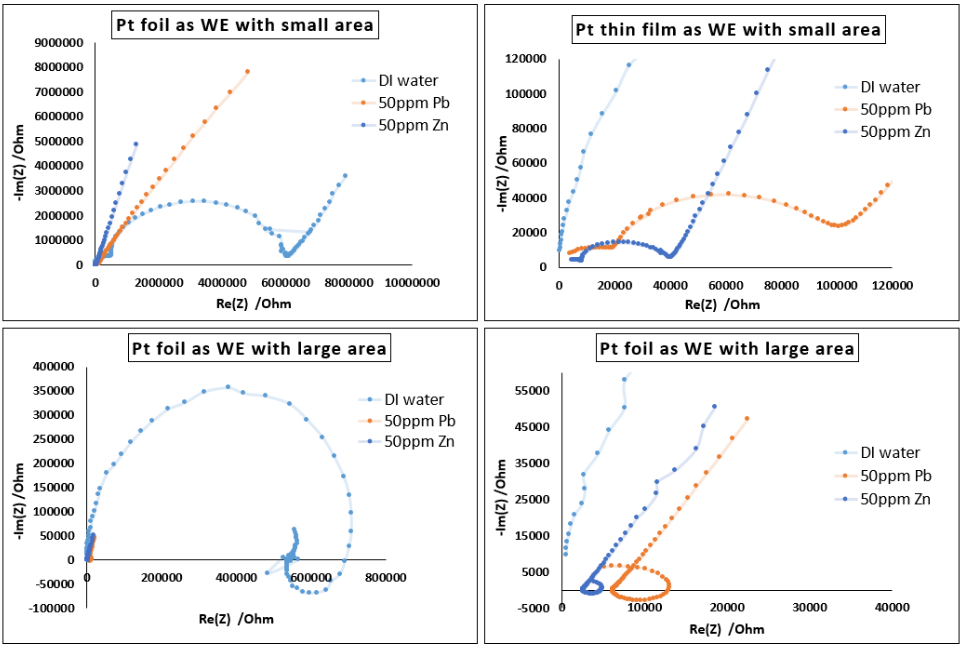

Figure 3.32: Nyquist impedance plot for the designs made for surface analysis.

3.1.5. Detection of HMIs in real water samples

In this section, the practicality of the EIS sensor is examined with real water samples. Figure 3.33 shows the Bode impedance plot for the samples of tap water and industrial water. It should be noted that the addition of Zn^{2+} into the real water samples was conducted by adding 10% of 2000ppm $ZnSO_{4(aq)}$ into the solution. It can be seen from the result that the overall impedance value of tap water and industrial water is much lower than that of DI water. The lowest impedance was detected previously in the case of 100ppm $ZnSO_{4(aq)}$, as shown in section 3.1.1; however, the impedance value of tap water and industrial water is even lower than that of 100ppm $ZnSO_{4(aq)}$, indicating that there were already a lot of ions existing inside the solution. The impedance value has resulted from the combined influence of these unknown ions.

As for the detection of HMIs, adding 10% of 2000ppm $ZnSO_{4(aq)}$ into the tap water lowers the impedance value in the mid- and high-frequency range. However, in the case of industrial water, the change of impedance is not so obvious, as the background solution is rather ”noisy”.

Figure 3.34 shows the impedance response for the cases related to industrial water samples. It can be seen from the result that impedance values of 100% industrial water and that of 90% industrial water added with 10% 2000ppm $ZnSO_{4(aq)}$ are similar. It is not easy to distinguish the two samples. However, for the sample

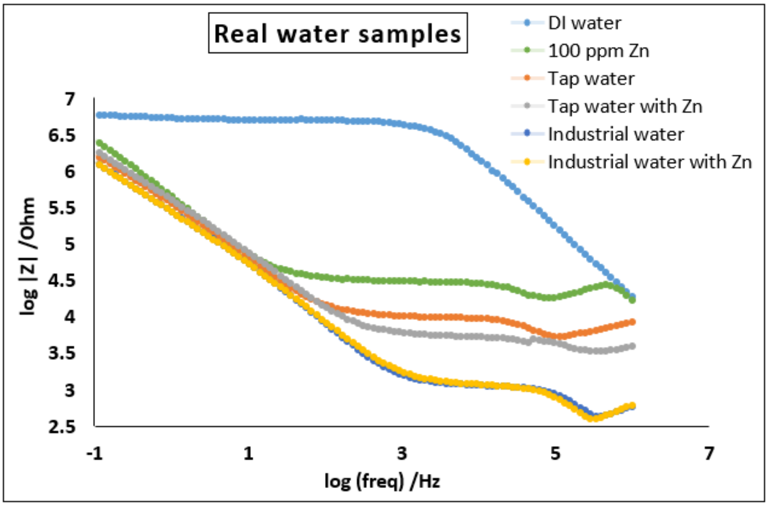

Figure 3.33: Bode impedance plot of real water samples.

of 80% industrial water added with 20% 50ppm $ZnSO_{4(aq)}$, the impedance value in mid- and high-frequency region is slightly higher. The reason why adding 20% 50ppm $ZnSO_{4(aq)}$ into the industrial water increases the overall impedance value is because that 50ppm $ZnSO_{4(aq)}$ was prepared with dissolving the salt in DI water, and the impedance value of 50ppm $ZnSO_{4(aq)}$ is much higher than that of industrial water. In other words, adding the 50ppm $ZnSO_{4(aq)}$ makes the solution become "cleaner" (the overall concentration of the ions decreases). The result shows that the ionic concentration is clearly reflected in impedance values.

(1) Interpretation of Nyquist impedance plot

The magnified Nyquist impedance plot for the real water sample, as shown in figure 3.35, indicates that there is also an inductive behavior in the case of tap water and industrial water, which is likely related to the adsorption/desorption process of the existing ions and their compounds. Since the data points started in the inductive region, the size of the first semicircle, representing the extent of charge transfer resistance, cannot be fully identified in these cases.

Figure 3.36 shows the magnified Nyquist impedance plot for the industrial water samples. The sample of 80% industrial water added with 20% 50ppm $ZnSO_{4(aq)}$ has a larger extent of non-diffusional resistance compared to the other two samples. The extent of non-diffusional resistance is marked out by the local minimum point at the beginning of the Warburg element. The increase of non-diffusional resistance comes from the decrease in overall ions concentration, as mentioned previously.

(2) Data analysis on Nyquist impedance plot

In order to know the reproducibility of the EIS result of real water samples, one of the characteristic points (local minimum) on the Nyquist impedance plot is replot-

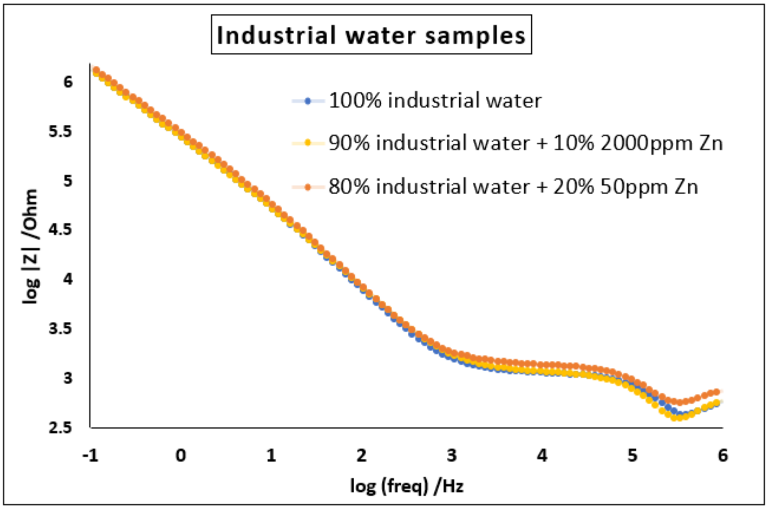

Figure 3.34: Bode impedance plot of industrial water samples.

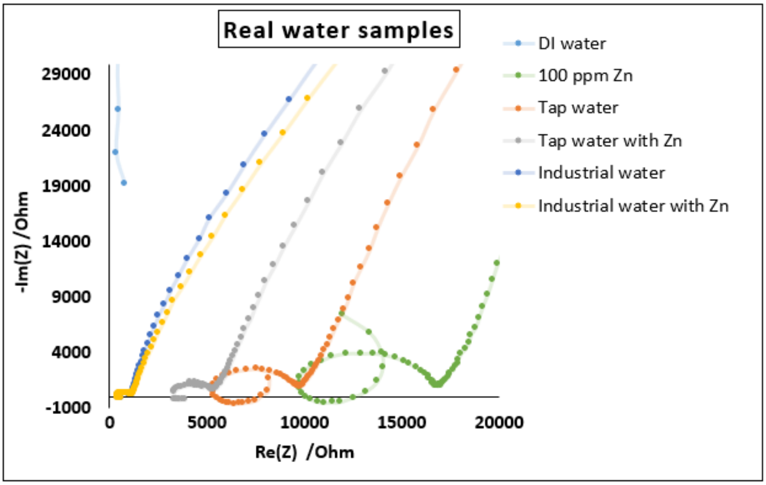

Figure 3.35: Magnified Nyquist impedance plot of real water samples.

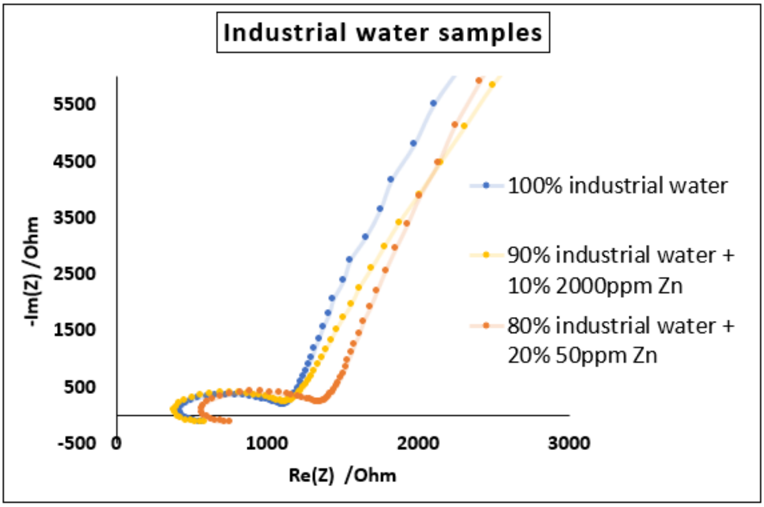

Figure 3.36: Magnified Nyquist impedance plot of industrial water samples.

ted, as shown in figure 3.37 for various real water samples. The result indicates that tap water samples have the largest standard deviation among all the samples, indicating the instability of the system. In contrast, for the industrial water samples and the sample of 100ppm $ZnSO_{4(aq)}$, the EIS results are rather reproducible. It is worth notice that the characteristic points for real water samples do not align nicely on the linear trend line. This alignment might imply that the systems of these water samples are different and cannot be plotted on the same linear trend line, considering that fact that the background water and the ionic composition are different.

In conclusion, the overall impedance value of tap water and industrial water is much lower compared to DI water. In addition, the detection range for these real water samples is way beyond the one in the previous research (section 3.1.1). The change in the impedance value is still detectable in most cases. However, since there is an influence of the background medium of $ZnSO_{4(aq)}$, the impedance value can be increased by adding $ZnSO_{4(aq)}$ with low concentration. Considering the influence of the background medium, a better approach is required to add HMI into the real water during experiments.

In order to expand the detection range in the low impedance environment, one can decrease the surface area of the working electrode. In this way, the system's initial impedance can be increased, which helps improve the sensor's sensitivity when the concentration of ions in the background solution is already very high. The current diameter of the WE is 1mm, which is non-ideal for detecting HMI in the real water environment. In chapter 5.2, the EIS sensor prototype design is proposed in the form of chips, and the electrode dimension is therefore calculated in the unit of μm.

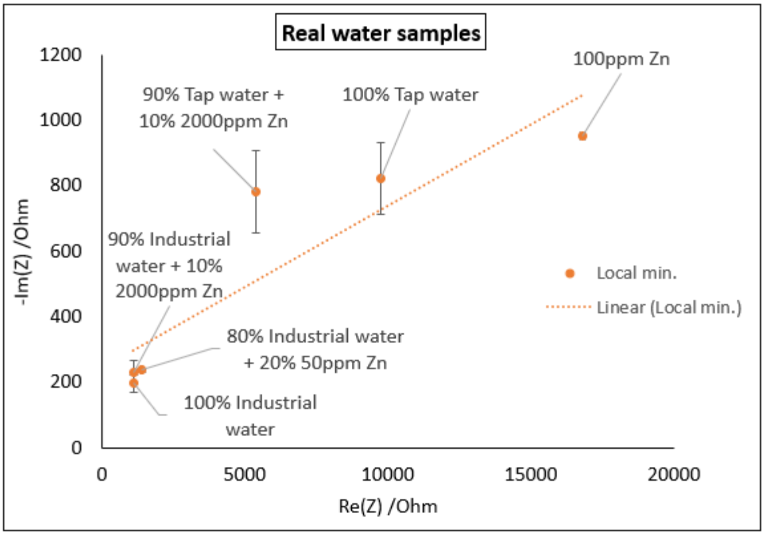

Figure 3.37: Characteristic points on Nyquist impedance plot for real water samples, representing the extent of non-diffusional resistance (local min.) of the electrochemical system.

3.2. Surface analysis

In this section, the result of the surface analysis is presented and discussed. The primary goal of the surface analysis is to investigate whether the HMI-related adsorption/desorption process occurs on the surface of electrodes during the EIS measurement. The presence of HMI-related adsorbates can support the hypothesis that the inductive behavior in the impedance response is partly due to the adsorption/desorption process. It is worth noting that the Pt wire WE in the standard design was replaced with Pt thin foil for the surface analysis due to sample size requirement.

3.2.1. SEM/EDS analysis

The surface of the Pt foil was first examined with SEM/EDS before the EIS measurements. The SEM images for the bare Pt foil before and after hand-polishing are shown in figure 3.38. Before hand-polishing, the surface of Pt foil had visible traces of cold-rolling left from the production stage, as shown as the straight vertical lines on the surface. After hand-polishing with fine diamond particles with $3\mu m$ and $1\mu m$ diameter, the traces of cold-rolling became less evident, and the surface became smoother with fine scratches left from hand-polishing. The difference between the original Pt foil provided by the supplier and the reused sample does not affect the result of SEM/EDS analysis, since the analysis depth of characteristic X-ray is $1\mu m$. However, since XPS is more surface sensitive and only detected the region, which is 3 to 5 nm beneath the surface, the surface's roughness can increase the noise during measurement. Further details are explained in section 3.2.2.

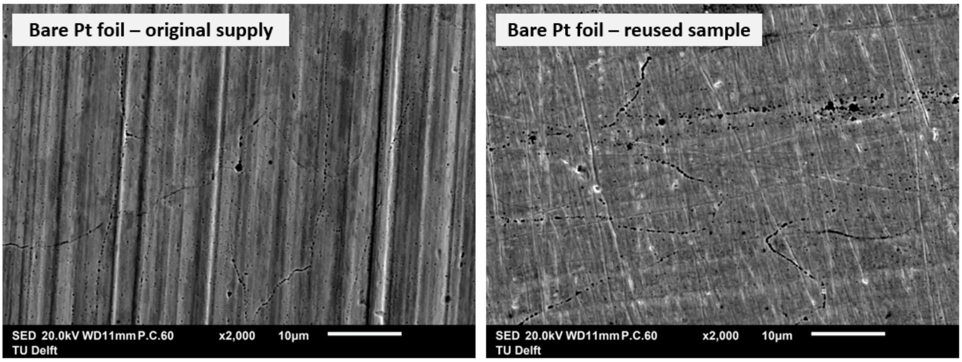

Figure 3.38: SEM images of bare Pt foil before and after hand-polishing.

Figure 3.39 and 3.40 shows the SEM/EDS result for the two samples of bare Pt foil. The percentage (%) listed in the table represents the mass percentage of the element detected by EDS. As expected, only the signal of Pt and C was detected on the grey area of the sample, as shown in point 3 and 5 on figure 3.40. Carbon is a common contamination in the EDS analysis since it appears everywhere in the surrounding. The source of carbon particles may also come from the hand-polishing process and carbon tape usage during the SEM/EDS analysis. However, since the bare Pt foil samples were fully cleaned with isopropanol and ultrasonic bath before the surface analysis, the chances of having fine diamond particles on the surface from the hand-polishing stage are very low.

In addition to the fine scratches and the grey area, there are also lines that consist of numerous black dots present on the bare Pt foil, with or without hand-polishing. The lines represent the grain boundaries of the material, and the black dots that are not in the area of grain boundaries are the defects or inclusions of the material. At these black dots, not only the signals of Pt and C were detected, but also the signals of O, Si, Fe, Mg, Al, Ca, Ni, and Cr. Most of these elements are the impurities already listed by the supplier of the Pt foil, as mentioned in section 2.1.3, including Fe (4ppm), Mg (1ppm), Ca (2ppm), Al (1ppm), and Ni (1ppm). It is worth noting that for some of these elements, the weight percentage is less than 0.5%, indicating a trace amount of impurities.

The reason why the grain boundaries are visible in the SEM images without undergoing any etching process may be due to the localized corrosion on the points with impurities segregation. Platinum is a noble metal that does not undergo any oxidation process in the air at room temperature. However, since there are impurities segregating at the grain boundaries, it is possible that these elements oxidized during the storage stage and formed discontinuous black dots on the grain boundaries. The black color indicates that the depth of these regions is deeper than the other parts of the surface.

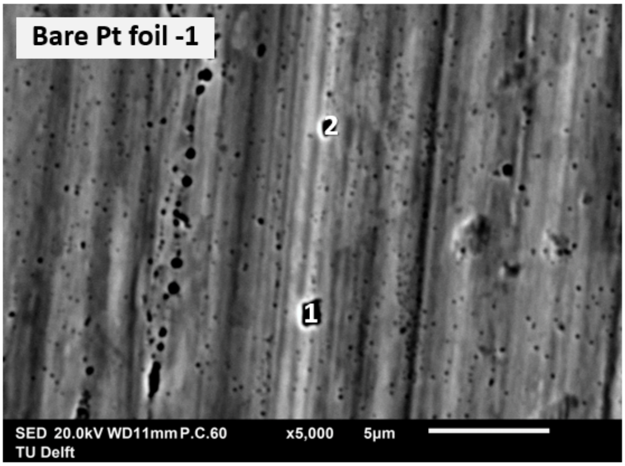

	Pt %	C %	O %	Si %	Fe %	Mg %	Al %	Ca %
No. 1	71.10	2.37	19.23	3.41	-	0.27	2.11	1.51
No. 2	85.08	1.96	8.52	1.51	1.03	-	0.90	0.99

Figure 3.39: SEM image of bare Pt foil (first sample) and point EDS analysis on the surface.

After the Pt foil was immersed into 50ppm $Pb(NO_3)_2$ $_{(aq)}$ and 3 repetitive EIS measurements were conducted, white particles were formed on the surface of Pt foil, as shown in figure 3.41 - 3.44. The size of these white particles ranges from approximately 1 to 3μm in diameter. Some of these white particles show the signal of Pb in EDS analysis, with the mass percentage being higher than 10%. In addition, the signal of Pb was only detected in the regions of white particles, indicating that the adsorption of lead did not occur uniformly on the surface of the electrode. The phenomenon was observed for both cases of the small and large exposed area.

It is not clear what kinds of lead-containing compounds were formed during the EIS measurement. However, according to the EDS analysis, as shown in figure 3.44, the lead-containing adsorbate was likely created in the form of oxide since the signal of oxygen was detected as well when the signal of lead was present.

In figure 3.42, the white particles also contain the signal of impurities that were mentioned previously in the case of bare Pt foil. This phenomenon is due to the fact that the white particle was formed directly on the region of grain boundary and the analysis depth of characteristic X-ray is $1\mu m$. Therefore, the elemental signals beneath the white particle were detected as well. It is not clear if the impurities at grain boundaries interact with the lead ions during the process of adsorption. Nevertheless, the white particles appeared to be randomly distributed on the surface of the Pt electrode. For instance, the white particles in figure 3.43 and 3.44 did not form on the regions of grain boundaries.

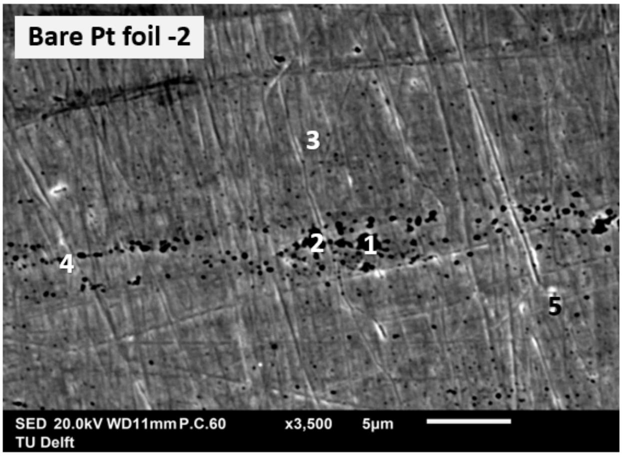

	Pt %	C %	O %	Si %	Fe %	Ni %	Cr %
No. 1	37.02	0.66	-	0.46	14.04	1.00	0.34
No. 2	50.70	-	10.86	0.41	11.00	-	-
No. 3	66.61	1.23	-	-	-	-	-
No. 4	70.16	1.46	1.57	-	0.94	-	-
No. 5	61.78	1.13	-	-	-	-	-

Figure 3.40: SEM image of bare Pt foil (second sample) and point EDS analysis on the surface.

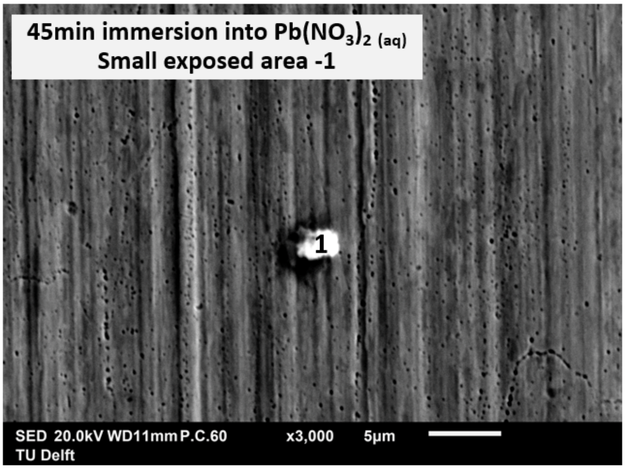

	Pt %	C %	O %	Si %	Pb %
No. 1	58.71	15.78	6.22	0.45	25.08

Figure 3.41: SEM/EDS result of Pt foil (small exposed area, first sample) after 45min immersion into $Pb(NO_3)_{2\ (aq)}$ and conducting 3 repetitive EIS measurements.

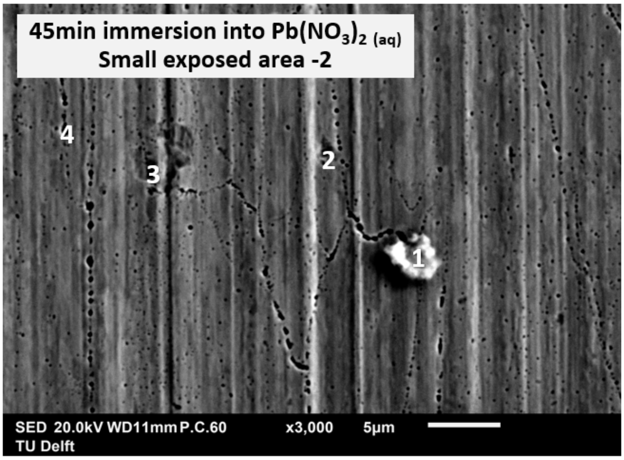

	Pt %	C %	O %	Si %	Fe %	Mg %	Al %	Pb %
No. 1	64.32	12.95	14.88	2.34	1.05	0.47	0.57	11.18
No. 2	73.65	2.18	5.49	-	2.58	-	-	-
No. 3	74.71	1.49	2.64	-	1.05	-	-	-
No. 4	75.75	1.35	-	-	-	-	-	-

Figure 3.42: SEM/EDS result of Pt foil (small exposed area, second sample) after 45min immersion into $Pb(NO_3)_2\ _{(aq)}$ and conducting 3 repetitive EIS measurements.

For the samples that were immersed into 50ppm $ZnSO_{4(aq)}$ during three repetitive EIS measurements, white particles also formed on the surface of Pt foil. However, no signal of zinc was detected on these white particles during EDS analysis. Only the signals of Pt, C, O, Si, and other elements that are related to the impurities of the Pt foil were detected. The situations are the same for both samples of the small and large exposed areas.

The signal of zinc was detected on the sample which has a 3-hour immersion time into 50ppm $ZnSO_{4(aq)}$ during 6 repetitive EIS measurements, as shown in figure 3.45. Although it is not clear which zinc-containing compound was formed on the electrode surface, the zinc-containing adsorbate likely came in the form of oxide since the signal of oxygen was also detected when the signal of zinc was present.

It should be noted that for the sample shown in figure 3.45 with zinc-containing adsorbates, the accelerating voltage of the electron beam was set at 10kV during SEM/EDS analysis, which is lower than that for the previous samples with lead-containing adsorbates (20kV). According to the energy table for EDS analysis provided by *Jeol*, the energy values of characteristic X-ray emitted from K_α line and L_α line of zinc are 8.630 keV and 1.012 keV, respectively. In addition, the energy values of characteristic X-ray emitted from L_α line and M line of lead are 10.550 keV and 2.342 keV, respectively. In principle, when the electron beam's acceler-

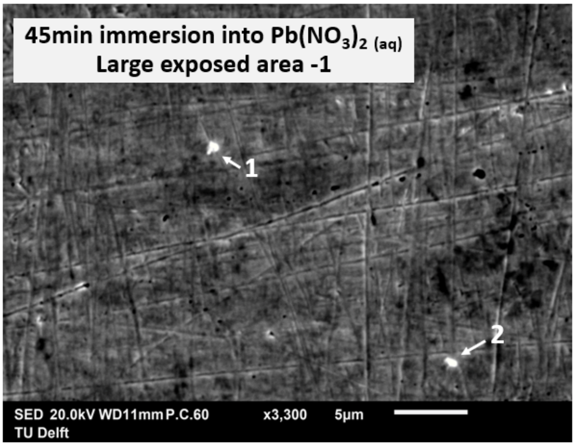

	Pt %	C %	O %	Si %	Mg %	Pb %
No. 1	79.82	3.97	4.90	0.56	-	10.75
No. 2	89.56	5.23	4.47	0.51	0.23	-

Figure 3.43: SEM/EDS result of Pt foil (large exposed area, first sample) after 45min immersion into $Pb(NO_3)_2$ $_{(aq)}$ and conducting 3 repetitive EIS measurements.

ating voltage is set at 20kV, the characteristic X-rays of both zinc and lead should be detectable. However, during practical operation, it was found that the optimal accelerating voltage for the detection of zinc should be set at 10-15kV. This is due to the fact that the peak intensity of Zn-L_α is much higher than that of Zn-K_α in the EDS spectrum [89]. In order to detect a trace amount of zinc, one should look at the signal of Zn-L_α, which has the energy of 1.012 keV, in the EDS spectrum. By decreasing the electron beam's accelerating voltage, the characteristic X-ray with lower energy can be better detected.

The signal of sodium was also detected in the sample shown in figure 3.45. It has been reported by Newbury that there is usually a problem for automatic peak identification when the energy of the two characteristic X-ray is very close to each other. The misidentification of Zn-L_α (1.012 keV) and Na-L_α (1.041 keV) is one of the examples. Since no source of sodium can be found during the whole experiment, Na's signal should be a misidentification due to Zn's presence.

In conclusion, the presence of lead-containing adsorbate is apparent. The signals of Pb-L_α and Pb-M were detected on all the tested samples that were shortly immersed into $Pb(NO_3)_2$ $_{(aq)}$ during EIS measurements. The adsorbate was formed as the white particles shown in SEM images. The signal of Zn-L_α was also detected on the sample that was immersed in $ZnSO_{4(aq)}$ for a longer time, with the setting of accelerating voltage being modified to 10kV. However, no signal of Zn was found on the samples that were shortly immersed into $ZnSO_{4(aq)}$ during EIS measurements.

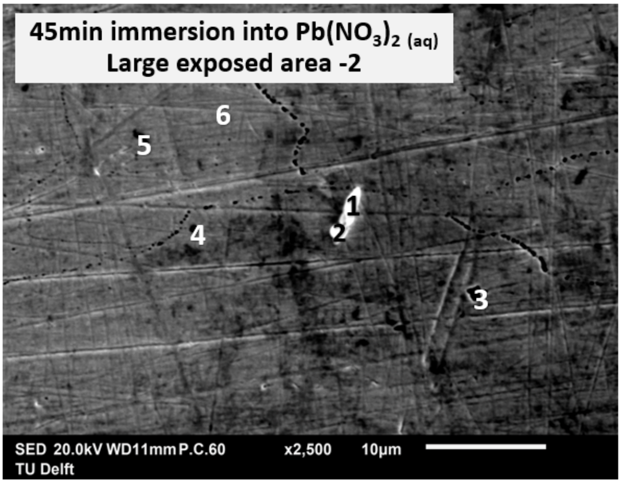

	Pt %	C %	O %	Si %	Ca %	Pb %
No. 1	78.65	4.20	2.91	-	-	14.24
No. 2	62.70	8.31	6.54	-	-	22.45
No. 3	90.47	1.59	6.22	1.72	-	-
No. 4	96.62	1.43	-	-	1.95	-
No. 5	98.29	1.71	-	-	-	-
No. 6	98.80	1.20	-	-	-	-

Figure 3.44: SEM/EDS result of Pt foil (large exposed area, second sample) after 45min immersion into $Pb(NO_3)_2$ $_{(aq)}$ and conducting 3 repetitive EIS measurements.

This is mainly because the original setting of accelerating voltage (20kV) was not optimal to detect the signal of zinc on those samples.

Finally, in addition to lead-containing and zinc-containing adsorbates, many white particles, without signal of Pb or Zn, formed on the Pt surface after immersion into HMI solutions. Some of the particles might be the adsorbates of Pb or Zn but were not successfully identified due to SEM/EDS setting. Some of the particles might be due to the contamination from the process of handling (e.g., gloves) or the environment (e.g., dust, air).

3.2.2. XPS analysis

In this section, the result of the XPS analysis is presented and discussed. This analysis aims to double-check the chemical composition of the adsorbates and get more information about the possible chemical form of them. It is worth notice that the analysis depth of XPS (4 to 5nm) is much lower than that of EDS ($1\mu m$). Therefore, the elemental signals obtained from XPS are more surface sensitive than that of EDS.

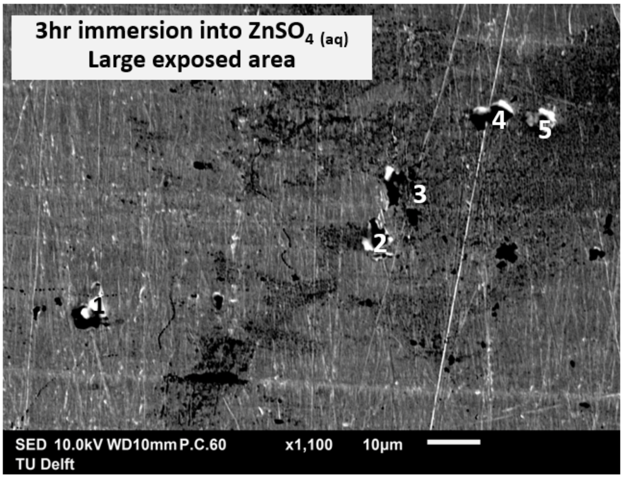

	Pt %	C %	O %	Si %	Ca %	Na %	Zn %
No. 1	38.23	48.48	6.36	-	1.81	0.53	4.60
No. 2	29.02	54.66	9.36	-	2.64	0.34	3.98
No. 3	98.56	1.44	-	-	-	-	-
No. 4	31.30	52.30	7.54	0.30	1.19	0.56	6.81
No. 5	69.73	25.47	2.79	-	-	-	2.02

Figure 3.45: SEM/EDS result of Pt foil (large exposed area) after 3hr continuous immersion in $ZnSO_{4\,(aq)}$ and conducting 6 repetitive EIS measurements.

The survey spectrum for the five tested samples is shown in appendix B. From table B.1, it can be seen that the atomic percentages of the Pb and Zn are below 1% for the samples that were shortly immersed into HMI solutions. After the scanning of high-resolution spectra, no evident peaks of Pb or Zn were observed in the short immersion samples. There are two possible reasons to explain the unsuccessful detection of Pb and Zn. First of all, the samples that were shortly immersed into HMI solutions were not hand-polished with fine-diamond particles, as illustrated in table 2.4. Since the surface was not flat enough, it gave more noise signals during XPS measurement, and the noise might cover the signals of target elements. The surface roughness of the originally supplied Pt foil and that of the hand-polished Pt foil was previously compared with figure 3.38. Second, the immersion time might not be long enough to generate the amount of absorption that can be successfully detected. Unlike point EDS analysis, which has a focused electron beam with a diameter ranging from 0.4 to 5 nm, the diameter of the scanning area in XPS analysis is 0.4 mm. If the concentration of the adsorbates was too low, after being divided by the whole analyzed area, the signal of adsorbates can become too small to be identified.

The high-resolution spectra for the sample that were continuously immersed in HMI solutions for 3 hours are shown in figure 3.47 and 3.46. Figure 3.47 shows the spectra for non-metallic elements, while figure 3.46 shows the spectra for metallic elements. As shown in figure 3.46 (c) and (d), the peaks of Pb 4f and Zn 2p3 become evident for the long immersion samples due to the smoothness of the surface after hand-polishing and enough duration for the adsorption process. The result provides evidence for the adsorption of HMI during EIS measurements.

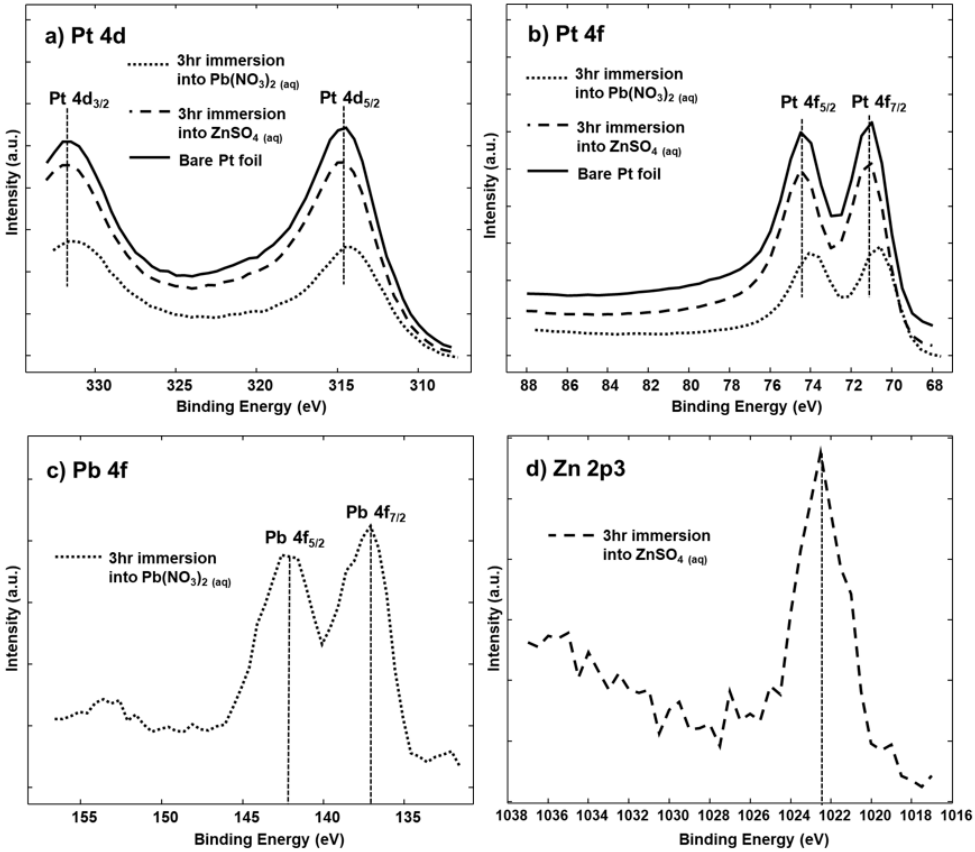

Figure 3.46: High resolution XPS spetra for the metallic elements.

In order to make sure that the presence of heavy metals on the Pt foil is due to the adsorption process rather than the direct precipitation of zinc sulfate or lead(II) nitrate, the high-resolution spectrum of nitrogen 1s and sulfur 2p were also scanned. It can be seen in figure 3.47 (c) that the intensity of the nitrogen peak is not very strong for the three samples, including bare Pt foil and two Pt foils that were immersed into HMI solutions. In addition, the nitrogen peak appears only on the bare Pt foil and the sample of long immersion into $ZnSO_{4(aq)}$, which means that

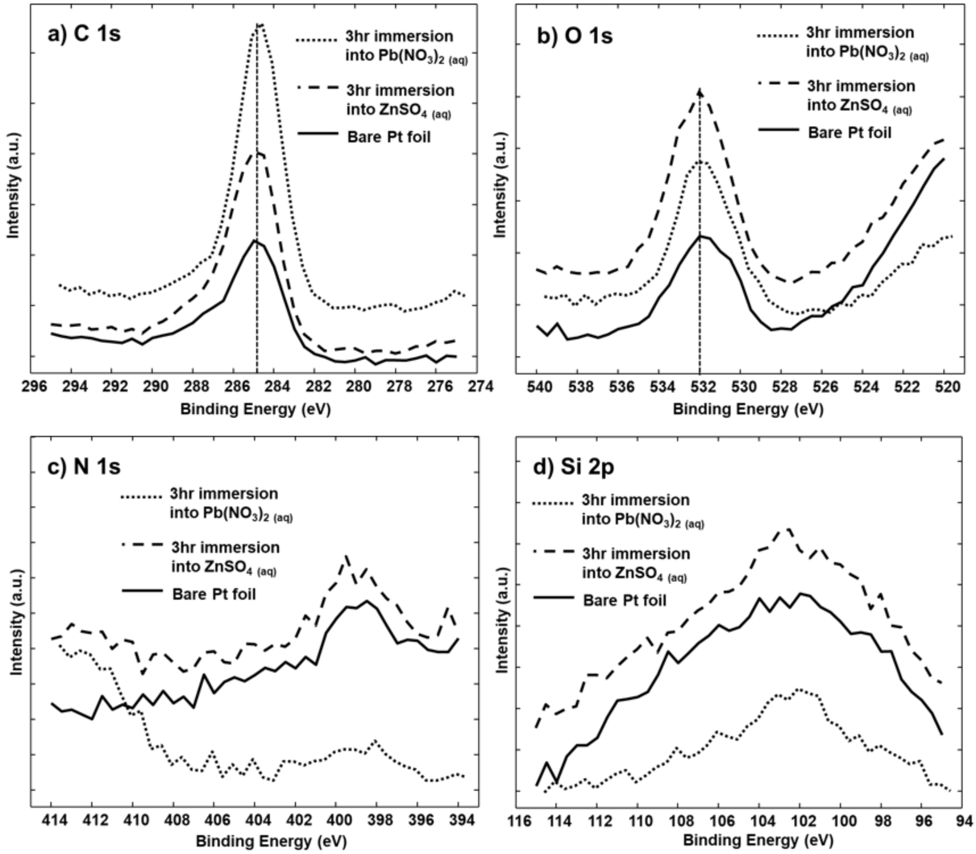

Figure 3.47: High resolution XPS spetra for the non-metallic elements.

the presence of nitrogen is probably due to contamination from air or the usage of nitrogen gas during the drying process of the samples. Another evidence to support the absence of nitrate precipitation is the binding energy of the nitrogen peak. The binding energy of N 1s for lead nitrate is generally around 407.2 eV in the XPS spectrum [91] [92], thus the increase of intensity on the right side of the figure for the sample of long immersion into $Pb(NO_3)_{2(aq)}$ is unlikely due to the peak of nitrate. As for sulfur, no evident peak was found in the high-resolution spectra for the three samples.

Since the data fitting was not conducted for the XPS analysis, it is impossible to determine the exact form of adsorption compounds on the Pt foil. However, by observing the shape of the spectra and the peak's binding energy, it is possible to obtain some clues about the possible chemical composition of the absorbates. For instance, in figure 3.46 (c) and (d), the peaks for Pb 4f and Zn 2p3 appear to be asymmetric. The result implies that the adsorbates are probably not in the form of pure metal but rather in the form of oxides, such as PbO_2 and ZnO. However, the spectrum of oxygen shown in figure 3.47 (b) does not fully agree with this argument, since the binding energy values of O 1s for PbO_2 and ZnO were reported to be around 529 eV [92] [93].

It is worth notice that there is a shift of platinum peaks for the sample that was immersed into $Pb(NO_3)_{2(aq)}$ for 3 hours, as shown in figure 3.46 (a) and (b). The peaks of Pt 4d and Pt 4f slightly shift to a position with lower binding energy compared to the other two samples, and the deviation is approximately 1 ev. Usually, the shift of peak in the XPS analysis is attributed to the charging effect on the material's surface. However, since the carbon peak was already corrected to 284.8 eV before analysis, the influence of the charging effect should be eliminated by the carbon correction already. In addition, the charging effect is generally not significant on the conductive metal without an insulating layer [94]. Another possibility for the peak shift is the chemical shift due to the change in the oxidation state of Pt or the local chemical and physical environment of Pt [95]. It is worth notice that the peak intensity of carbon 1s for the sample of long immersion into $Pb(NO_3)_{2(aq)}$ is the highest among all samples. In addition, the peak intensity of Pt 4d and 4f for the same sample appears to be the lowest. This result implies that the sample has the highest amount of adventitious carbon.

Since the signal of Si was detected in the EDS analysis, the high-resolution spectrum of Si 2p was examined again with XPS, as shown in figure 3.47 (d). However, the intensity of Si 2p peak was not significant compared to the background signals. Additionally, the binding energy of O 1s (532 eV) in figure 3.46 (b) is not fully compatible with that for the detection of SiO_2 (533 eV) [96]. In addition to the impurities present in the Pt foil, the contamination of silicon might also come from the silicone oil that was used during the construction of the electrochemical cell. The silicone oil was used as a lubricant for producing a hole in the acrylic holder and might be mixed into the holder during the cooling process. Nevertheless, the chance of having effusion of silicon from the acrylic holder to the HMI solution is very small, considering the holder was fully cleaned with an ultrasonic bath before surface analysis. Another possible source of silicon contamination is the silicon gloves, but the chances of having this kind of contamination are also small.

In conclusion, the XPS result indicates that there are HMI-related adsorbates present on the surface of the Pt electrode. However, since data fitting was not conducted, the exact chemical form of the adsorbates cannot be determined. In addition, since no significant peaks of nitrogen and sulfur were found on samples, it is assumed that NO_3^- and SO_4^{2-} do not participate in the adsorption/desorption process.

3.3. Modelling and data fitting

This section presents and discusses the results of modelling and data fitting into the equivalent circuit models. In the section of surface analysis, it was found that the HMI-related adsorbates were present on the electrode surface, supporting the hypothesis that the inductive behavior in the Nyquist impedance plot mainly results from the adsorption/desorption process of HMI. Based on this hypothesis, two equivalent circuit models (ECMs) were proposed separately for the case of DI water and the case of HMI solution by adapting the existing models from the literature. Finally, the EIS results are fitted into ECMs in order to compare the impedance response between the cases of 20ppm $ZnSO_{4(aq)}$ and 50ppm $Pb(NO_3)_{2(aq)}$, which exhibit similar impedance values as each other and cannot be distinguished with the previous methods of data analysis, as shown in section 3.1.1.

3.3.1. Proposal of equivalent circuit models (ECMs)

Figure 3.48 shows the proposed ECM for the case of DI water. This model is an adapted version of the classic Mixed Kinetic and Diffusion Control model, as illustrated in section 1.2.3. The model consists of: (1) two resistors, representing the ohmic resistance of the system ($R1$) and the charge transfer resistance ($R2$) between the electrode | electrolyte surface; (2) a constant phase element ($CPE1$), representing the double layer capacitance in a non-ideal system; (3) a finite-space Warburg element (W_O1), representing the diffusion process of ions.

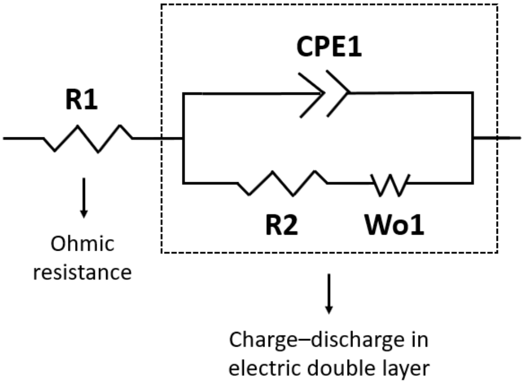

Figure 3.48: Equivalent circuit model for the case of DI water, adapted from ref [10].

In contrast to the case of DI water, the proposed ECM for HMI solutions is shown in figure 3.49. The model is adapted from the ECM developed by Cui *et al.*, which describes the adsorption of nickel ions on the material's surface in the electroless plating process. The model consists of four serial parts of circuit elements, corresponding to (1) ohmic resistance; (2) electric double layer; (3) adsorption of unstable intermediate on the electrode surface; (4) adsorption of HMI-related compounds on the electrode surface. It should be noted that the EIS results for the cases of $ZnSO_{4(aq)}$ and $Pb(NO_3)_{2(aq)}$ are both fitted into this model.

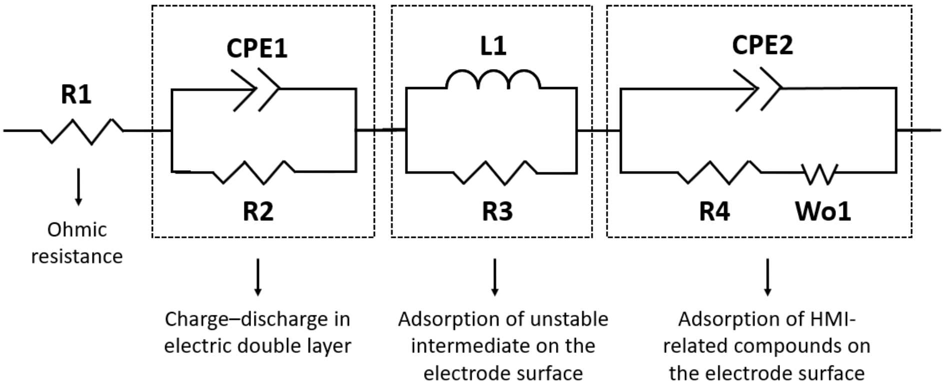

Figure 3.49: Equivalent circuit model for the case of HMI solutions, adapted from ref [16].

3.3.2. Data fitting and analysis

The results of EIS data fitting for the case of DI water and the case of HMI solutions are shown in figure 3.50, where the orange lines represent the simulated impedance response, and the grey lines represent the experimental data. In addition to the case of DI water, the three simulated cases of HMI solutions include 20ppm $ZnSO_{4(aq)}$, 50ppm $ZnSO_{4(aq)}$, and 50ppm $Pb(NO_3)_{2(aq)}$. As shown in the figure, the simulated impedance response is very close to the experimental result, though the individual simulated points are not fully aligned with the experimental data.

The values of each circuit element given by simulation are shown in table 3.2, where $R1$ and $R2$ represent the ohmic resistance and the charge transfer resistance (unit:Ω), respectively. As expected, the value of charge transfer resistance for the four solution cases descend as: DI water > 50ppm $Pb(NO_3)_{2(aq)}$ > 20ppm $ZnSO_{4(aq)}$ > 50ppm $ZnSO_{4(aq)}$. Although the impedance values of the characteristic points selected previously for 20ppm $ZnSO_{4(aq)}$ and 50ppm $Pb(NO_3)_{2(aq)}$ are difficult to distinguish, the modelling results of them are very different. One of the great differences is the value of CPE1-T, with the case of 20ppm $ZnSO_{4(aq)}$ being 4.6E-14 and the case of 50ppm $Pb(NO_3)_{2(aq)}$ being 1.02E-13. Considering the case of 50ppm $ZnSO_{4(aq)}$ together, one can see that the values of CPE-T and CPE-P for $ZnSO_{4(aq)}$ are generally higher than that for $Pb(NO_3)_{2(aq)}$. This is also true for the values of CPE2-T and CPE2-P. The differences between the constant phase elements are resulted from the size of the inductive loop of each HMI solution, which is correlated with the shape of the spiral as shown in the Nyquist impedance plot.

Unfortunately, it is not possible to correlate the value of CPE-T shown here to the physical meaning of the system. In principle, the parameter of CPE-P has a value between 0 and 1, indicating a pseudocapacitance. If CPE-P equals 0, then the constant phase element behaves like an ideal resistor, and CPE-T represents

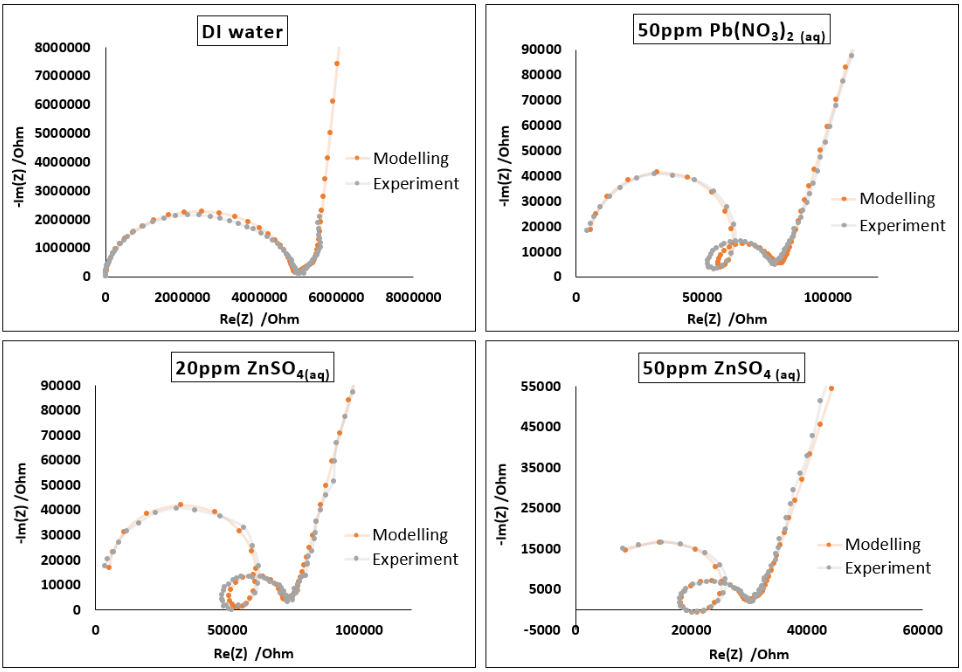

Figure 3.50: Simulation results for the case of DI water, 20ppm $ZnSO_{4(aq)}$, 50ppm $ZnSO_{4(aq)}$, and 50ppm $Pb(NO_3)_{2(aq)}$.

the value of resistance with the unit of Ω. In contrast, if CPE-P equals 1, then the constant phase element behaves like an ideal capacitor, and CPE-T represents the value of capacitance with the unit of F [97]. However, the CPE-P values obtained for HMI solutions after simulation are all higher than 1, which has no specific physical meaning. The only case which has the value of CPE-P below 1 is the case of DI water.

In addition to the above mentioned elements, the values of finite-space Warburg elements also show differences between 20ppm $ZnSO_{4(aq)}$ and 50ppm $Pb(NO_3)_{2(aq)}$. According to the instruction written in Zview software, $W_o - R$ represents the diffusion impedance, $W_o - P$ represents the exponential factor, and $W_o - T$ represents the diffusion interpretation, which is equal to L^2/D (L is the effective diffusion thickness, and D is the effective diffusion coefficient of the particle). However, the analysis of the Warburg element is beyond the scope of this project and will not be discussed further.

Overall, by data fitting into ECMs, more information about the differences between two HMI solutions can be obtained. Since the model not just considers a single point or value on the impedance plot but rather the whole impedance response, it provides a more holistic view of the changes in impedance as well as the inductive behavior. However, it is not an easy task to find a suitable ECM to properly describe the system and correlate each circuit element with the physical meaning of the system due to the semi-empirical nature of the ECM. Nevertheless, the data fitting results still provide a possibility to distinguish different types of HMIs in practical application. Future recommendations for the overall EIS sensor research and the development of modelling techniques are addressed in chapter 5.2.

Table 3.2: The values of equivalent circuit elements and their parameters given by the simulation.

		DI water	**50ppm $Pb(NO_3)_{2(aq)}$**	**20ppm $ZnSO_{4(aq)}$**	**50ppm $ZnSO_{4(aq)}$**
Ohmic resistance	**R1**	0	0	0	0
Double layer capacitance (non-ideal)	**CPE1-T***	1.59E-11	1.02E-13	4.6E-14	1.345E-14
	CPE1-P*	0.95742	1.286	1.345	1.44
Charge transfer resistance	**R2**	4860000	54000	48600	16600
Adsorption of unstable intermediate	**L1**	-	0.012	0.03	0.008
	R3	-	8000	9200	7000
Adsorption of HMI-related compounds	**CPE2-T***	-	3.098E-10	3.8E-11	3.506E-11
	CPE2-P*	-	1.08	1.26	1.22
	R4	-	22000	19500	11000
Diffusion of ions	**Wo1-R****	1779600	17655	20826	12844
	Wo1-T**	1.283	0.003	0.0048651	0.002557
	Wo1-P**	0.4758	0.405	0.42151	0.42827

* CPE-T: the amplitude factor of CPE; CPE-P: the depression factor of CPE, which determines whether CPE is more like a capacitor or a resistor.

** Wo-R: diffusion impedance; Wo-P: the exponential factor of the Warburg element; Wo-T: diffusion interpretation of the Warburg element.

4

Conclusion

In the first part of the research, each HMI solution was found to have its characteristic impedance values at a certain concentration in the mid- and high-frequency regions of the EIS spectrum. These regions are related to charge transfer resistance at the electrode surface and the system's non-diffusional resistance. As the concentration increases, the extent of the charge transfer resistance and the extent of the non-diffusional resistance decreases, following a linear relationship. The impedance values of the mixed HMI solution falls between the values for single HMI solutions. However, $Pb(NO_3)_{2(aq)}$ was found to have a dominant role in determining the impedance value of the mixed HMI solution at low concentration. In contrast, its dominant role vanished at high concentration. The phenomena were attributed to different tendency between the adsorption of Pb^{2+} and Zn $^{2+}$ to the electrode surface. Still, the quantification of the HMI-related adsorbates is needed to confirm the hypothesis.

The inductive behavior observed in the cases of HMI solutions was attributed to the adsorption/desorption process of HMI. After the appearance of HMI-related adsorbates on the electrode surface was confirmed by both SEM/EDS and XPS analysis, an equivalent circuit model related to ions' adsorption process was adapted from the literature. The result of data fitting and simulation helps to identify more differences between the impedance response of 20ppm $ZnSO_{4(aq)}$ and 50ppm $Pb(NO_3)_{2(aq)}$, which have similar extent of charge transfer resistance.

Overall, the EIS measurements for the detection of HMI show excellent reproducibility and high sensitivity. The influence of changing temperature on the EIS result was found to have a predictable pattern, and the error caused by 10°C deviation on the impedance change compared to DI water in log scale was less than 1%. It is possible to calibrate the influence of temperature during a later stage of sensor application. However, the system of mixed HMI solution is more complex than the system of a single HMI solution, and the interactions between the two HMIs need to be defined in the future study. In addition, the detection of HMI in the real water samples requires a better design of electrochemical cell with a higher impedance value than the current electrochemical cell, which can be achieved by decreasing the electrodes' surface area.

5

Recommendations

In this chapter, possible improvement of the research method and the validity of the experimental results are discussed integrally in section 5.1. In addition, the suggestions for extending this research by adjusting the current methodology are proposed. In contrast, the topics that were not explored in this research but are important for the future are listed in section 5.2, along with the proposal of EIS sensor prototype.

5.1. Improvement of the current research

In the first part of the current research, EIS results for different types of solutions were analyzed by selecting and comparing the characteristic points on the Bode impedance plot and Nyquist impedance plot. Although this method is a practical way to analyze a massive amount of data and quantify the influence of varying parameters, only some of the points can be correlated to the physical meaning of the system, such as the local maximum points on the Nyquist impedance plots, representing the extent of charge transfer resistance, and the local minimum points, representing the extent of overall non-diffusional resistance. In addition, the physical interpretation of the Bode impedance plot for the system of HMI detection has not been well-established. Since the connection between the Bode impedance plot and the Nyquist impedance plot was not built in this research, one cannot relate the information of frequency with the real or imaginary impedance values on the Nyquist impedance plot. Furthermore, the analysis point of impedance change compared to DI water was selected at log(freq)=2.5 on the Bode impedance plot, representing the system's overall impedance value. However, the stable plateau in the mid-frequency region shifts its horizontal position depending on varying parameters. The shift may induce some problems when two comparing samples' plateau region does not align with each other or does not appear at log(freq)=2.5. Thus, a better selection of analysis points is required in the future.

For the EIS measurements conducted with real water samples, the influence of the background medium is shown when mixing a portion of HMI solutions with the real water samples. A better way to add HMI into the real water samples is to dissolve the salt of $ZnSO_4{\cdot}H_2O_{(s)}$ or $Pb(NO_3)_{2(s)}$ directly into samples. However, after some trial experiments, the salts appeared to be insoluble in the industrial water samples and even form other types of insoluble compounds (yellowish precipitation) in the process. Since it is not clear which types of ions were present in the industrial water samples, it is impossible to define which chemicals were formed during precipitation. Further investigations are required to understand the original composition of the real water samples and develop a better way to conduct HMI detection experiments.

In the second part of the current research, the surface analysis was conducted on alternative Pt foils rather than the Pt wire used in the standard design due to the sample size requirement. Although the chemical composition of the two materials is the same (platinum with 99.99+% purity), and the electrochemical reactions between the Pt electrodes and the electrolyte should be more or less the same in the two systems, the impedance responses shown in the Nyquist impedance plot for the two systems are different. It is still questionable if the adsorption/desorption process of HMIs took place in the same way for the two systems and if the inductive behavior in one system can be explained by the surface analysis result in another system. The ideal way is to conduct surface analysis directly on the electrode of the standard design, but redesigning the electrochemical cell is needed for such a purpose. Another improvement to make in the future for the surface analysis is the setting of accelerating voltage in the SEM/EDS. Since every element has its optimal setting for detection, one should first figure out the optimal setting before experimenting. In addition, quantitative analysis is needed to understand if one HMI has a stronger tendency of adsorption than the other and quantify the increase of adsorbates with time. The quantification of adsorbates is crucial for the EIS senor since the senor may be immersed in the water environment for a long time during usage. Although the adsorption/desorption process did not influence the EIS results' reproducibility during the research, it is not clear if and how the accumulation of adsorbates on the electrode affects the EIS results when the immersion period is longer than 3 hours. Furthermore, further investigation is required to identify the exact chemical form of the adsorbates, such as data fitting in the XPS analysis.

In the last part of the current research, equivalent circuit models were proposed based on the hypothesis that attributes the inductive behavior present in the cases of HMI solutions to the adsorption/desorption process of HMIs. However, the values of CPE given by the simulation were not ideal and did not have significant physical meaning. In addition to checking other possible contribution to the inductive behavior, such as stray capacitance, wiring, and electric shielding of the system, one should also be aware of the semi-empirical nature of the equivalent circuit model and carefully construct or modify the model by selecting as few circuit elements as possible with a proper connection to the physical system. In the future, more EIS data should be fitted into ECMs to have a systematic analysis of the values of different circuit elements and to see the influence of changing parameters on them. In addition, the ECMs should be validated with extra in-situ measurements in the future.

5.2. Recommendation for future research and the proposal of the EIS sensor prototype

In addition to the research done in this project, there are several parameters that need to be further investigated for the development of the EIS sensor. The parameters that may have an impact on the EIS results are listed as follows:

- The pH value of the solution.
- The flow velocity of the liquid.
- Surface roughness of the electrode.
- Other geometric dimensions related to the design of electrochemical cell, which were not addressed in this research, such as the distance between the electrodes.

Additionally, investigations on the impedance response of other types of HMIs is required. It is worth notice that the two HMIs tested in this research, including Pb^{2+} and Zn^{2+}, have the same number of positive charges. Since the number of positive charges of these ions equals 2, these ions are likely to form intermediates during the process of adsorption and have a higher chance to meet the requirement for the inductive behavior mentioned in chapter 3.1.1. Therefore, testing ions with a different number of positive charges, such as Ni^{+} and Fe^{3+} is crucial for understanding the inductive behavior and the adsorption/desorption process of HMI. In addition, the influence of the anions on the EIS measurements, such as NO_3^{-} and SO_4^{2-} present in this research, has not been fully studied yet. Although NO_3^{-} and SO_4^{2-} were believed not to participate in the adsorption/desorption process since no related adsorbates were found in the surface analysis, these anions may also affect other aspects of the EIS measurements.

Finally, the author would like to suggest that the extension of this research is conducted with the EIS sensor prototype developed together with the supervisors and collaborators of this project. The design of the EIS sensor prototype is shown in figure 5.1 and the dimension of it is shown in figure 5.2. As discussed in chapter 3.1.4 and 3.1.5, every design of electrochemical cell creates it own specific impedance spectrum, and the surface area of the electrode should be decreased for the HMI detection in a real water environment. Therefore, the EIS data for various HMIs should be collected with a device that is close to the real application of the EIS sensor and has a dimension calculated in the scale of μm. In addition, since distinguishing the types of HMIs involves a more complicated process for EIS, the sensor surface can be designed to have selective properties and only reacts with the target elements. Another possibility is to combine the DC measurements with EIS, such as cyclic voltammetry (CV), to double-check the result produced by EIS, as shown in figure 5.1.

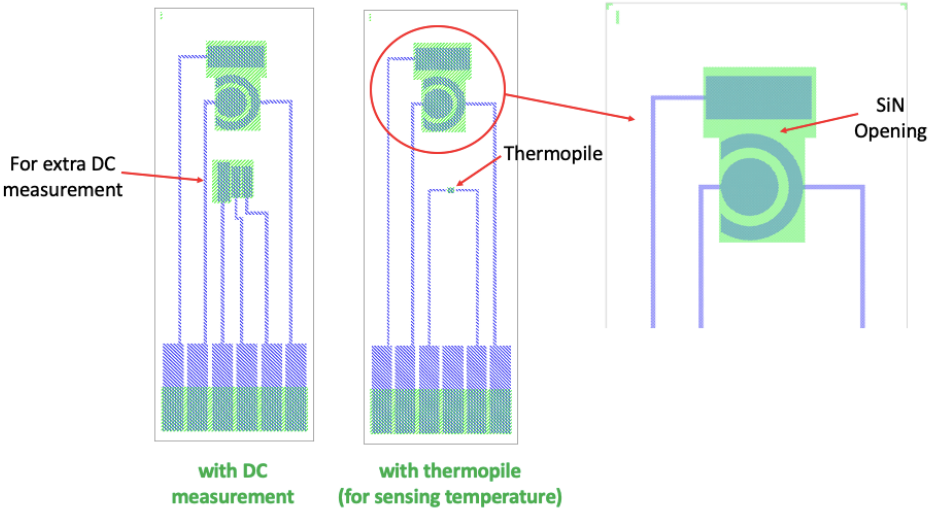

Figure 5.1: Prototypes of the EIS sensors designed in the form of a chip.

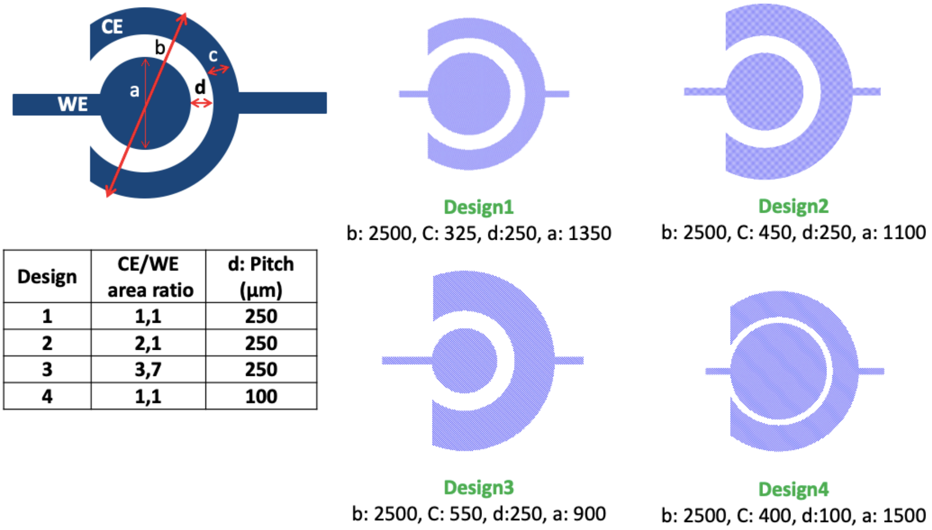

Design	CE/WE area ratio	d: Pitch (µm)
1	1,1	250
2	2,1	250
3	3,7	250
4	1,1	100

Figure 5.2: The dimension of the main electrodes on the EIS sensor prototypes.

Since the EIS sensor prototype is planned to use platinum for the reference

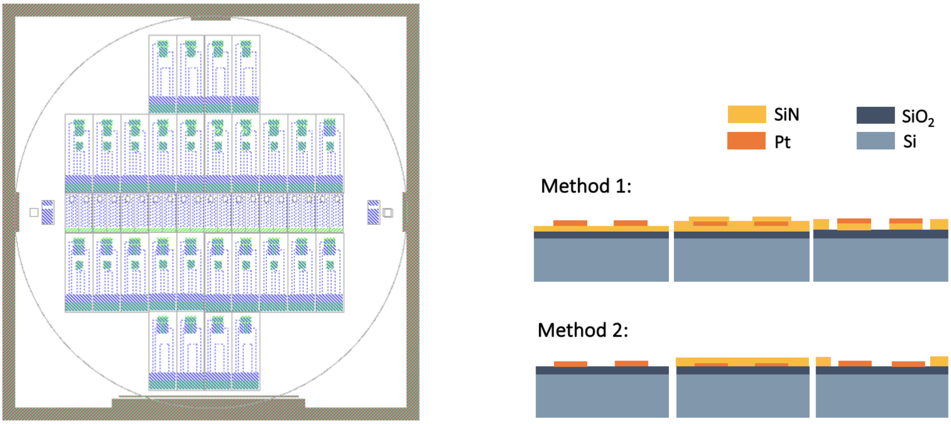

(a) The arrangement of EIS sensor on a wafer.

(b) The production flow of the sensor surface.

Figure 5.3: The illustration of the manufacturing process of the EIS sensor prototype.

electrode, considering the mass production of products shown in figure 5.3, it is crucial to understand the effect of stray capacitance between the RE and the WE during EIS measurements. Although the electrochemical cell with Pt wire as the RE also produces reproducible data as the standard design, as discussed in chapter 3.1.4, the inductive behavior was intensified by the geometric construction of the cell. Therefore, more trial testings for the 3-Pt-electrode system are needed in the future to minimize the artifacts that may generate undesirable results in the EIS measurements. As for the data analysis, it is suggested to use a more advanced algorithm such as principal component analysis (PCA) in the future to process the data extracted from Bode impedance plots. In addition, the analysis on Bode phase shift plot and the impedance response in the very-low-frequency region are now excluded from the scope of the project. It is suggested to include these parts in future research to extract extra information.

A

XRD Result

In this appendix, the XRD result for the platinum wire that was used as WE or CE in the electrochemical cells mentioned in chapter 2.1 was presented. The main purpose of the XRD analysis is to check the chemical composition of the platinum wire and its possible impurities in order to compare with that of the ordered Pt foil. The XRD pattern for the bare platinum wire (cross section) is shown in figure A.1. The XRD pattern is fully compatible with the platinum spectrum, and no other crystalline phases were detected, indicating a pure platinum composition.

In addition to bare platinum wire, the Pt wires that were immersed into 50ppm $Pb(NO_3)_{2(aq)}$ and 50ppm $ZnSO_{4\ (aq)}$ during 3 repetitive EIS measurements were also checked with XRD. However, the XRD pattern for these samples did not show any other elemental signals except platinum. The XRD pattern of the sample that was immersed into 50ppm $Pb(NO_3)_{2(aq)}$ is shown in figure A.2, while the XRD pattern of the sample that was immersed into 50ppm $ZnSO_{4\ (aq)}$ is shown in figure A.3. The result indicates that the concentration of HMI-adsorbates on the Pt surface was too low to be detected by XRD.

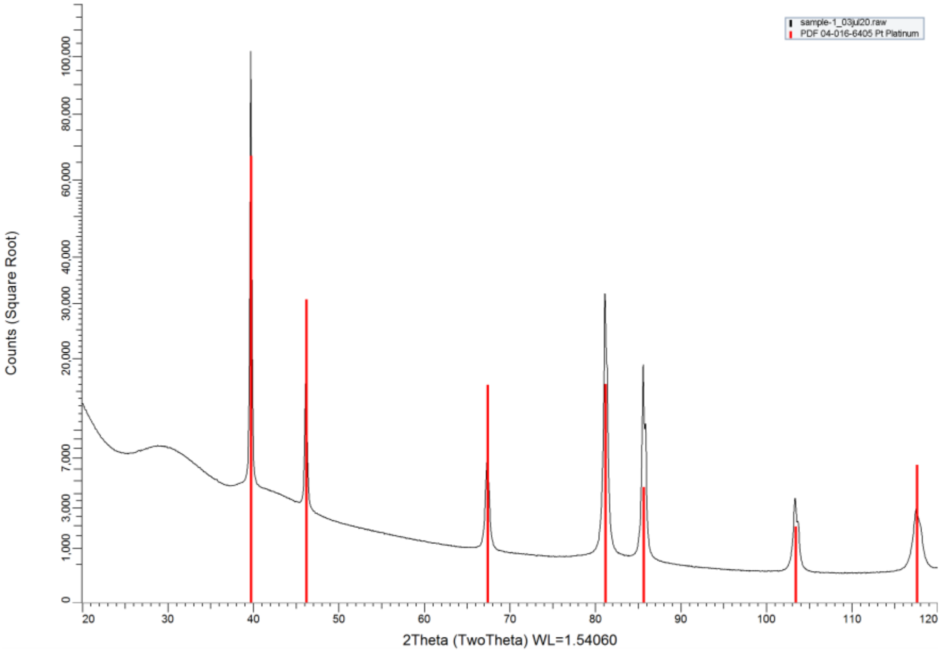

Figure A.1: XRD pattern for the cross section surface of bare platinum wire.

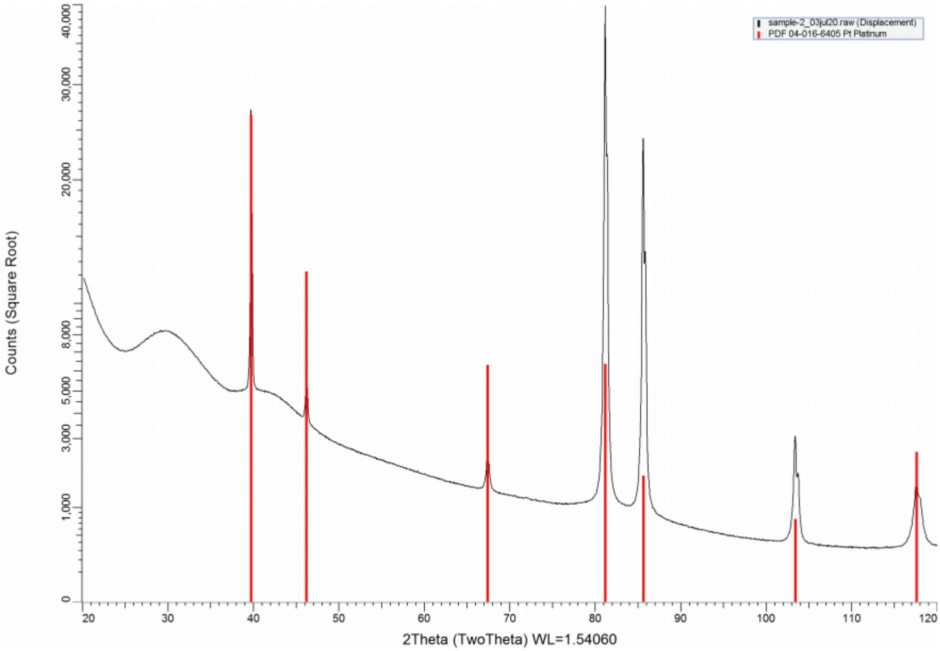

Figure A.2: XRD pattern for the cross section surface of the platinum wire that was immersed in 50ppm $Pb(NO_3)_{2(aq)}$ during 3 repetitive EIS measurements.

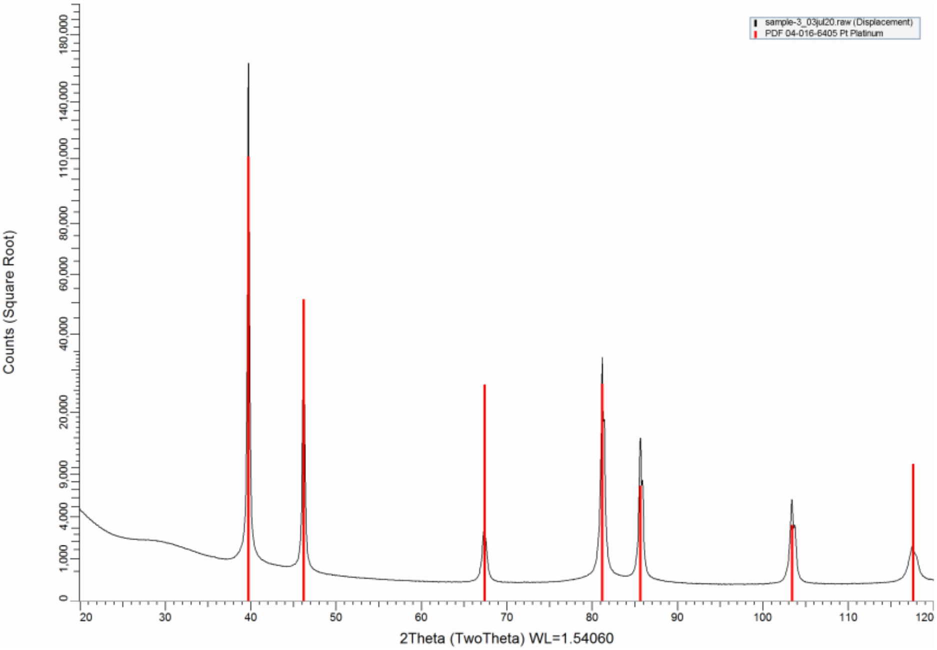

Figure A.3: XRD pattern for the cross section surface of the platinum wire that was immersed in 50ppm $ZnSO_4$ $_{(aq)}$ during 3 repetitive EIS measurements.

B

XPS Result

In this appendix, the survey spectrum of XPS analysis is presented. Table B.1 shows the atomic percentage of each element on the five samples that were investigated during the XPS analysis. In addition, figure B.1 shows the XPS survey spectrum of the five samples.

Table B.1: Atomic percentage (unit:%) acquired from the XPS survey spectrum for bare Pt foil and Pt foils that were immersed into HMI solutions during EIS experiments.

	Pt 4f	**C 1s**	**O 1s**	**Si 2p**	**N 1s**	**Pb 4f**	**S 2p**	**Zn 2p3**
Bare Pt foil	34.2	35.9	16.9	5.2	7.7	-	-	-
45min immersion into $Pb(NO_3)_{2\ (aq)}$	3.3	73.2	16.4	4.8	-	0.4	-	-
45min immersion into $ZnSO_4$ (aq)	2.3	72.8	18.9	4.6	-	-	0.8	0.5
3hr immersion into $Pb(NO_3)_{2\ (aq)}$	12.9	52.2	14.8	13.2	5.4	1.4	-	-
3hr immersion into $ZnSO_{4\ (aq)}$	20.3	37.0	20.6	12.9	5.3	-	2.4	1.4

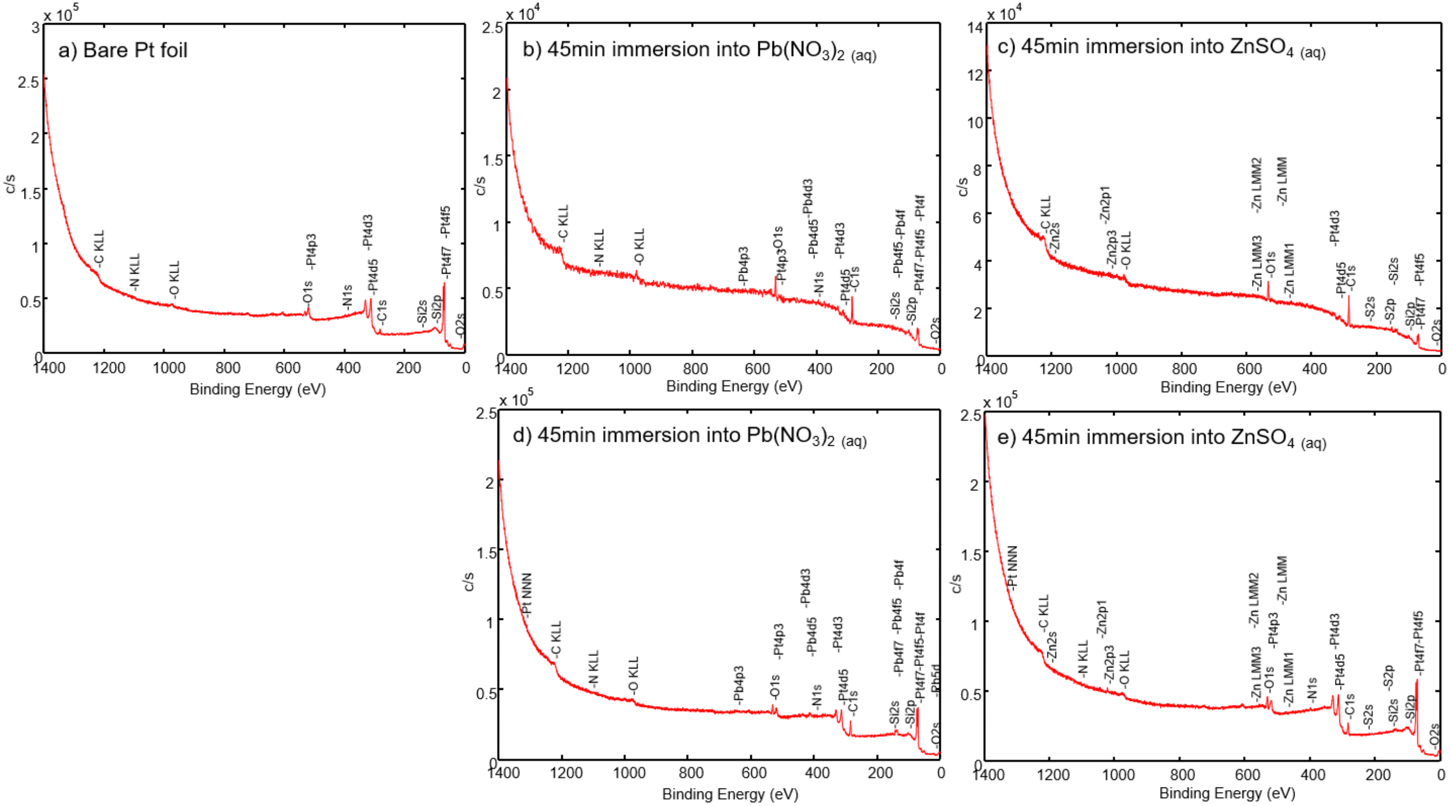

Figure B.1: XPS survey spectrum for the bare Pt foil and Pt foils that were immersed in HMI solutions during EIS measurements.

C

Bode Phase Shift Plots

In this appendix, the Bode phase shift plot for all the EIS measurements are shown. The sequence of these plots is arranged according to the topics discussed in chapter 3. Since the discussion and data analysis on the Bode phase shift plot are beyond the scope of this project, the original data are plotted without further description.

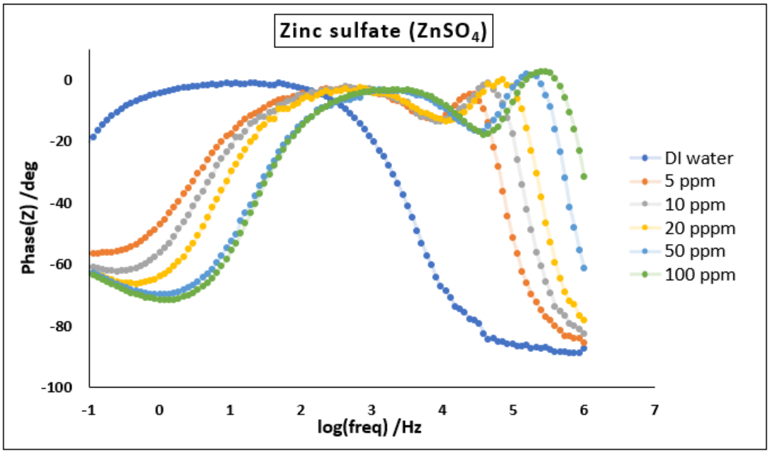

Figure C.1: Bode phase shift plot for $ZnSO_{4\ (aq)}$ at various concentration at 20°C.

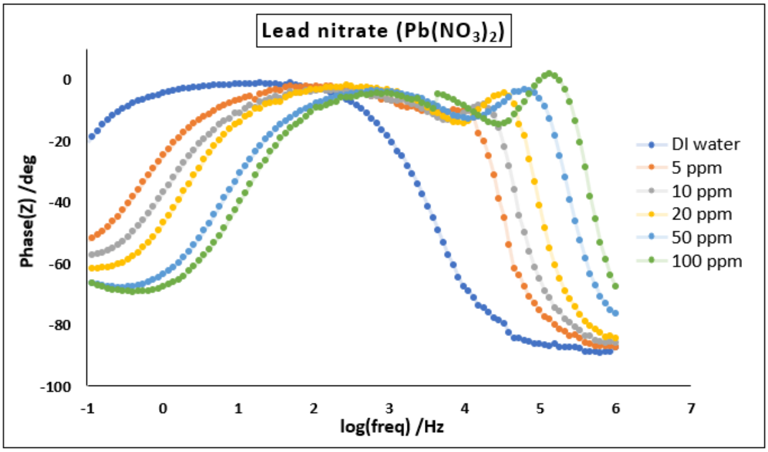

Figure C.2: Bode phase shift plot for $Pb(NO_3)_{2\ (aq)}$ at various concentration at 20°C.

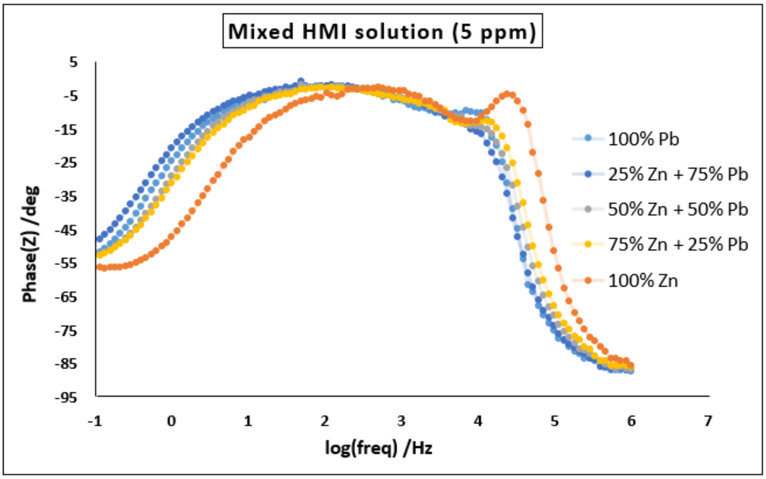

Figure C.3: Bode phase shift plot for 5ppm mixed HMI solution with various mixing ratio at 20°C.

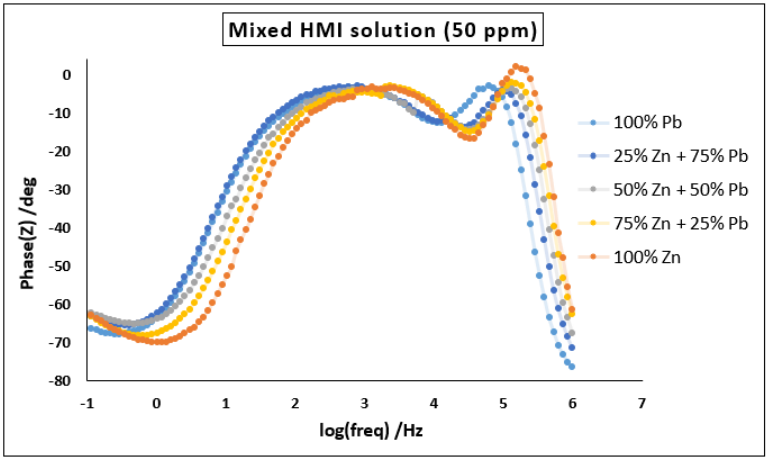

Figure C.4: Bode phase shift plot for 50ppm mixed HMI solution with various mixing ratio at 20°C.

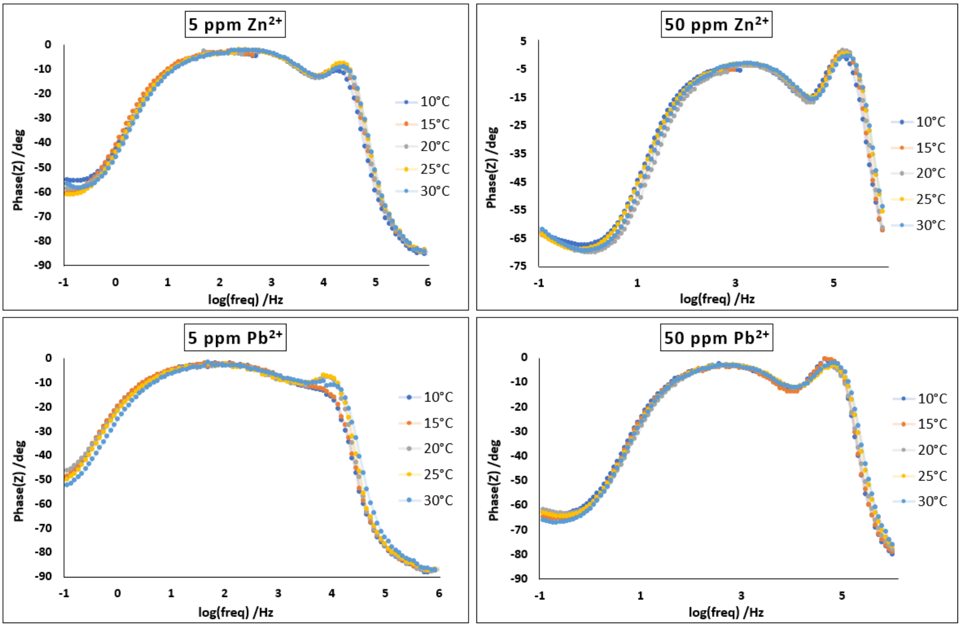

Figure C.5: Bode phase shift plot for 4 cases of HMI solutions at various temperature.

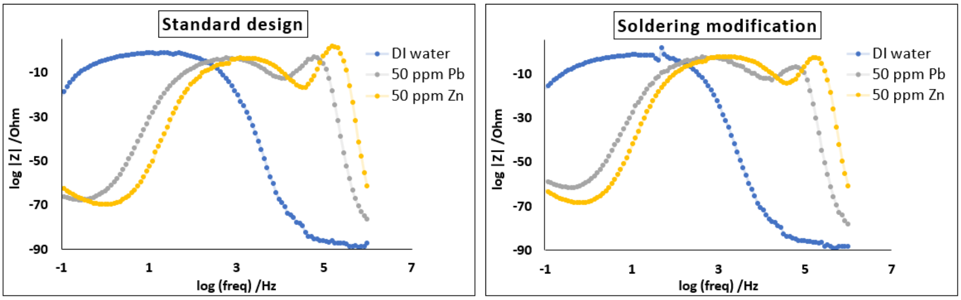

Figure C.6: Comparison of Bode phase shift plot between the standard electrochemical cell design and the soldering modification.

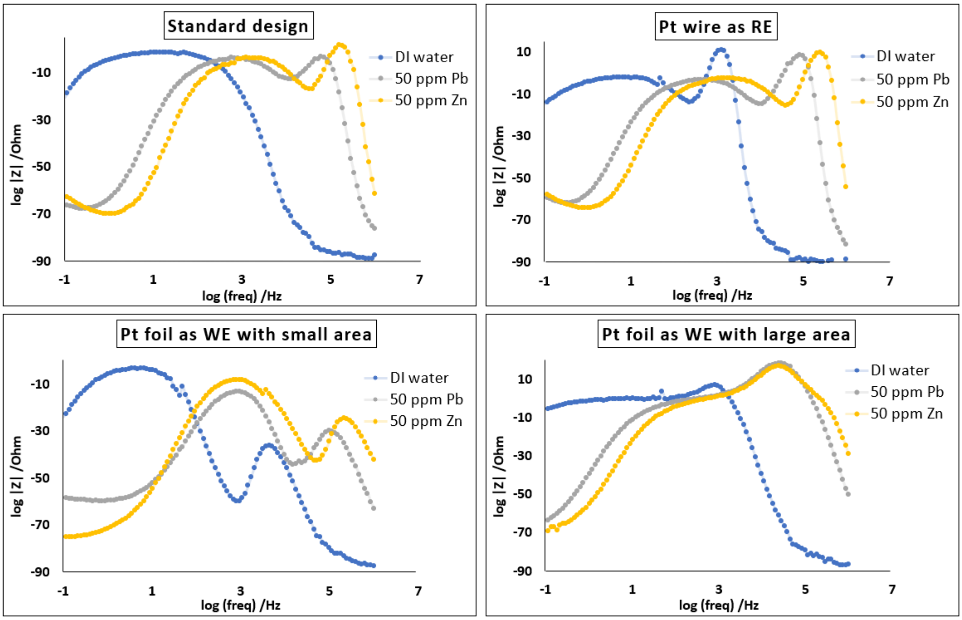

Figure C.7: Comparison of Bode impedance plot between the standard electrochemical cell design and the designs for surface analysis / evaluation of sensor prototype.

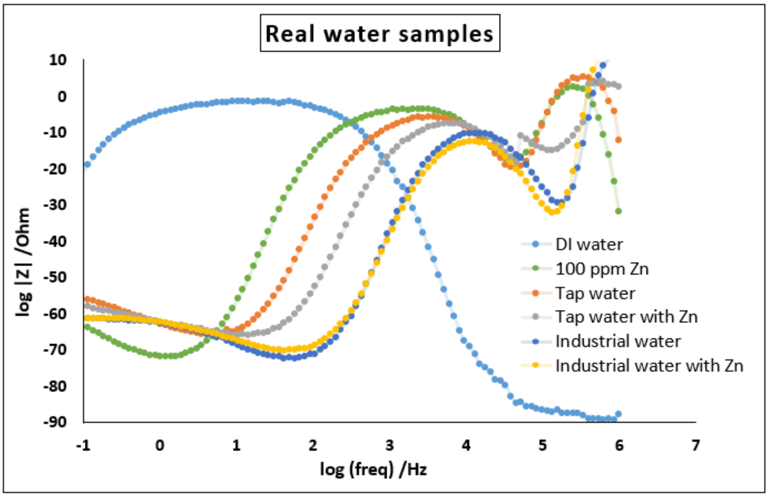

Figure C.8: Bode phase shift plot of real water samples.

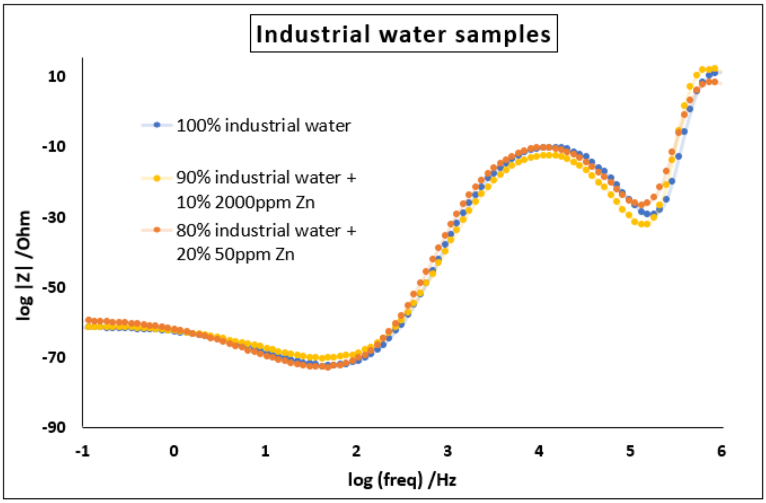

Figure C.9: Bode phase shift plot of industrial water samples.

Bibliography

[1] F. Edition, *Guidelines for drinking-water quality,* WHO chronicle **38**, 104 (2011).

[2] G. March, T. D. Nguyen, and B. Piro, *Modified electrodes used for electrochemical detection of metal ions in environmental analysis,* Biosensors **5**, 241 (2015).

[3] B. Bansod, T. Kumar, R. Thakur, S. Rana, and I. Singh, *A review on various electrochemical techniques for heavy metal ions detection with different sensing platforms,* Biosensors and Bioelectronics **94**, 443 (2017).

[4] J. A. Rodríguez, E. Barrado, M. Vega, Y. Castrillejo, and J. L. Lima, *Sequential injection anodic stripping voltammetry at tubular gold electrodes for inorganic arsenic speciation,* Electrochemical Cells-New Advances in Fundamental Researches and Applications. Publisher InTech, Croatia (available on-line) , 203 (2012).

[5] J. Barton, M. B. G. García, D. H. Santos, P. Fanjul-Bolado, A. Ribotti, M. McCaul, D. Diamond, and P. Magni, *Screen-printed electrodes for environmental monitoring of heavy metal ions: a review,* Microchimica Acta **183**, 503 (2016).

[6] M. Pandiarajan and S. Rajendran, *Applications of cyclic voltammetry,* International Journal of Nano Corrosion Science and Engineering **3**, 166 (2016).

[7] Ossila Ltd, *Cyclic voltammetry: Basic principles & set up,* `https://www.ossila.com/pages/cyclic-voltammetry`, [Online; accessed 19-November-2020].

[8] S. Zhang, H. Zhu, P. Ma, F. Duan, W. Dong, and M. Du, *A self-supported electrochemical sensor for simultaneous sensitive detection of trace heavy metal ions based on ptau alloy/carbon nanofibers,* Analytical Methods **9**, 6801 (2017).

[9] Z. Zou, A. Jang, E. Macknight, P.-M. Wu, J. Do, P. L. Bishop, and C. H. Ahn, *Environmentally friendly disposable sensors with microfabricated on-chip planar bismuth electrode for in situ heavy metal ions measurement,* Sensors and Actuators B: Chemical **134**, 18 (2008).

[10] X.-Z. R. Yuan, C. Song, H. Wang, and J. Zhang, *Electrochemical impedance spectroscopy in PEM fuel cells: fundamentals and applications* (Springer Science & Business Media, 2009).

[11] B.-A. Mei, O. Munteshari, J. Lau, B. Dunn, and L. Pilon, *Physical interpretations of nyquist plots for edlc electrodes and devices,* The Journal of Physical Chemistry C **122**, 194 (2018).

[12] S. G. R. Avuthu, B. B. Narakathu, A. Eshkeiti, S. Emamian, B. J. Bazuin, M. Joyce, and M. Z. Atashbar, *Detection of heavy metals using fully printed three electrode electrochemical sensor,* in *SENSORS, 2014 IEEE* (IEEE, 2014) pp. 669–672.

[13] R. Karkra, P. Kumar, B. K. Bansod, S. Bagchi, P. Sharma, and C. R. Krishna, *Classification of heavy metal ions present in multi-frequency multi-electrode potable water data using evolutionary algorithm,* Applied Water Science **7**, 3679 (2017).

[14] S. Liu, M. Kang, F. Yan, D. Peng, Y. Yang, L. He, M. Wang, S. Fang, and Z. Zhang, *Electrochemical dna biosensor based on microspheres of cuprous oxide and nano-chitosan for hg (ii) detection,* Electrochimica Acta **160**, 64 (2015).

[15] T. Q. Nguyen and C. Breitkopf, *Determination of diffusion coefficients using impedance spectroscopy data,* Journal of The Electrochemical Society **165**, E826 (2018).

[16] G. Cui, S. Liu, K. Wang, Q. Li, and G. Wu, *Discovering p-doped mechanism in non-magnetic ni–p films for hdd substrate: a combined experimental and theoretical study,* RSC Advances **4**, 14663 (2014).

[17] N. Srivastava and C. Majumder, *Novel biofiltration methods for the treatment of heavy metals from industrial wastewater,* Journal of hazardous materials **151**, 1 (2008).

[18] J. O. Duruibe, M. Ogwuegbu, J. Egwurugwu, *et al.*, *Heavy metal pollution and human biotoxic effects,* International Journal of physical sciences **2**, 112 (2007).

[19] K.-J. Appenroth, *Definition of "heavy metals" and their role in biological systems,* in *Soil heavy metals* (Springer, 2010) pp. 19–29.

[20] S. Singh, S. Lal, J. Harjit, S. Amlathe, and H. Kataria, *Potential of metal extractants in determination of,* Advanced Studies in Biology **3**, 239 (2011).

[21] M. B. Gumpu, S. Sethuraman, U. M. Krishnan, and J. B. B. Rayappan, *A review on detection of heavy metal ions in water–an electrochemical approach,* Sensors and actuators B: chemical **213**, 515 (2015).

[22] Y. H. Han, S. Z. Kim, S. H. Kim, and W. H. Park, *Suppression of arsenic trioxide-induced apoptosis in hela cells by n-acetylcysteine.* Molecules & Cells (Springer Science & Business Media BV) **26** (2008).

[23] S.-Y. Ho, W.-J. Wu, H.-W. Chiu, Y.-A. Chen, Y.-S. Ho, H.-R. Guo, and Y.-J. Wang, *Arsenic trioxide and radiation enhance apoptotic effects in hl-60 cells through increased ros generation and regulation of jnk and p38 mapk signaling pathways,* Chemico-biological interactions **193**, 162 (2011).

[24] M. Kessel, S. X. Liu, A. Xu, R. Santella, and T. K. Heil, *Arsenic induces oxidative dna damage in mammalian cells,* in *Oxygen/Nitrogen radicals: Cell injury and disease* (Springer, 2002) pp. 301–308.

[25] M. Valko, H. Morris, and M. Cronin, *Metals, toxicity and oxidative stress,* Current medicinal chemistry **12**, 1161 (2005).

[26] S. J. Flora, *Structural, chemical and biological aspects of antioxidants for strategies against metal and metalloid exposure,* Oxidative medicine and cellular longevity **2** (2009).

[27] M. Hutton and C. Symon, *The quantities of cadmium, lead, mercury and arsenic entering the uk environment from human activities,* Science of the total environment **57**, 129 (1986).

[28] F. Habashi, *Chemistry and metallurgy in the american indian empires,* Canadian Mining and Metallurgical Bulletin(Canada) **85**, 103 (1992).

[29] D. L. Baun and T. H. Christensen, *Speciation of heavy metals in landfill leachate: a review,* Waste management & research **22**, 3 (2004).

[30] M. Ghaedi, K. Niknam, A. Shokrollahi, E. Niknam, H. R. Rajabi, and M. Soylak, *Flame atomic absorption spectrometric determination of trace amounts of heavy metal ions after solid phase extraction using modified sodium dodecyl sulfate coated on alumina,* Journal of Hazardous Materials **155**, 121 (2008).

[31] M. Ghaedi, M. Reza Fathi, A. Shokrollahi, and F. Shajarat, *Highly selective and sensitive preconcentration of mercury ion and determination by cold vapor atomic absorption spectroscopy,* Analytical Letters **39**, 1171 (2006).

[32] L. Rottmann and K. G. Heumann, *Determination of heavy metal interactions with dissolved organic materials in natural aquatic systems by coupling a high-performance liquid chromatography system with an inductively coupled plasma mass spectrometer,* Analytical Chemistry **66**, 3709 (1994).

[33] M. Faraji, Y. Yamini, A. Saleh, M. Rezaee, M. Ghambarian, and R. Hassani, *A nanoparticle-based solid-phase extraction procedure followed by flow injection inductively coupled plasma-optical emission spectrometry to determine some heavy metal ions in water samples,* Analytica chimica acta **659**, 172 (2010).

[34] R. Sitko, P. Janik, B. Zawisza, E. Talik, E. Margui, and I. Queralt, *Green approach for ultratrace determination of divalent metal ions and arsenic species using total-reflection x-ray fluorescence spectrometry and mercapto-modified graphene oxide nanosheets as a novel adsorbent,* Analytical chemistry **87**, 3535 (2015).

[35] A. Yusof, M. Rahman, and A. Wood, *Speciation of some trace elements in water samples after preconcentration on activated carbon by neutron activation analysis,* Journal of radioanalytical and nuclear chemistry **259**, 479 (2004).

[36] Q. Zhou, N. Zhao, and G. Xie, *Determination of lead in environmental waters with dispersive liquid–liquid microextraction prior to atomic fluorescence spectrometry,* Journal of hazardous materials **189**, 48 (2011).

[37] L. Pujol, D. Evrard, K. Groenen-Serrano, M. Freyssinier, A. Ruffien-Cizsak, and P. Gros, *Electrochemical sensors and devices for heavy metals assay in water: the french groups' contribution,* Frontiers in chemistry **2**, 19 (2014).

[38] J. Feldmann, P. Salaün, and E. Lombi, *Critical review perspective: elemental speciation analysis methods in environmental chemistry–moving towards methodological integration,* Environmental Chemistry **6**, 275 (2009).

[39] A. Krolicka, A. Bobrowski, K. Kalcher, J. Mocak, I. Svancara, and K. Vytras, *Study on catalytic adsorptive stripping voltammetry of trace cobalt at bismuth film electrodes,* Electroanalysis: An International Journal Devoted to Fundamental and Practical Aspects of Electroanalysis **15**, 1859 (2003).

[40] G. Gillain, G. Duyckaerts, and A. Disteche, *Direct and simultaneous determinations of zn, cd, pb, cu, sb and bi dissolved in sea water by differential pulse anodic stripping voltammetry with a hanging mercury drop electrode,* Analytica Chimica Acta **106**, 23 (1979).

[41] R. J. Reay, A. F. Flannery, C. W. Storment, S. P. Kounaves, and G. T. Kovacs, *Microfabricated electrochemical analysis system for heavy metal detection,* Sensors and Actuators B: Chemical **34**, 450 (1996).

[42] C. R. T. Tarley, V. S. Santos, B. E. L. Baêta, A. C. Pereira, and L. T. Kubota, *Simultaneous determination of zinc, cadmium and lead in environmental water samples by potentiometric stripping analysis (psa) using multiwalled carbon nanotube electrode,* Journal of hazardous materials **169**, 256 (2009).

[43] F. G. Thomas and G. Henze, *Introduction to voltammetric analysis: theory and practice* (Csiro Publishing, 2001).

[44] EDAQ, *Anodic stripping voltammetry: Hints and tips,* `https://www.edaq.com/w/index.php?title=Anodic_Stripping_Voltammetry:_Hints_and_Tips&oldid=4301` (2017), [Online; accessed 17-November-2020].

[45] E. Schonberger and W. Pickering, *The influence of ph and complex formation on the asv peaks of pb, cu and cd,* Talanta **27**, 11 (1980).

[46] K. Salariya, A. Umar, S. K. Kansal, and S. K. Mehta, *Rapidly synthesized polyethylene glycol coated cadmium sulphide (cds) nanoparticles as potential scaffold for highly sensitive and selective lethal cyanide ion sensor,* Sensors and Actuators B: Chemical **241**, 276 (2017).

[47] M. Krasovska, V. Gerbreders, I. Mihailova, A. Ogurcovs, E. Sledevskis, A. Gerbreders, and P. Sarajevs, *Zno-nanostructure-based electrochemical sensor: Effect of nanostructure morphology on the sensing of heavy metal ions,* Beilstein journal of nanotechnology **9**, 2421 (2018).

[48] K. Deshmukh, S. Sankaran, B. Ahamed, K. K. Sadasivuni, K. S. Pasha, D. Ponnamma, P. R. Sreekanth, and K. Chidambaram, *Dielectric spectroscopy,* in *Spectroscopic Methods for Nanomaterials Characterization* (Elsevier, 2017) pp. 237–299.

[49] R. Maalouf, C. Fournier-Wirth, J. Coste, H. Chebib, Y. Saïkali, O. Vittori, A. Errachid, J.-P. Cloarec, C. Martelet, and N. Jaffrezic-Renault, *Label-free detection of bacteria by electrochemical impedance spectroscopy: comparison to surface plasmon resonance,* Analytical chemistry **79**, 4879 (2007).

[50] I. O. K'Owino and O. A. Sadik, *Impedance spectroscopy: a powerful tool for rapid biomolecular screening and cell culture monitoring,* Electroanalysis: An International Journal Devoted to Fundamental and Practical Aspects of Electroanalysis **17**, 2101 (2005).

[51] P. L. Bonora, F. Deflorian, and L. Fedrizzi, *Electrochemical impedance spectroscopy as a tool for investigating underpaint corrosion,* Electrochimica acta **41**, 1073 (1996).

[52] S. Carrara, V. Bavastrello, D. Ricci, E. Stura, and C. Nicolini, *Improved nanocomposite materials for biosensor applications investigated by electrochemical impedance spectroscopy,* Sensors and Actuators B: Chemical **109**, 221 (2005).

[53] A. Ward, *Dielectric materials for advanced applications,* State of the art research (2016).

[54] J. Hirschenhofer, D. Stauffer, R. Engelman, and M. Klett, *Fuel cell handbook. us department of energy federal energy technology center,* (1998).

[55] R. Kötz and M. Carlen, *Principles and applications of electrochemical capacitors,* Electrochimica acta **45**, 2483 (2000).

[56] C. Lei, F. Markoulidis, Z. Ashitaka, and C. Lekakou, *Reduction of porous carbon/al contact resistance for an electric double-layer capacitor (edlc),* Electrochimica acta **92**, 183 (2013).

[57] I. Yang, S.-G. Kim, S. H. Kwon, M.-S. Kim, and J. C. Jung, *Relationships between pore size and charge transfer resistance of carbon aerogels for organic electric double-layer capacitor electrodes,* Electrochimica Acta **223**, 21 (2017).

[58] B. B. Narakathu, M. Z. Atashbar, F. A. Abebe, C. S. Eribal, and E. Sinn, *8.2. 5 detection of zn2+ ions using a novel chemosensor based on coumarin schiff-base derivatives by electrochemical and fluorescence spectroscopy,* Proceedings IMCS 2012 , 690 (2012).

[59] M. V. Nambo, J. A. G. Gnecchi, E. R. Archundia, A. d. C. T. Anguiano, L. I. P. Lázaro, J. G. R. Ruiz, and D. L. Espinoza, *An experimental study of electrical impedance spectroscopy analysis of conductive liquids,* in *2018 IEEE International Autumn Meeting on Power, Electronics and Computing (ROPEC)* (IEEE, 2018) pp. 1–6.

[60] S. B. Hočevar, B. Ogorevc, J. Wang, and B. Pihlar, *A study on operational parameters for advanced use of bismuth film electrode in anodic stripping voltammetry,* Electroanalysis: An International Journal Devoted to Fundamental and Practical Aspects of Electroanalysis **14**, 1707 (2002).

[61] S. Zhang, K. Xu, and T. Jow, *Electrochemical impedance study on the low temperature of li-ion batteries,* Electrochimica acta **49**, 1057 (2004).

[62] A. A. N. EC08, *Basic overview of the working principle of a potentiostat/galvanostat (pgstat)–electrochemical cell setup,* Metrohm Autolab. BV , 1 (2011).

[63] K. M. Hambidge and N. F. Krebs, *Zinc deficiency: a special challenge,* The Journal of nutrition **137**, 1101 (2007).

[64] N. Roney, *Toxicological profile for zinc* (Agency for Toxic Substances and Disease Registry, 2005).

[65] A. Ara, J. A. Usmani, *et al.*, *Lead toxicity: a review,* Interdisciplinary toxicology **8**, 55 (2015).

[66] R. Rubin, D. S. Strayer, E. Rubin, *et al.*, *Rubin's pathology: clinicopathologic foundations of medicine* (Lippincott Williams & Wilkins, 2008).

[67] A. D. Woolf, R. Goldman, and D. C. Bellinger, *Update on the clinical management of childhood lead poisoning,* Pediatric Clinics of North America **54**, 271 (2007).

[68] R. F. Egerton *et al.*, *Physical principles of electron microscopy*, Vol. 56 (Springer, 2005).

[69] G. Parker, *Encyclopedia of materials: science and technology,* (2001).

[70] Nanoscience Instruments, *Scanning electron microscopy,* `https://www.nanoscience.com/techniques/scanning-electron-microscopy/` (2017), [Online; accessed 19-November-2020].

[71] T. L. Barr, *Modern ESCAThe Principles and Practice of X-Ray Photoelectron Spectroscopy* (CRC press, 1994).

[72] Z. Stoynov and D. Vladikova, *Differential impedance analysis, marin drinov acad,* Publish. House, Sofia, Bulgaria (2005).

[73] K. Neyerlin, W. Gu, J. Jorne, and H. A. Gasteiger, *Study of the exchange current density for the hydrogen oxidation and evolution reactions,* Journal of The Electrochemical Society **154**, B631 (2007).

[74] J. Fleig, J. Jamnik, J. Maier, and J. Ludvig, *Inductive loops in impedance spectroscopy caused by electrical shielding,* Journal of the Electrochemical Society **143**, 3636 (1996).

[75] H. Brandstätter, I. Hanzu, and M. Wilkening, *Myth and reality about the origin of inductive loops in impedance spectra of lithium-ion electrodes—a critical experimental approach,* Electrochimica acta **207**, 218 (2016).

[76] M. Balabajew and B. Roling, *Minimizing artifacts in three-electrode double layer capacitance measurements caused by stray capacitances,* Electrochimica Acta **176**, 907 (2015).

[77] M. Itagaki, A. Taya, K. Watanabe, and K. Noda, *Deviations of capacitive and inductive loops in the electrochemical impedance of a dissolving iron electrode,* Analytical Sciences **18**, 641 (2002).

[78] D. Harrington and P. Van den Driessche, *Stability and electrochemical impedance of mechanisms with a single adsorbed species,* Journal of Electroanalytical Chemistry **501**, 222 (2001).

[79] S. Cruz-Manzo, R. Chen, and P. Greenwood, *Analysis of the performance of an open-cathode polymer electrolyte fuel cell stack using simultaneous electrochemical impedance spectroscopy measurements,* ECS Transactions **48**, 47 (2014).

[80] L. Khotseng, *Oxygen reduction reaction,* Electrocatalysts for Fuel Cells and Hydrogen Evolution-Theory to Design (2018).

[81] A. Ekop and N. Eddy, *Adsorption of pb2+, zn2+ and ni2+ from aqueous solution by helix aspera shell,* E-Journal of Chemistry **6** (2009).

[82] J. Taparcevska, L. Markovska, B. Koumanova, and V. Meshko, *Diffusion models for adsorption kinetics of zn2+, cd2+ and pb2+ onto natural zeolite,* Water Science and Technology **62**, 1136 (2010).

[83] C.-H. Wu, C.-Y. Kuo, and S.-S. Guan, *Adsorption kinetics of lead and zinc ions by coffee residues.* Polish Journal of Environmental Studies **24** (2015).

[84] M. V. Maslova, V. I. Ivanenko, N. Y. Yanicheva, and N. V. Mudruk, *Comparison of the sorption kinetics of lead (ii) and zinc (ii) on titanium phosphate ion-exchanger,* International Journal of Molecular Sciences **21**, 447 (2020).

[85] F. Martin-Dupont, V. Gloaguen, R. Granet, M. Guilloton, H. Morvan, and P. Krausz, *Heavy metal adsorption by crude coniferous barks: a modelling study,* Journal of Environmental Science and Health, Part A **37**, 1063 (2002).

[86] T. Momma, M. Matsunaga, D. Mukoyama, and T. Osaka, *Ac impedance analysis of lithium ion battery under temperature control,* Journal of Power Sources **216**, 304 (2012).

[87] G. A. Williamson, V. W. Hu, T. B. Yoo, M. Affandy, C. Opie, E. K. Paradis, and V. C. Holmberg, *Temperature-dependent electrochemical characteristics of antimony nanocrystal alloying electrodes for na-ion batteries,* ACS Applied Energy Materials **2**, 6741 (2019).

[88] H. Vedage, T. A. Ramanarayanan, J. Mumford, and S. Smith, *Electrochemical growth of iron sulfide films in h2s-saturated chloride media,* Corrosion **49**, 114 (1993).

[89] Y. Liao, *Practical electron microscopy and database,* (2006).

[90] D. E. Newbury, *Mistakes encountered during automatic peak identification of minor and trace constituents in electron-excited energy dispersive x-ray microanalysis,* Scanning: The Journal of Scanning Microscopies **31**, 91 (2009).

[91] M. Biesinger, *X-ray photoelectron spectroscopy (xps) reference pages,* Surface Science Western, University of Western Ontario, Ontario (2015).

[92] J. A. Taylor, G. M. Lancaster, and J. W. Rabalais, *Chemical reactions of n 2+ ion beams with group iv elements and their oxides,* Journal of Electron Spectroscopy and Related Phenomena **13**, 435 (1978).

[93] M. C. Biesinger, L. W. Lau, A. R. Gerson, and R. S. C. Smart, *Resolving surface chemical states in xps analysis of first row transition metals, oxides and hydroxides: Sc, ti, v, cu and zn,* Applied surface science **257**, 887 (2010).

[94] D. R. Baer, K. Artyushkova, H. Cohen, C. D. Easton, M. Engelhard, T. R. Gengenbach, G. Greczynski, P. Mack, D. J. Morgan, and A. Roberts, *Xps guide: Charge neutralization and binding energy referencing for insulating samples,* Journal of Vacuum Science & Technology A: Vacuum, Surfaces, and Films **38**, 031204 (2020).

[95] F. C. Krebs, *Polymer photovoltaics: a practical approach,* (SPIE-International Society for Optical Engineering, 2008).

[96] G. Beamson, *High resolution xps of organic polymers,* The Scienta ESCA 300 Database (1992).

[97] Y. Gönüllü, K. Kelm, S. Mathur, and B. Saruhan, *Equivalent circuit models for determination of the relation between the sensing behavior and properties of undoped/cr doped tio2 nts,* Chemosensors **2**, 69 (2014).